



UNIVERSITY OF SIENA

DEPARTMENT OF
PHYSICAL SCIENCES, EARTH AND ENVIRONMENT

PHD PROGRAM IN EXPERIMENTAL PHYSICS

XXXVIII CYCLE

COORDINATOR: PROF. ALESSANDRO CERRI

Ag-111 radiopharmaceutical development in the context
of the ISOLPHARM project: from radionuclides
production to preclinical studies

Disciplinary Scientific Sector: PHYS-06/A

Supervisor:
Prof. Emilio Mariotti

Candidate:
Davide Serafini
ID 133204

Co-supervisor:
Dr. Alberto Andrighetto

Academic year 2024-2025

Ai miei genitori

Abstract

^{111}Ag is a radionuclide with promising features for nuclear medicine, particularly as a precursor for theranostic radiopharmaceuticals intended for Targeted Radionuclide Therapy. Preclinical studies, which are essential to assess the suitability of a radiopharmaceutical for its intended clinical application, are being conducted within the framework of the ISOLPHARM project. This project involves a wide collaboration of institutes and researchers, coordinated by the National Laboratories of Legnaro of the National Institute for Nuclear Physics (INFN-LNL). At this site, the SPES facility will host the production of ^{111}Ag via the ISOL technique. Thanks to a resonant ionisation laser ion source and a mass separation stage, the produced radionuclides can be collected with high specific activity. The work described in this thesis contributed to the development and installation of the experimental setup for the collection of the radionuclide. In parallel with the production activities, preclinical studies on ^{111}Ag were also carried out. To support these studies, two custom imaging devices were designed and built: one is sensitive to β radiation and the other one to γ radiation. These instruments were specifically tailored to the decay characteristics of ^{111}Ag , to fully exploit its imaging potential. Their development was further supported by the creation of corresponding digital twins using the GEANT4 simulation toolkit.

Riassunto

^{111}Ag è un radionuclide con caratteristiche interessanti nel campo della fisica medica, in particolare come precursore di un radiofarmaco per la radioterapia metabolica. Nel contesto del progetto ISOLPHARM, sono in corso studi preclinici con questo radionuclide, allo scopo di validare un possibile radiofarmaco che possa essere utilizzato in ambito clinico. Il progetto si basa su una ampia collaborazione di istituti e ricercatori ed è coordinato dai Laboratori Nazionali di Legnaro dell'Istituto Nazionale di Fisica Nucleare (INFN-LNL). In questi laboratori si trova la struttura SPES, che ospiterà la produzione di ^{111}Ag tramite tecnica ISOL. Grazie a una sorgente di ioni basata su laser risonanti e a un selettore di massa, i radionuclidi prodotti potranno essere raccolti con una alta attività specifica. Il lavoro descritto in questa tesi ha contribuito allo sviluppo e all'installazione del setup sperimentale per la raccolta dei radionuclidi. In parallelo alle attività sulla produzione dei radionuclidi, sono stati condotti studi preclinici riguardanti ^{111}Ag . Al fine di supportare questa tipologia di studi, due dispositivi di imaging sono stati disegnati e costruiti: il primo è un beta detector sensibile alla radiazione carica mentre il secondo è una gamma-camera, per i raggi gamma. Questi strumenti sono stati progettati seguendo le caratteristiche tipiche del decadimento di ^{111}Ag , con lo scopo di sfruttarne appieno il potenziale come tracciante. Lo sviluppo di questi dispositivi è stato supportato dalla creazione di due corrispondenti gemelli digitali, realizzati usando il software GEANT4 per simulazioni Monte Carlo.

Contents

1	Introduction	1
1.1	Targeted Radionuclide Therapy	1
1.2	Novel Medical Radionuclides	3
1.3	Radionuclide production	5
1.4	The ISOLPHARM project	8
1.5	Geant4 Monte Carlo simulations	12
1.6	Thesis results	13
2	The ISOLPHARM experimental station	15
2.1	ISOL radionuclide production at SPES	17
2.2	Resonant Ionisation Laser Ion Source	23
2.3	Production estimation	29
2.4	Collection on the SPES Tape Station	32
2.5	IRIS development and installation	34
2.6	Conclusion	42
3	DUMBO for ^{111}Ag	43
3.1	Motivation	43
3.2	Device technical description	47
3.3	DUMBO digital twin	52
3.4	Experimental results	54
3.5	Discussion	57
3.6	Conclusion	59
4	Gamma camera for ^{111}Ag	60
4.1	Motivation	60
4.2	Device technical description	61
4.3	Prediction with Monte Carlo simulations	62
4.4	Measurements with ^{111}Ag	69
4.5	Conclusion	74

5	Preclinical studies with ^{111}Ag	75
5.1	Characterisation of a multimodal imaging device	76
5.2	Imaging of ^{111}Ag phantoms	82
5.3	Biodistribution of ^{111}Ag	85
5.4	Conclusion	90
	Conclusion	91
	Bibliography	94
A	Radioactivity for nuclear medicine	114
A.1	Radionuclide	114
A.2	Effective disappearance half-life	115
A.3	Decay chain	115
A.4	Radionuclide sample properties	116
	References	117
B	Detector calibration at MEDICIS	119
B.1	Introduction	119
B.2	Materials and Methods	120
B.3	Results	128
B.4	Conclusion	137
	References	137
	List of publications	139
	List of Acronyms	141

List of Figures

1.1	World map with breast cancer statistics.	2
1.2	Schematic representation of a small-molecule radiopharmaceutical. From [7].	2
1.3	The steps necessary for drug discovery and development. The probability of success at each step is indicated. From [23]. . .	4
1.4	Production curve for a generic radionuclide according to Eq. (1.1). . .	6
1.5	Decay Scheme of ^{111}Ag . From [36].	9
1.6	Comparison of the electrons energy spectrum of ^{111}Ag with the ones of β -emitting radionuclides used for cancer therapy. . . .	11
1.7	Logos of the ISOLPHARM experiments.	11
1.8	Comparison between BetaShape and Geant4 ^{111}Ag beta-rays energy spectra.	13
2.1	Nuclear research reactor of the LENA laboratory at Pavia. From [44]	16
2.2	Steps for ISOL radionuclide production at SPES.	17
2.3	Layout of the SPES facility. From [55].	19
2.4	3D model section of the Target Ion Source unit.	20
2.5	Radionuclides of possible medical interest that can be produced at SPES. Adapted from [7].	21
2.6	Cross section values for ^{111}Ag production via ^{238}U fission, from the EXFOR database.	22
2.7	SPES Tape Station scheme. Adapted from [67].	22
2.8	Scheme of the RILIS technique.	24
2.9	Combination of mass and element selections in an ISOL facility.	24
2.10	Selected excitation path for silver with corresponding energy levels. From [73].	25
2.11	Graph representing the 28 pm scan for the first transition, while keeping the second transition fixed at 421.402 nm. From [73]. . .	26
2.12	Picture of the SPES online laser laboratory.	28
2.13	Picture of the TOF-MS present in the SPES online laser laboratory.	28

2.14	In-target production rates for fission of UC_x induced by a 40 MeV proton beam.	29
2.15	β decay chain with ^{111}Ag as daughter nucleus. From [36]. . . .	31
2.16	Measurement scheme for a tape station cycle.	33
2.17	Picture showing the implantation station part of IRIS while decoupled from the beamline.	35
2.18	The ISOLPHARM Radionuclide Implantation Station (IRIS) at SPES.	37
2.19	Efficiency curve of the IRIS germanium detector; the fit is performed using the logarithmic polynomial described in Eq. (2.25). . . .	38
2.20	Screenshot of the main control tab of the IRIS Graphical User Interface (GUI).	40
2.21	Loading phase components and monitoring system.	40
2.22	Screenshot of the CCTVs feeds.	41
2.23	Front view of the IRIS motion system.	41
3.1	Scheme highlighting the differences between radiography and autoradiography.	43
3.2	Radioluminescence microscope scheme. From [92].	44
3.3	Brightfield and radioluminescence images of FDG uptake in single cells acquired with the RLM setup.	45
3.4	Lensless radiomicroscope scheme. From [25].	45
3.5	Brightfield and beta imaging of ^{18}F -FDG in breast cancer cells via LRM.	46
3.6	Scheme of the DUMBO acquisition mechanism.	47
3.7	Schematic cross section of an ALPIDE pixel.	48
3.8	Scheme of the electronics implemented in DUMBO.	49
3.9	Scheme representing the workflow of the acquisition system. . . .	50
3.10	3D model of DUMBO.	52
3.11	Structure of an ALPIDE pixel unit as simulated in Geant4. . . .	53
3.12	Image of vials containing ^{111}Ag solution. The hit maps have a 8×8 binning.	55
3.13	Plastic phantom acquisition with ^{111}Ag solution.	56
3.14	GelMA phantom acquisition with ^{111}Ag solution.	58
4.1	Scheme representing the basic components of an Anger scintillation camera and the imaging workflow. Adapted from [115]. . . .	60
4.2	S14160-3050HS-08 quantum efficiency spectrum. From [121]. . . .	62
4.3	Graphical representation of the simulated gamma camera. . . .	63
4.4	Simulation of a collimated beam of 342 keV gamma-rays impinging directly on the scintillator.	65

4.5	Triggered channels per event with a 342 keV gamma-rays source.	65
4.6	Simulated response of a distribution of ^{111}Ag 342 keV gamma-rays generated in a line along the x-axis.	66
4.7	Representation of the 4-D MOBY phantom with models for heart and respiratory motions. From [127].	67
4.8	Simulated images with two tumours 5 mm apart inside a mouse model.	68
4.9	Acquisition of the large vial containing ^{111}Ag , without the collimator.	70
4.10	Images of the small vial filled with the ^{111}Ag solution with activity 7.36 MBq.	71
4.11	Total charge for the large vial acquisition with energy windows on the 245 keV (red band) and 342 keV (green band) peaks. .	72
4.12	Profiles of a ^{111}Ag acquisition analysed with different energy windows.	73
4.13	Acquisition of the phantom bladder filled with ^{111}Ag superimposed with the phantom geometry.	73
5.1	Phantom design scheme.	79
5.2	Scheme of the geometry used in the data collection with the Bruker In Vivo Xtreme.	80
5.3	Scheme of the geometry used in the simulations. From [146]. .	81
5.4	CLI images with ^{111}Ag (a) and ^{68}Ga (b).	82
5.5	Counts-activity correlation plots for ^{111}Ag and ^{68}Ga in the CLI experimental image.	84
5.6	DRI images for ^{111}Ag and ^{68}Ga	85
5.7	Autoradiography images of the mouse injected with 1.5 MBq of ^{111}Ag . Images are acquired at 1 h, 3 h, 24 h, 48 h, 120 h, 144 h post-injection.	88
5.8	Mice biodistribution calculated as injected activity per gram per organ.	89
A.1	Schematic representation of the patient dose as a function of time for radionuclides with different half-lives. Adapted from [4].	116
B.1	Offline setup for detector characterisation.	121
B.2	Plot of the efficiency logarithm values \mathcal{L} fitted with logarithm polynomials of different grades.	124
B.3	Diagram illustrating the steps to estimate the activity of a radioactive source with a Kromek CZT detector.	126

B.4	^{152}Eu energy spectrum with Gaussian fitting curves superimposed to the main full-energy peaks.	128
B.5	Energy calibration plot with residuals.	129
B.6	FWHM estimated for the peaks of ^{152}Eu , ^{133}Ba , ^{60}Co	130
B.7	Comparison between the efficiency values obtained analysing the ^{152}Eu spectrum with different software programs.	131
B.8	Efficiency values obtained with different sealed sources for the GR05 detector; with fitting curve and corresponding residuals.	132
B.9	Estimation of the activity of the calibration sources using the efficiency curve fitting the experimental data.	133
B.10	Efficiency curve configuration in Kromek MultiSpect.	133

List of Tables

1.1	Decay features of some radionuclides of interest.	10
2.1	Radiative neutron capture reactions for natural Palladium isotopes. Adapted from [45].	15
2.2	In-target production yields for ^{111}Ag radioactive isobars. Data from [81].	32
2.3	Fit parameters for the germanium efficiency	39
3.1	Features comparison between the developed β -imaging device DUMBO and the Lensless RadioMicroscope (LRM).	49
3.2	List of parameters and corresponding values chosen for the experiments.	50
3.3	Description of the FESTO items used to move the sample. . .	51
5.1	Phases required for the development of a radiopharmaceutical. From [9].	75
5.2	Decay features of ^{111}Ag and ^{68}Ga	77
5.3	Activity of ^{68}Ga and ^{111}Ag at the start of the experiment according to the hole volume.	80
5.4	Linear coefficients of the fits in the form $y = mx + q$ for ^{68}Ga and ^{111}Ag CLI images.	83
B.1	Radioactive sources used for the detector calibration and test.	120
B.2	Gamma lines of interest for the measured sources. Data are retrieved from the NNDC [5].	121
B.3	Optimised parameters for the efficiency fit with the functions described in Equation (B.1) and (B.2).	128
B.4	Optimised parameters for the efficiency fit with the function described in Equation (B.11).	132
B.5	Covariance matrix for the efficiency fit with the function described in Equation (B.11).	132

B.6	Comparison between the activity values calculated by Kromek MultiSpect, Scipy and the reference ones.	134
B.7	Comparison between efficiency values calculated for ^{152}Eu calibration source using different software.	136

Acknowledgements

First of all, I would like to thank Prof. Emilio Mariotti, my supervisor, and Dr. Alberto Andrichetto, my co-supervisor: under your guidance I learned the foundations of research and carried out the work described in this thesis. I thank Dr. Charlotte Duchemin and Dr. Thierry Stora for welcoming me into the MEDICIS group at CERN, where I was able to undertake an internship. I thank the Gamma group at LNL, who solved every problem I had with detectors with both expertise and kindness. I thank Prof. Marcello Lunardon and Prof. Sandra Moretto for giving me the opportunity to take part in many interesting activities. I thank the University of Siena for believing in my research project and for funding my PhD scholarship.

I thank the INFN National Laboratories of Legnaro for the wonderful working environment, canteen included. I thank my colleagues: Aurora, Massimo, Daiyuan, Alberto, and Omorjit, with whom it was a pleasure to work and play ping pong. I thank the ISOLPHARM group and the SPES group, whose members are always ready to help me and clear up my doubts. I thank all the engineers and technicians, without whom nothing beautiful can be accomplished. I thank my classmates from the University of Padova and those from Siena, with whom I shared, and overcame, many challenges.

I thank my big family for always being by my side. In particular, my parents, Roberta and Ezio, for studying with me and for their unconditional support. Thanks to my brother Andrea, whose determination is an example to follow. I thank Anita, Bruce, and Nerone for their warm company. I thank my friends, who have accompanied me on this long journey and will continue to do so: we were here, and we will be here in the future as well. Finally, a special thank you to Giulia, because her presence and her music have become an important part of my life. With you by my side, every day feels sunny.

Ringraziamenti

Prima di tutto, vorrei ringraziare il Prof. Emilio Mariotti, mio supervisore, e il Dott. Alberto Andrichetto, mio co-supervisore: sotto la vostra guida ho appreso le basi della ricerca e svolto il lavoro descritto in questa tesi. Ringrazio la Dott.ssa Charlotte Duchemin e il Dott. Thierry Stora per avermi accolto nel gruppo MEDICIS al CERN, dove ho potuto svolgere un periodo di tirocinio. Ringrazio il gruppo Gamma dei LNL, che ha risolto ogni mio problema sui detector con esperienza e disponibilità. Ringrazio il Prof. Marcello Lunardon e la Prof.ssa Sandra Moretto per avermi dato l'opportunità di fare molte attività interessanti. Ringrazio l'Università degli Studi di Siena per aver creduto nel mio progetto di ricerca e per aver finanziato la mia borsa di dottorato.

Ringrazio i Laboratori Nazionali di Legnaro dell'INFN per lo splendido ambiente di lavoro, mensa compresa. Ringrazio i miei compagni: Aurora, Massimo, Daiyuan, Alberto e Omorjit con cui è stato un piacere lavorare e giocare a ping pong. Ringrazio il gruppo ISOLPHARM e il gruppo SPES, i cui membri sono sempre disponibili ad aiutarmi e a fugare i miei dubbi. Ringrazio gli ingegneri tutti e i tecnici, senza i quali nulla di bello può essere realizzato. Ringrazio i miei compagni di corso dell'Università degli Studi di Padova e quelli di Siena, con i quali ho condiviso, e superato, molte difficoltà.

Ringrazio la mia grande famiglia per essermi stata vicino. In particolare, i miei genitori, Roberta e Ezio, per aver studiato con me e per il loro supporto incondizionato. Grazie a mio fratello Andrea, la cui determinazione è un esempio da seguire. Ringrazio Anita, Bruce e Nerone per la calorosa compagnia. Ringrazio i miei amici, che mi hanno accompagnato in questo lungo viaggio e continueranno a farlo: noi siamo stati qua e ci saremo anche in futuro. Infine, un ringraziamento speciale a Giulia, perché la sua presenza e la sua musica sono diventate parte importante della mia vita. Con te vicino, ogni giorno c'è il sole.

Chapter 1

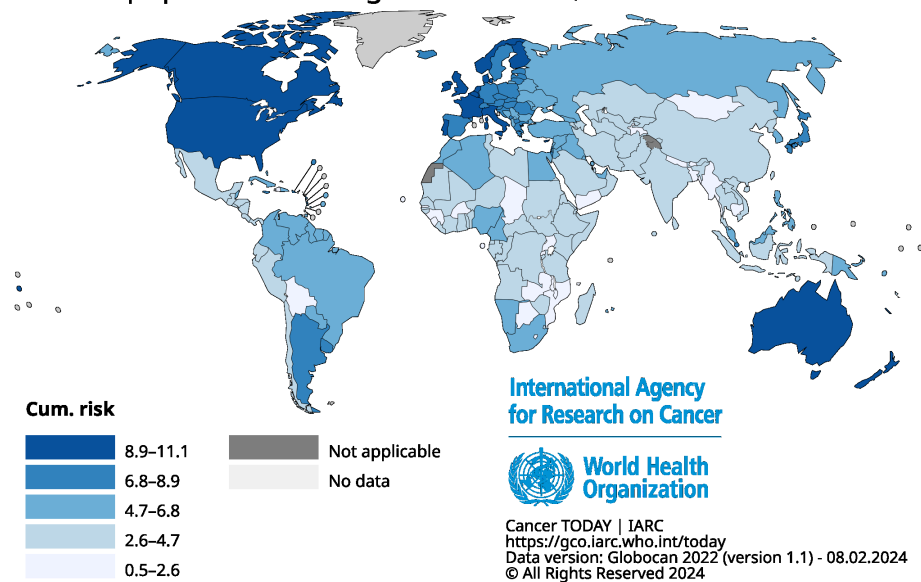
Introduction

1.1 Targeted Radionuclide Therapy

Cancer is a major cause of death in the world. For instance, in Italy about 9 female children out of 100 are expected to develop a breast cancer at some point of their life (Figure 1.1 [1]). Starting from surgery alone, the landscape of treatment modalities has grown considerably [2]. Several techniques that make use of ionising radiation have been developed, either using external or internal sources [3, 4]. The simplest way to perform internal radiotherapy with unsealed sources, is by coupling a radionuclide with a targeting moiety, such as a small drug-like molecule, a peptide or a monoclonal antibody (mAb). Depending on its features, the radionuclide can either be directly bonded to the targeting moiety or complexed with an appropriate chelator (in the case of radioactive metal ions) [5]. According to the targeting strategy employed, internal radiotherapy can be distinguished with different techniques, such as: Peptide Receptor Radionuclide Therapy (PRRT) or RadioImmunoTherapy (RIT). In this thesis the term Targeted Radionuclide Therapy (TRT) will be used, meaning a form of cancer treatment by administration of a radiolabelled molecule designed to seek out specific cells [6].

TRT is performed using radiopharmaceuticals, that are pharmaceuticals containing a radionuclide. These drugs accumulate preferentially on the membrane of the cancer cells or within them, with respect to normal cells. The radionuclide decays according to the exponential decay law (formulas in Appendix A). The resulting ionising radiation damage the DNA of the cancer cells leading to their death. The radionuclide is linked to a specific molecule (targeting agent) that preferentially binds to one of the receptors expressed by the cancer cells. In this way, the damage is localised to the tumour cells sparing as much as possible the surrounding healthy tissue.

Estimated cumulative risk (%) for breast cancer incidence in females population with age from 0 to 74, in 2022



All rights reserved. The designations employed and the presentation of the material in this publication do not imply the expression of any opinion whatsoever on the part of the World Health Organization / International Agency for Research on Cancer concerning the legal status of any country, territory, city or area or of its authorities, or concerning the delimitation of its frontiers or boundaries. Dotted and dashed lines on maps represent approximate borderlines for which there may not yet be full agreement.

Figure 1.1: Number of newborn female children out of 100 who are expected to develop breast cancer over a lifetime. Edited from [1].

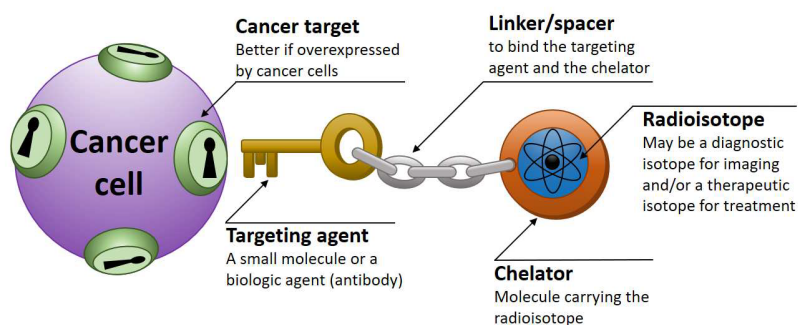


Figure 1.2: Schematic representation of a small-molecule radiopharmaceutical. From [7].

Figure 1.2 shows a small molecule radiopharmaceutical. New approaches to reduce the toxicity and maximise the therapeutic efficacy are continuously investigated. Recently the use of NanoParticles (NPs) as a vehicle for the radionuclides has been gaining interest from the community [8].

Each radionuclide has specific physical features: half-life, type of emission and energy. These features determine whether the radionuclide can be suitable for therapy or diagnosis [9]. On the other hand, the carrier molecule has specific chemical and biological behaviours that determine the radiopharmaceutical affinity and selectivity. In particular, with some specific radionuclides, TRT can be used for theranostics (or theragnostics) in nuclear medicine, that means to provide both tumour therapy and diagnosis [10]. Advancements in this field involve also:

- the design of new targeting vectors [11];
- the search for suitable radionuclides [12];
- the translation from research to clinical practice [13];
- the understanding of biological mechanism involved in tumour control [14];
- the quantification of the patient dose [15, 16];
- the development of technology for radionuclide production [17].

There exist several production methods for medical radionuclides. The most common ones are based on cyclotrons or nuclear research reactors. Alternatively, Isotopes Separation On-Line (ISOL) facilities for Radioactive Ion Beam (RIB) production can be used [18].

1.2 Novel Medical Radionuclides

Several radionuclides are well established for TRT, whereas others are currently emerging. ^{177}Lu is considered the gold standard among the beta-emitters, it is used in the commercial drug Pluvicto[®] targeting the Prostate-Specific Membrane Antigen (PSMA) [19]. Alpha-emitters are also studied for TRT; with respect to electrons, this type of radiation has a shorter pathlength ($\sim 50\text{ }\mu\text{m}$) and a higher Linear Energy Transfer (LET) ($\sim 80\text{ keV }\mu\text{m}^{-1}$) [20]. Based on these features, alpha-emitters can potentially have fewer side effects on the normal tissue surrounding the targeted cancer. For instance, ^{225}Ac Ac-PSMA-617 can be effective even in tumours that are resistant to ^{177}Lu Lu-PSMA-617 treatment [21]; Xofigo[®] radiopharmaceutical, based

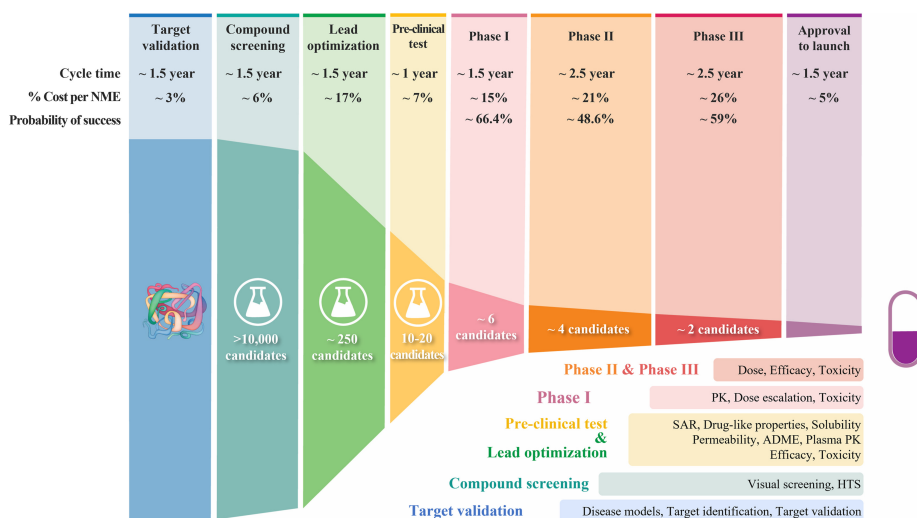


Figure 1.3: The steps necessary for drug discovery and development. The probability of success at each step is indicated. From [23].

on ^{223}Ra , has been approved for clinical treatment of prostate cancer bone metastases [22].

Developing a new radiopharmaceutical is a long and difficult process. A lot of tests have to be performed to assess its efficacy and non-toxicity. Figure 1.3 shows the steps necessary to complete the drug development starting from scratch. The typical total amount of time required to complete the process is about 14 years. Focusing only on the physical part related to the radionuclides, a candidate needs to fulfil a set of criteria [24]. The Linear Energy Transfer (LET) should be high enough to be able to localise the damage in the tumour tissue. The half-life should be in between one day and a couple of weeks to maximise the ratio between the dose delivered to the tumour and the one delivered to the healthy tissue. The production method should be able to provide radionuclides with high purity from several points of view: radionuclidic, radiochemical, elemental, and chemical. The presence of a gamma-ray decay branch is desirable to trace the radionuclide within a body. It should be possible to label a drug with the radionuclide. The cost of the radionuclide production should be affordable to pass from preclinical experiment to clinical use.

Imaging devices can be used in preclinical experiments to assess whether a candidate is suitable for the desired medical application. Beta-emitting radionuclides can be imaged by detectors sensitive to this type of radiation and similarly for gamma-emitting ones. Gamma-cameras are widespread in the scientific community, in particular as SPECT devices. Instead, devices

sensitive to beta-rays are much less used [25].

1.3 Radionuclide production

Radionuclides decay with an exponential trend characterised by a specific half-life. Therefore, radionuclides that can be found in nature, tend to have very long half-lives (such as thousands of years), or are stable. The dose, defined in Eq. (A.3), delivered outside the window for imaging or therapy needs to be as low as possible. For this reason, radionuclides with long half-lives are not suited for medical use and the production of short-lived ones is needed [26]. The two most common production methods employ either nuclear research reactors or cyclotrons [27]. Nuclear research reactors are widely employed as sources of neutrons. Via neutron capture reactions, neutron-rich radionuclides are produced. Moreover, the neutron flux can be used to induce fission, eventually producing unstable fragments. Cyclotrons can provide proton beams that, impinging on a target, induce nuclear reactions such as (p,n), (p, α). Cyclotrons enable the production of neutron-poor radionuclides. Alongside these well-established methods, Isotope Separation On-Line (ISOL) facilities can be used to produce radionuclides with high purity. This technique relies on a primary accelerator to induce nuclear reactions in a target and subsequently produce a Radioactive Ion Beam (RIB). Element-wise laser ionisation and mass separation enable high specific activities (defined in chapter A) for the collected samples; this technique will be described more in details in Section 2.1.

The amount N of a given radionuclide that can be accumulated in a generic production facility can be modelled with a differential equation that considers both the production rate P and the decay constant λ . Assuming that both the target material and particle flux are constant in time, the equation is

$$\frac{dN}{dt} = P - \lambda N \quad (1.1)$$

This is a linear, inhomogeneous Ordinary Differential Equation (ODE). Using the variation of constants methods, one can find a solution of the form

$$N(t) = \frac{P}{\lambda} + Ce^{-\lambda t} \quad (1.2)$$

where C is a constant. As a boundary condition, the amount of radionuclide is set to zero at the start. The solution in this case is

$$N(t) = \frac{P}{\lambda}(1 - e^{-\lambda t}) \quad (1.3)$$

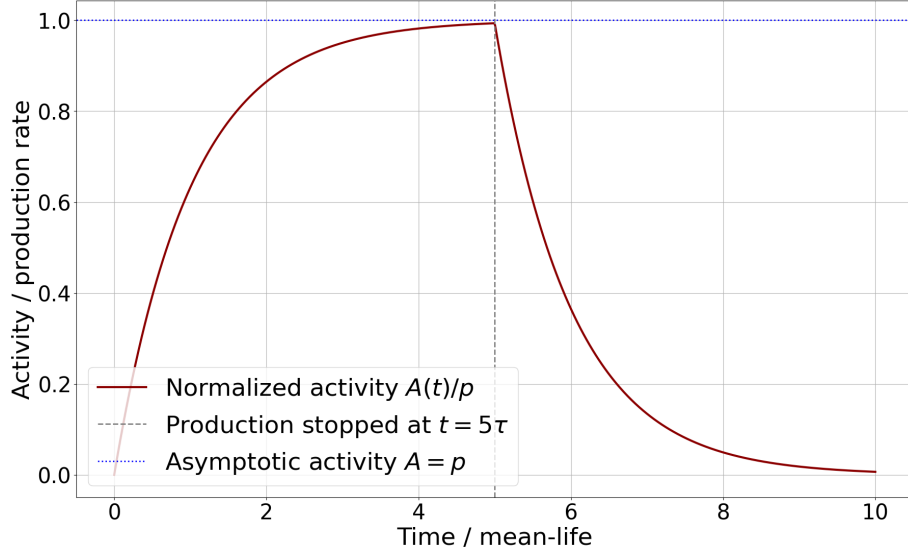


Figure 1.4: Production curve for a generic radionuclide according to Eq. (1.1).

and for the activity

$$A(t) = \underbrace{P}_{\text{production rate}} \cdot \underbrace{(1 - e^{-\lambda t})}_{\text{saturation factor}} \quad (1.4)$$

Studying this function, one can see that the maximum number of radionuclides that can be collected is determined by the combination of the production system (P) and the radionuclide decay constant.

$$N_{\infty} \equiv N(t) \xrightarrow{t \rightarrow +\infty} \frac{P}{\lambda} \quad (1.5)$$

Consequently, the activity is limited to:

$$A_{\infty} \equiv \lambda N_{\infty} = P \quad (1.6)$$

On the other hand, the system performance has no effect on the time at which a determined fraction F of the maximum amount is reached, it depends only on the radionuclide decay constant:

$$t_F \text{ for } \frac{N(t_F)}{N_{\infty}} \stackrel{!}{=} F \implies t_F = -\frac{\ln(1-F)}{\lambda} \quad (1.7)$$

Consequently, it is optimal to run the production facility only for a time as long as a few half-lives of the radionuclide. A curve of production valid for a generic radionuclide is shown in Figure 1.4.

A reaction cross section measures the relative probability for a reaction to occur, it can be defined as [28]

$$\sigma \equiv \frac{P}{I_a N_t} \quad (1.8)$$

where P is the production rate, I_a is the current of incident particles per unit time and N is the number of target nuclei per unit area that the beam sees. Then, the production rate of Eq. (1.4) can be expressed as

$$P = I_a \sigma N_t \quad (1.9)$$

In general, the cross section is a function of the incident particles energy and the produced particles have angular and energy distributions [29]. Although there exist some fields of research where studying the doubly differential cross section $d^2\sigma/dE_b d\Omega$ is relevant, for radionuclide production considering the integral over all the angles and energies is sufficient.

In a more realistic scenario, the production rate is not constant but instead depends on time $P(t)$. Such a time dependence commonly arises in nuclear reactors, where the neutron flux is sufficiently high to cause a macroscopic transmutation of the target material during irradiation. Another second-order effect that shall be considered is the destruction of the produced radionuclides due to reactions with the incoming beam. Adding these effects, Eq. (1.1) becomes [30]

$$\frac{dN}{dt} = N_{\text{target},0} e^{-\sigma_{\text{ab}} \phi t} - (\lambda + \sigma'_{\text{ab}} \phi) N \quad (1.10)$$

where $N_{\text{target},0}$ is the initial number of target nuclei, σ_{ab} is the absorption cross section causing target destruction, ϕ is the flux of incoming particles, σ'_{ab} is the absorption cross section causing produced-nuclei destruction. The target destruction can be neglected if

$$\sigma_{\text{ab}} \phi t \ll 1 \quad (1.11)$$

The destruction of the produced radionuclides can be neglected if

$$\frac{\sigma'_{\text{ab}} \phi}{\lambda} \ll 1 \quad (1.12)$$

For the cases described in this thesis (Section 2), these effects can be safely neglected.

Cyclotrons are typically used to produce neutron-deficient isotopes decaying via beta plus (β^+) emission or Electron Capture (EC) [31]. Most of the

cyclotrons designed for producing medical radionuclides accelerate protons only. The largest part of the radionuclides of interest can be produced via proton-induced reactions. Nonetheless, there exist also cyclotrons able to accelerate deuterons, ${}^3\text{He}^{2+}$ and alpha particles, such as the ARRONAX cyclotron at Nantes [32].

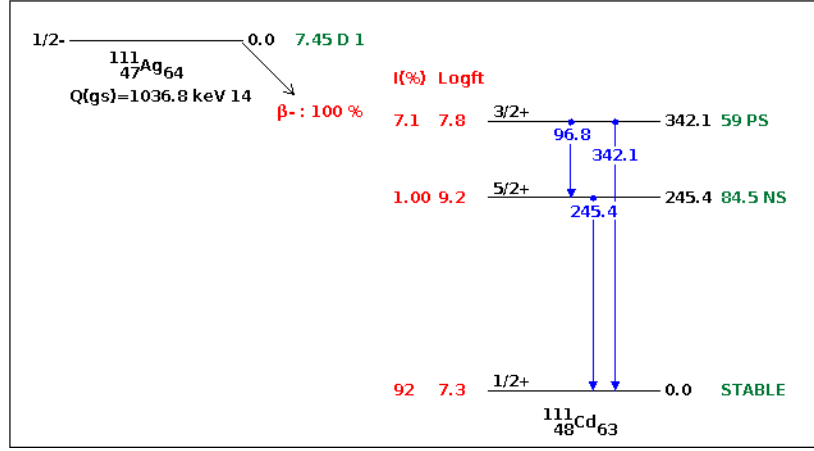
The neutron flux available in nuclear reactors can be used to produce neutron-rich radionuclides [33]. The target material is inserted in a sealed container that is placed close to the reactor core. The nuclear reactions triggered by the neutrons flux lead to the production of radioactive nuclides [30]. The radiative capture reaction (n,γ) is one of the most used reactions. It is triggered mainly by the thermal neutrons, which are in thermal equilibrium with the molecules of the surrounding medium. At a temperature of 20°C , thermal neutrons have energy of $\sim 0.025\text{ eV}$.

Beyond these two standard methods, radionuclides can be produced in ISOL facilities, where protons impact on, e.g., uranium carbide targets. This type of facilities typically produces radionuclide samples with high specific activity (no-carrier-added). The element selection is offered by the Resonant Ionisation Laser Ion Source (RILIS), which ionises only the isotopes that are compatible with the chosen ionisation scheme. A Wien Filter and a magnetic dipole select only the isobars of a specific mass. This technique will be presented more in details in Section 2.1, in particular for the case of the SPES ISOL facility at INFN-LNL [34].

1.4 The ISOLPHARM project

The ISOLPHARM project was launched in 2014 with the aim of producing radionuclides of medical interests using the ISOL technique. The fission of UC_x targets triggered by the impact of the high-energy protons, enables the access to a wide gamma of radionuclides. Within this plethora of species, about 60 of them have properties that can be interesting for medical applications or are already used in clinical practice; examples of clinically-relevant radionuclides are ${}^{89}\text{Sr}$, ${}^{90}\text{Y}$, ${}^{125}\text{I}$, ${}^{131}\text{I}$, ${}^{133}\text{Xe}$ [7]. The ISOL production of radioPHARMaceutical (ISOLPHARM) is planned at the SPES facility [35]. In the last 8 years, the project focused on investigating the potential of a new radiopharmaceutical based on ${}^{111}\text{Ag}$.

${}^{111}\text{Ag}$ is on the neutron-rich side of the Segrè chart, it decays on ${}^{111}\text{Cd}$ with a half-life of 7.45 d. The decay has a Q-value equal to 1036.8 keV. In 92 % of the decay events, the process is ground state to ground state, so the end-point of the energy spectrum of the emitted electron is equal to the Q-value. In the remaining percentage of the events, the daughter ${}^{111}\text{Cd}$

Figure 1.5: Decay Scheme of ^{111}Ag . From [36].

nucleus is produced in one of the two different excited states. Consequently, the end-points of the emitted electrons for these decay branches are smaller because the excitation energy is dissipated as a gamma-ray emission. In other words, two gamma rays at 342 keV and 245 keV are emitted with a probability of 6.7 % and 1.2 % respectively. Figure 1.5 shows the ^{111}Ag decay scheme; the 97 keV gamma ray generated in the transition between the two excited states of ^{111}Cd has low intensity (~ 0.1 %), therefore it will not be further considered.

The total number of Auger electrons has a probability smaller than 0.27 %, so their biological effect is negligible. Same goes for Conversion Electrons (CE), that are produced with an intensity of about 0.26 %. The main decay features of ^{111}Ag are reported in Table 1.1 and compared to the ones of beta-emitter radionuclides approved for clinical use or under clinical investigation. The list comprehends radionuclides used in the following drugs: REYOBIQTM (^{186}Re), SIR-Spheres[®] (^{90}Y), QUADRAMET[®] (^{153}Sm), MetastronTM (^{89}Sr), AZEDRA[®] (^{131}I), PLUVICTO[®] and LUTATHERA[®] (^{177}Lu).

Figure 1.6 shows the comparison between the energy spectra of the electrons emitted by ^{111}Ag and other radionuclides that are considered for or have already been approved for TRT. ^{186}Re , used for palliative treatments of cancer, has a spectrum similar to ^{111}Ag [38]. As a matter of fact, the main β^- -decay of ^{186}Re has an end-point energy of 1072 keV; this value is close to the correspondent main branch of ^{111}Ag : 1036 keV. The data are calculated using the BetaShape software [37]. ^{111}Ag has already been considered for radiosynovectomy against rheumatoid arthritis and SPECT imaging of this radionuclide has already been proved feasible [39].

Isotope	Half-life	Type	Mean Energy (keV)	Intensity (%)
^{111}Ag	7.45 d	β^-	360	92
		γ	342	6.7
		γ	245	1.2
^{177}Lu	6.64 d	β^-	149	79
		γ	208	10
		γ	113	6
^{131}I	8.02 d	β^-	192	89
		γ	364	82
		γ	637	7
		γ	284	6
^{153}Sm	46.3 h	β^-	225	49
		β^-	199	30
		β^-	264	19
		γ	103	29
		γ	69	4.7
^{186}Re	3.72 d	β^-	360	71
		β^-	307	21
		γ	137	9.4
^{89}Sr	50.5 d	β^-	587	100
^{90}Y	64.1 h	β^-	932	100

Table 1.1: Radioactive decay features of some radionuclides of interest. Information extracted from the NuDat database [36].

From a more general point of view, the ISOLPHARM name comprehends the following list of approved and funded experiments (Figure 1.7):

ISOLPHARM_Ag From 2018 to 2019, a two-year INFN *Commissione Nazionale Scientifica 5* (CSN5) experiment with the aim of studying and demonstrating the feasibility of the production and use of ^{111}Ag .

ISOLPHARM_EIRA From 2020 to 2022, a three-year INFN CSN5 experiment that started the first in vitro and in vivo studies toward a preclinical experimental phase for ^{111}Ag

ADMIRAL From 2023 to 2025, a three-year INFN CSN5 experiment aimed at probing the diagnostic and therapeutic potential of ^{111}Ag

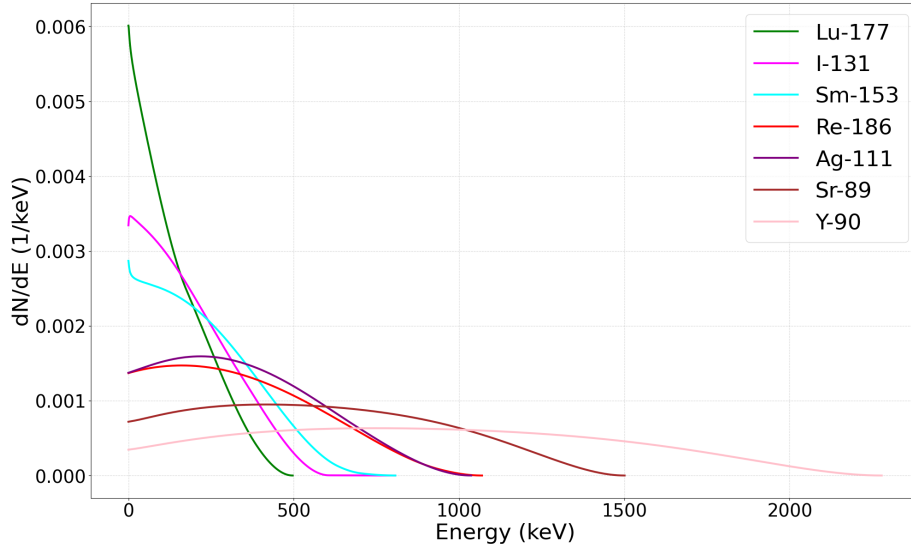


Figure 1.6: Comparison of the electrons energy spectrum of ^{111}Ag with the ones of β -emitting radionuclides used for cancer therapy. Data are obtained from the BetaShape software [37].



Figure 1.7: Logos of the ISOLPHARM experiments.

ISOLPHARM_CORE From 2024 to 2025, a two-year *Progetti di Rilevante Interesse Nazionale* (PRIN) project funded by the Italian *Ministero dell'Università e della Ricerca* (MUR) and devoted to support the technological aspects in the medical radionuclides ISOL production at SPES

SPES_MED From 2025 to 2027, a three-year INFN CSN3 experiment that will estimate yields for the production of several radionuclides at SPES

ISOLPHARM denotes also an experimental station present in a dedicated beamline (the ISOLPHARM beamline) of the SPES facility at INFN-LNL. This experimental station is designed to collect the radionuclides produced

with the ISOL technique and to perform a first characterisation of the obtained activity. The ISOLPHARM beamline is part of the low-energy experimental area of the facility. A phase of the SPES project, called SPES- γ , is devoted to the production of medical radionuclides.

1.5 Geant4 Monte Carlo simulations

Simulations are a powerful tool in this field of research. In particular, in this thesis work, the Geant4 software was used to support several experiments. This is a toolkit to simulate the passage of particles in matter [40, 41, 42]. Many fields of research use this toolkit, such as: nuclear and high energy physics, space science and medical physics. Following the increasing trend on computational power available for research, the use of simulations has become more and more prominent. In the ISOLPHARM research context, several experimental setups have a corresponding simulation framework. These *digital twins* can be used to predict experimental outcomes and optimise construction parameters.

Geant4 is based on C++ programming language and it uses its object-oriented programming paradigm. For instance, a type of object that is present in the software is the `G4Track`. As the name suggests, it represents the track described by a particle from its generation to its deletion. Also particles have their software counterpart, e.g. the electrons are described by the `G4Electron` class. As in a real experiment, the first necessary step for a simulation is the generation of the experimental apparatus. The volumes representing the various elements of the apparatus are built in the user-defined `G4VUserDetectorConstruction` class. Once the materials are set, the experimental run (`G4Run` class) can start. In a run, a certain number of particles is generated and their interaction with matter is recorded. The features of the particles to be generated (such as its energy, position, and momentum direction) are set in the `G4VPrimaryGenerator` class. Every generated particle is independent from the other ones and the information regarding particle-matter interactions are stored in a dedicated container (`G4Event` class). In Geant4, the user can decide which physics mechanisms are relevant for the application and include them. For instance, working with radionuclides, importing the `G4RadioactiveDecay` class is convenient to include all the radioactive decay-related processes. The interesting information resulting from the simulation can be stored for analysis in a ROOT output file [43].

As an example, Figure 1.8 compares the energy spectra of beta-rays emitted in the decay of ^{111}Ag as calculated by the BetaShape software and

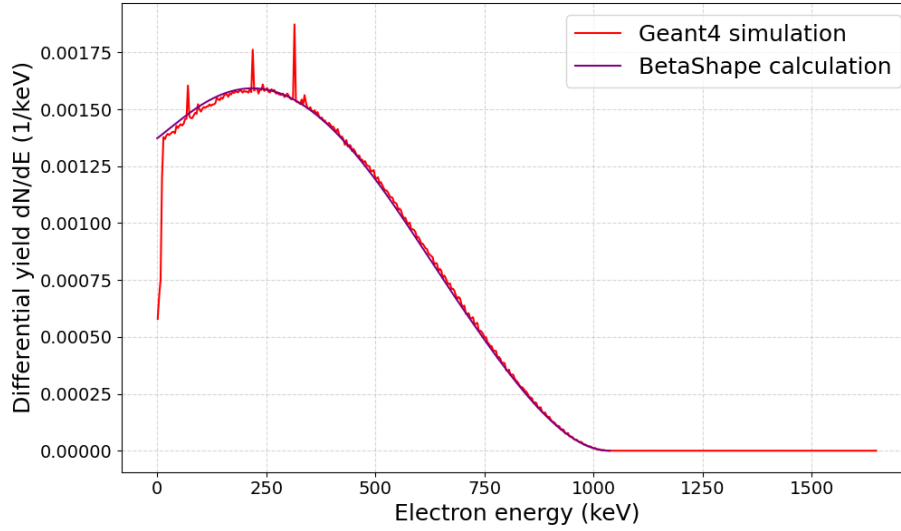


Figure 1.8: Comparison between BetaShape and Geant4 ^{111}Ag beta-rays energy spectra.

as simulated by the Geant4 software. Geant4 includes the CE electrons, but their contribution is a small percentage with respect to the total. The difference visible at 10 keV may be due to differences in the screening calculation algorithms. In addition to the generation of beta-rays, Geant4 can also simulate their interaction with matter, providing insight of real experimental apparatus.

1.6 Thesis results

This PhD thesis summarises an all-round work that involved several aspects of radiopharmaceutical production within the ISOLPHARM project. Each one of the four numbered chapters of this thesis will cover one of the main lines of research. Given the width of the topics involved in the project, the ISOLPHARM collaboration is a multi-disciplinary environment with experts contributing from different fields: from physics to chemistry, biology, engineering and pharmaceuticals. Consequently, the work here described has a strong inter-disciplinary character.

First, the production of radionuclides at the SPES facility at INFN-LNL is discussed. The ISOLPHARM experimental setup for radionuclide collection (IRIS) was installed at the SPES experimental hall for low energy RIB and characterised. The software needed for operating the system and measure the relevant physical quantities was developed. IRIS will

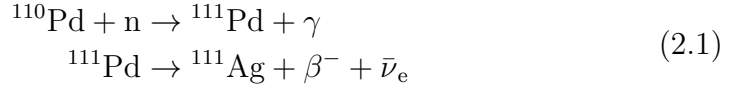
be able to supply the desired radionuclides to the users. In particular, the ISOLPHARM project is interested in ^{111}Ag , that is currently supplied by the LENA laboratory of Pavia. The suitability of this radionuclide for theranostic is under investigation. To aid these studies, a novel beta detector (DUMBO) sensitive to the electrons emitted by ^{111}Ag was designed and realised. The core element of this device is a pixelated sensor derived from High-Energy Physics. To host the sensor a unique motorised frame was assembled and the readout is performed using a dedicated electronics front-end. Due to the physical properties of the ^{111}Ag beta-rays branches, increasing the sample-detector distance, DUMBO spatial resolution drops. Another device, sensitive to the gamma-ray radiation, can be used to perform imaging of ^{111}Ag from a different type of radiation. The ISOLPHARM collaboration designed and built a gamma-camera suitable to the energy of ^{111}Ag gamma-rays. The choice of the construction parameters was driven by the results obtained in a simulation framework prepared with the Geant4 toolkit. Finally, the potential of ^{111}Ag as a radiotracer was proved by a series of preclinical experiments. While testing the feasibility of imaging ^{111}Ag in a murine model, the biodistribution of this radionuclide with no targeting agent was studied.

Chapter 2

The ISOLPHARM experimental station

^{111}Ag production at LENA

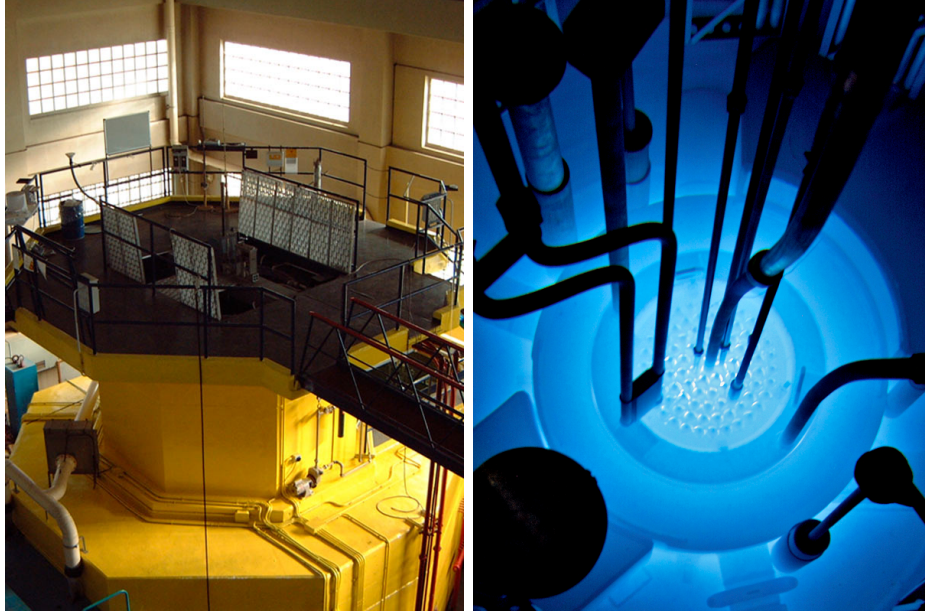
The ^{111}Ag for the ISOLPHARM activities is currently supplied by the Laboratorio di Energia Nucleare Applicata (LENA) of Pavia University [46]. In this laboratory, a TRIGA Mark II nuclear research reactor (see Figure 2.1) can be used to produce ^{111}Ag through the following reaction:



The ^{111}Pd decays to ^{111}Ag with a half-life of 24 min. Targets of natural palladium contain mainly ^{106}Pd (27.33 %), ^{108}Pd (26.46 %) and ^{105}Pd (22.33 %), while ^{110}Pd is only a small fraction (11.72 %). When natural palladium targets are used, all the stable isotopes undergo radiative neutron capture

Isotope	Abundance (%)	Reaction	Cross section (mb)
^{102}Pd	1.02	$^{102}\text{Pd} \xrightarrow{\text{n},\gamma} {}^{103}\text{Pd} \xrightarrow{\text{EC}} {}^{103}\text{Rh}$	180
^{104}Pd	11.14	$^{104}\text{Pd} \xrightarrow{\text{n},\gamma} {}^{105}\text{Pd}$	75
^{105}Pd	22.33	$^{105}\text{Pd} \xrightarrow{\text{n},\gamma} {}^{106}\text{Pd}$	217
^{106}Pd	27.33	$^{106}\text{Pd} \xrightarrow{\text{n},\gamma} {}^{107}\text{Pd} \xrightarrow{\beta^-} {}^{107}\text{Ag}$	29
^{108}Pd	26.46	$^{108}\text{Pd} \xrightarrow{\text{n},\gamma} {}^{109}\text{Pd} \xrightarrow{\beta^-} {}^{109}\text{Ag}$	868
^{110}Pd	11.72	$^{110}\text{Pd} \xrightarrow{\text{n},\gamma} {}^{111}\text{Pd} \xrightarrow{\beta^-} {}^{111}\text{Ag}$	340

Table 2.1: Radiative neutron capture reactions for natural Palladium isotopes. Adapted from [45].



(a) Picture of the reactor.

(b) Picture of the nuclear reactor core.

Figure 2.1: Nuclear research reactor of the LENA laboratory at Pavia. From [44]

(the (n,γ) reaction), as summarised in Table 2.1. In particular, the neutron irradiation of the palladium isotopes with mass number 106 and 108 produces unstable isotopes, which decay into stable silver isotopes, thereby reducing the specific activity (defined in Sec. A.4) of ^{111}Ag [45]. To avoid these contaminants, enriched palladium targets with abundances of ^{110}Pd as high as 99.4% can be employed [46].

The palladium target is positioned in the central thimble of the reactor. The neutron flux in this position is about $1.7 \times 10^{13} \text{ cm}^{-2} \text{ s}^{-1}$. After several hours of irradiation ($< 1 \text{ d}$), the activated target is retrieved. Considering these parameters and the cross sections in Table 2.1, the target transmutation described in Eq. (1.10) can be neglected. Similarly, the product burn-up via neutron capture of ^{111}Ag , with cross section $< 1 \text{ b}$, is negligible [47].

The produced silver nuclides are separated from the palladium substrate using a chromatographic column. First, the solid target is dissolved using aqua regia, then it is evaporated by heating. The residue is dissolved with Hydrochloric acid (HCl) and evaporated many times. An ion-exchange chromatography column is prepared using a LN resin. The solution with 0.005 M HCl is loaded in the column: ^{111}Ag fixes on the resin and is eluted

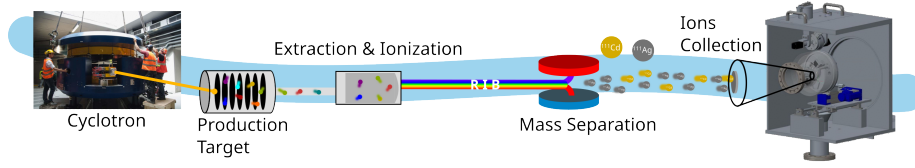


Figure 2.2: Diagram representing the steps for radionuclide production via ISOL technique as applied in the SPES facility.

with 1 M HCl. This production route for ^{111}Ag , with similar steps for the chemical separation, has already been described in literature [33, 48].

Within the ISOLPHARM context, preclinical experiments were run with the solution containing ^{111}Ag prepared with the protocol described above. The outcome of these experiments suggested that a palladium contamination was present even after the separation step provided by the chromatographic column. Since palladium can have biological effects in mice injected with the solution, tests were run to determine whether the contamination by Pd (about hundred of μg) was present in the eluted sample with ^{111}Ag . This measurement was carried out using the Neutron Activation Analysis (NAA) technique. The sample was irradiated a second time at the TRIGA reactor and its energy spectrum was analysed to identify the elements contained within it. The characteristic peak at 88 keV of ^{109}Pd was observed, indicating the presence ^{108}Pd in the sample, which was activated by the neutron flux.

Therefore, a new protocol was developed by adding a second ion-exchange column step. The eluted sample of 1 M HCl with ^{111}Ag is evaporated and redissolved in 0.005 M HCl. The solution is loaded in the column and rinsed with 0.005 M HCl to remove as much palladium as possible. Following elution with 1 M HCl, ^{111}Ag is collected again. The irradiation with neutron is repeated for the ^{111}Ag sample obtained with this protocol. In the energy spectrum the presence of ^{109}Pd is no longer visible, proving that the amount of Pd contained in the solution is below the detector sensitivity.

2.1 ISOL radionuclide production at SPES

The ISOL technique

Isotope Separation On-Line (ISOL) is a well-established technique to produce Radioactive Ion Beams (RIBs). It features beams with small emittance and high purity [49]. The technique requires several steps [50, 51]:

1. the primary beam impinges on a target;

2. the produced nuclei are transferred to the ions source;
3. the neutral products are selectively ionised;
4. the ions are accelerated by an electrical potential difference and form a beam;
5. the beam undergoes a mass selection step;
6. the purified beam is collected on an implantation substrate.

Figure 2.2 represents the steps mentioned above on a facility layout, namely for the SPES case.

Several sites around the world adopt the ISOL technique to produce radionuclides. As an example, in the European Organization for Nuclear Research (CERN) site there is the MEDical Isotopes Collected from ISolde (MEDICIS) facility, that is dedicated to the production of medical radionuclides [52, 53]. MEDICIS has been operating since its commissioning in 2017 and has provided its partner institutes with non-conventional medical radionuclides, such as ^{149}Tb , ^{152}Tb , ^{155}Tb , ^{153}Sm , ^{165}Tm , ^{167}Tm , ^{169}Er , ^{175}Yb , and ^{225}Ac . The produced radionuclides features the high specific activity enabled by the ISOL technique.

Appendix B presents a report that describes the characterisation of a gamma-ray detector for activity quantification employed at MEDICIS [54]. This type of detector is placed close to the irradiation site to provide online activity estimation. This solution and other methods that are used during operations at MEDICIS, has been considered during the development and design of the collection station at SPES.

The SPES case

At the Legnaro National Laboratories of the Italian Institute for Nuclear Physics (INFN-LNL), a facility named Selective Production of Exotic Species (SPES) for RIB production with ISOL technique is under commissioning. The layout is depicted in Figure 2.3 and will be described in this section. SPES primary accelerator is a cyclotron for protons only, that is able to provide $750\text{ }\mu\text{A}$ of beam current with energies between 35 and 70 MeV. The proton beam produced by the cyclotron is directed toward the Target Ion Source (TIS), where it impinges on a multi-disc target to produce the radionuclides of interest via nuclear reactions. The target is maintained at high temperature (about $2000\text{ }^{\circ}\text{C}$) to promote the diffusion of radionuclides through the material and their subsequent effusion into the transfer line. The effused nuclides then reach the ion source, where they are ionised. An

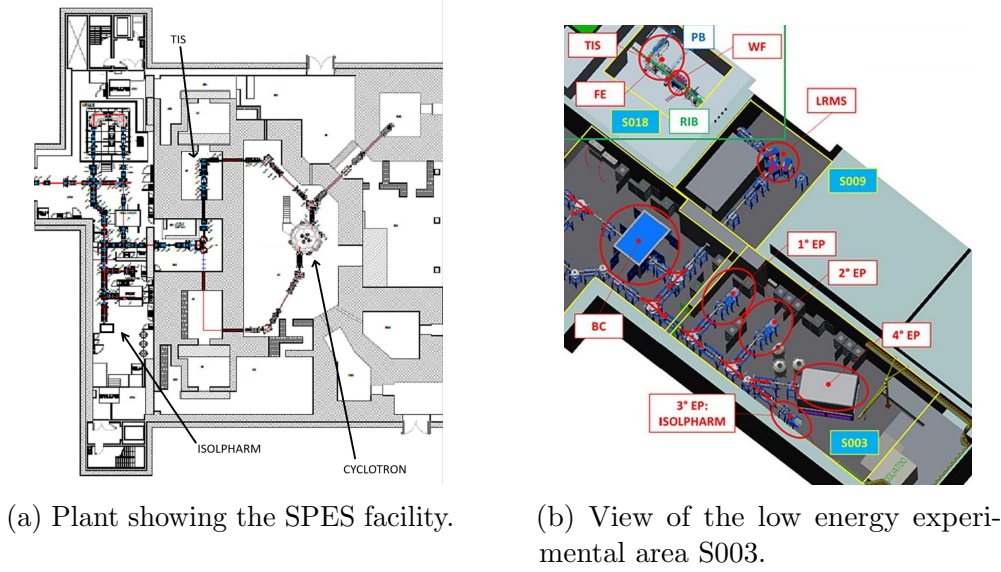


Figure 2.3: Layout of the SPES facility. From [55].

electrical potential difference accelerates the ions forming the Radioactive Ion Beam (RIB). In the low-energy experimental area, three experimental stations are available: the SPES Tape Station (STS), the β -decay tape station dedicated to nuclear physics research and the ISOLPHARM station for radionuclide production.

The SPES target maximises the nuclides production by absorbing almost all the power of the primary proton beam. This result is achieved using a multi-foil layout [57, 58]. In this facility, three types of ion sources will be used:

- Surface Ion Source (SIS);
- Plasma Ion Source (PIS);
- Resonant Ionisation Laser Ion Source (RILIS).

Each source has its own advantages and disadvantages. To get pure RIBs for medical radionuclide production, the latter is the most suitable one, since it can selectively ionise the isotopes of a specific element [59, 60]. The working principle behind this type of ion source is described in section 2.2. Figure 2.4 shows a section of the 3D model for the TIS unit mounting a PIS.

The RIB extracted by the TIS enters the Low-Resolution Mass Separator (LRMS) system, where the resolution in the selected mass reaches $\Delta M/M = 1/200$. The LRMS is made of a Wien Filter (WF) and a magnetic dipole [61,

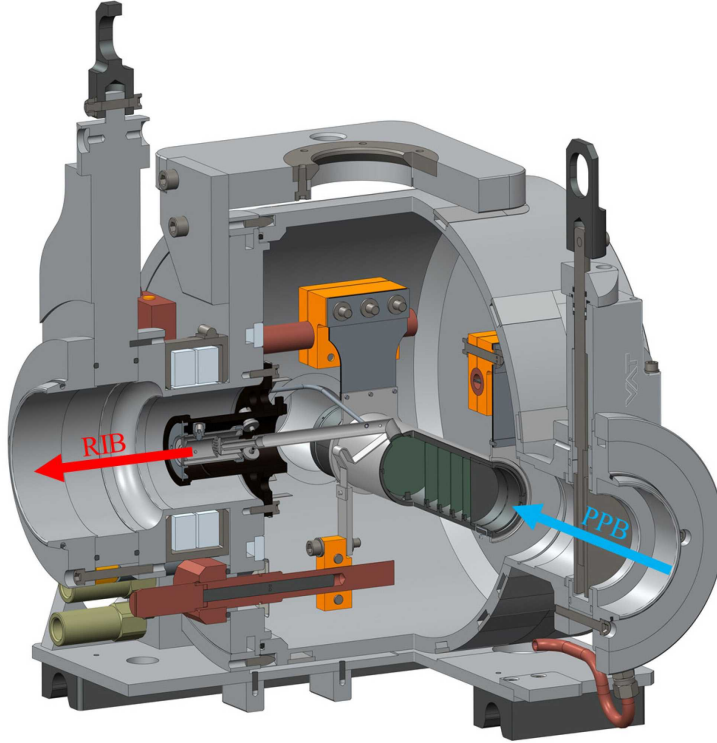


Figure 2.4: Representation of the 3D model of the Target Ion Source (TIS) unit mounting a Plasma Ion Source. PPB is the Primary Proton Beam and RIB is the Radioactive Ion Beam. From [56].

62]. The working principle of these systems is based on the well-known Lorentz force

$$\vec{F} = q(\vec{E} + \vec{v} \times \vec{B}) \quad (2.2)$$

The beamline is equipped with electrostatic deflectors and quadrupole triplets, which have the advantage of being mass-independent.

The ISOL technique, together with a UC_x target, enables access to a large number of radionuclides. Among the ones that are produced with sufficiently high rate, the medical physics community is interested in those with half-life and decay features that are useful for medical applications. The list of the suitable ones is summarised in Figure 2.5. The ISOLPHARM project recognised ^{111}Ag as the most promising theranostic candidate; the physical characteristics of this radionuclide are summarised in Table 1.1. ^{111}Ag is produced at SPES through the following reaction:



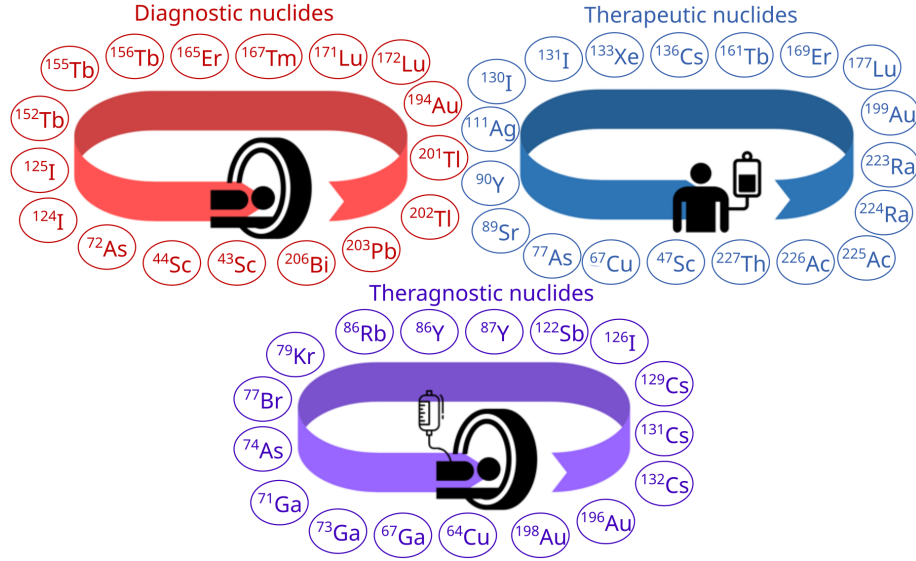


Figure 2.5: Radionuclides of possible medical interest that can be produced at SPES. Adapted from [7].

Natural uranium has 99.27 % of ^{238}U and 0.72 % of ^{235}U . Instead, the SPES target are made of depleted uranium, with a reduced quantity of ^{235}U , as low as 0.2 % [63]. Since the ISOL-produced RIB undergoes a mass selection phase, the contaminants that do not belong to the beta decay chain of ^{111}Ag are discarded. In particular, the stable silver isotopes are discarded. Therefore, the ISOL technique offers a viable production route for ^{111}Ag . This alternative is particularly relevant given the age of the LENA nuclear reactor, which will eventually enter a decommissioning phase.

For proton projectiles with energy between 35 and 70 MeV, the independent cross section for the production of ^{111}Ag via proton-induced fission of ^{238}U varies between 1×10^{-4} and 1×10^{-1} mb. These cross section data are available in the EXFOR database and are plotted in Figure 2.6 [64, 65, 66].

Experimental beamlines at SPES

The mass-selected RIB is directed to the experimental area, where it is characterised using the diagnostic beamline elements and the tape station. Once characterised, it can be directed to the ISOLPHARM station to collect the selected radionuclides. The SPES Tape Station (STS) is a system featuring a Mylar tape that can be rolled. The tape is in vacuum and the beam can be implanted directly onto it. At the implantation site, a beta detector and a germanium gamma-ray detector can be used to characterise

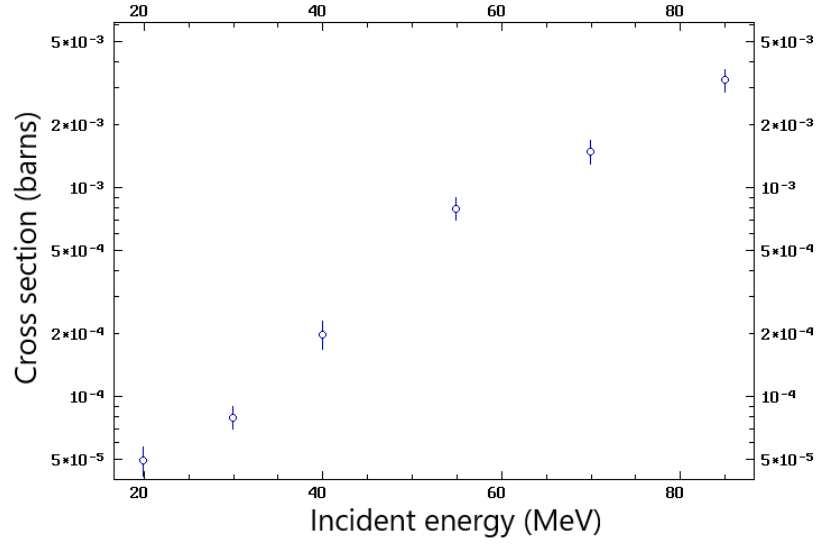


Figure 2.6: Experimental values for the independent cross section of the nuclear reaction producing ^{111}Ag via fission induced by protons on a ^{238}U target nucleus. From the EXFOR database [64, 65, 66].

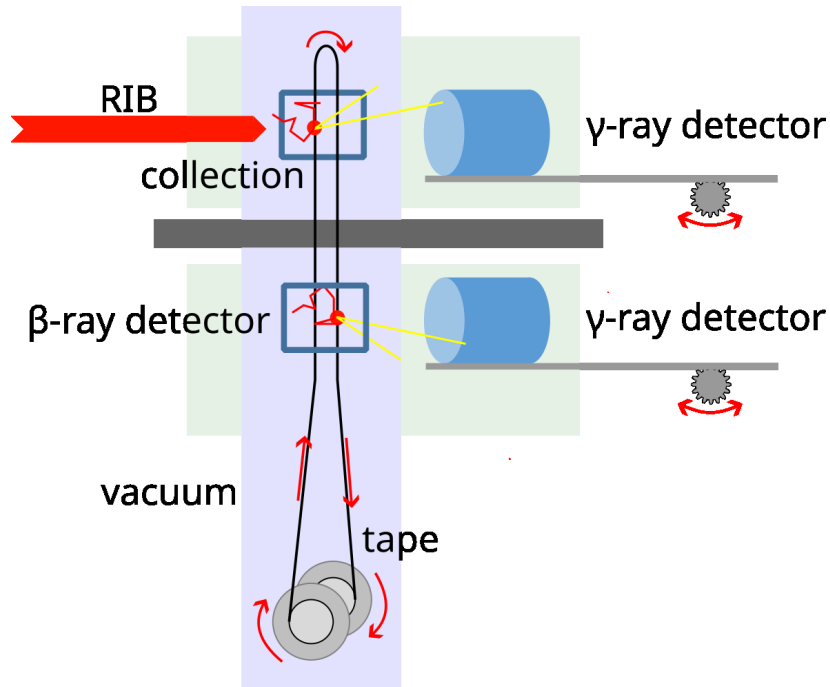


Figure 2.7: SPES Tape Station scheme. Adapted from [67].

the beam. The deposited radioactive sample can be moved into a shielded area by rolling the tape; here, a similar β - γ detector configuration can be used. A scheme with the main STS elements is represented in Figure 2.7. Coherently with the rest of the SPES equipment, the STS control system is based on Experimental Physics and Industrial Control System (EPICS) and the Graphical User Interface (GUI) on the Phoebus version of the Control System Studio (CS-Studio) toolset [68].

With short-lived radionuclides, the collection and measurement on a tape is performed on a cyclic fashion. Each cycle has a duration of the same order of magnitude of the half-life of the species under observation.

2.2 Resonant Ionisation Laser Ion Source

The Resonant Ionisation Laser Ion Source (RILIS) was chosen as the most suitable ion source to produce medical radionuclides with high specific activity and low chemical contaminations. In this section, the working principle behind this ion source is described.

Laser photo-ionisation

Consider an atom or molecule with two energy levels E_1 and E_2 . The molecule in the ground state E_1 has a certain probability to absorb a photon of energy $h\nu = E_2 - E_1$ and pass to the excited state E_2 [69]:

$$\frac{d}{dt}\mathcal{P}_{12} = B_{12}\rho(\nu) \quad (2.4)$$

This excitation process is called *induced absorption*. If the upper energy state is above the minimum energy required to remove the most loosely bound electron (the valence electron) then the atom is ionised. Wavelength-tunable lasers (meaning *Light Amplification by Stimulated Emission of Radiation*) can generate photons with the desired frequency within a certain range. In particular, the photon energy can be matched (resonance) to the gap energy for the transition of interest. The lasers excite the atom resonantly via intermediate atomic states and eventually ionise it [70].

RILIS at SPES

Figure 2.8 represents the scheme of the ion source used at ISOLDE (and similarly at SPES) that implements the laser-induced excitation. In the Resonant Ionisation Laser Ion Source (RILIS), a laser beam is sent through

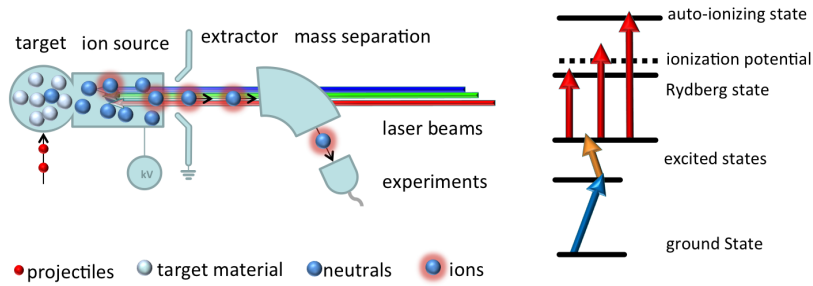


Figure 2.8: Scheme of the RILIS technique. The blue and yellow arrows indicates the excitation between atomic levels induced by the lasers and the third transition delivers the ionisation. From [71].

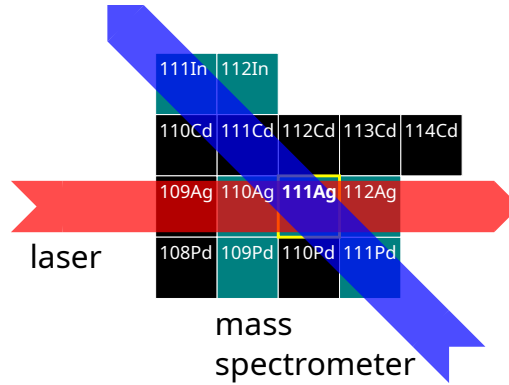


Figure 2.9: Schematic representation of the combination of isobaric selection, provided by the mass separator, and isotopic selection, achieved through laser photo-ionisation. The combined selectivity enables the collection of a specific radionuclide, such as ^{111}Ag .

the vapour of neutral atoms to ionise the selected species via subsequent resonant excitation steps. The theory of stepwise photo-ionisation was described first by Letokhov in 1972 [72].

In principle, combining the chemical-selectivity of the Resonant Ionisation Laser Ion Source (RILIS) with the mass-selectivity of the LRMS, a specific nuclide can be collected, as shown in Figure 2.9.

Laser spectroscopy

A ionisation scheme for the radionuclide of interest ^{111}Ag (and in general for silver) was studied in the SPES offline laser laboratory [60]. The selected scheme requires two resonant lasers tuned at frequencies 328.163 nm and 421.402 nm, as shown in Figure 2.10. The third step necessary to overcome

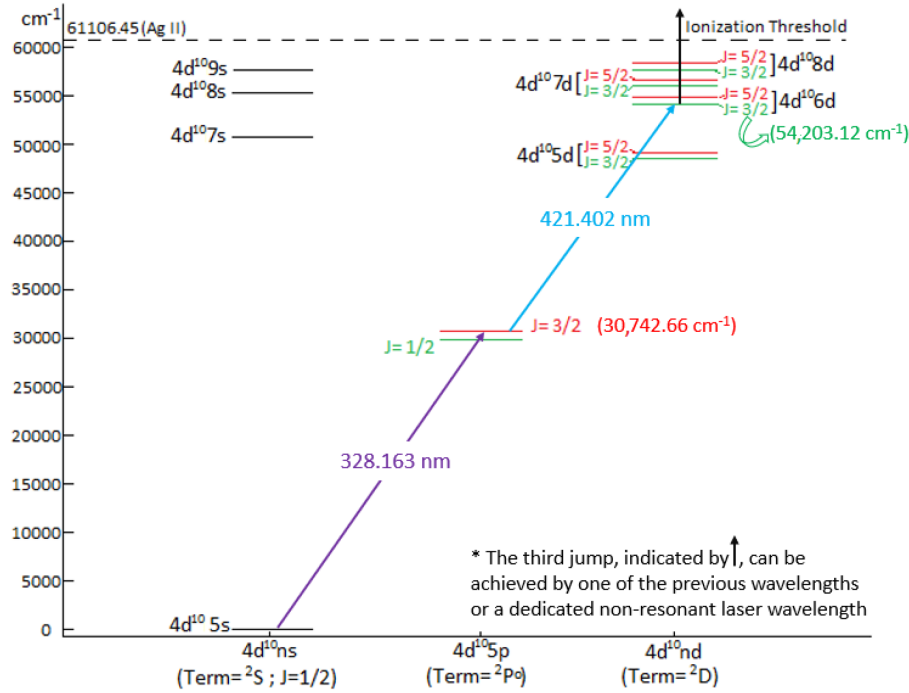


Figure 2.10: Selected excitation path for silver with corresponding energy levels. From [73].

the ionisation potential is provided by any photon of the previous excitation steps [73]. Two dye lasers were used to provide the resonant photons. Both lasers are pulsed, with a repetition rate of 10 Hz and a pulse duration of 20 ns.

The first transition was driven by a Quantel TDL 50 dye laser pumped by a Quantel YG 580 laser at 532 nm. The dye solution used was sulforhodamine 640 with methanol solvent. This dye laser was tuned at 656.326 nm; a Second Harmonic Generation (SHG) crystal was used to double the frequency, producing a UV light at 328.163 nm. The fundamental beam was sent to a HighFinesse WS7 wavemeter to monitor the wavelength.

The second transition was driven by a Lambda Physik FL2002 dye laser pumped by a Quantel YG 980 at 355 nm. The dye solution used was Stilbene 420 with methanol solvent. This dye laser was tuned at 421.402 nm.

The silver vapour was generated by directing a Nd:YAG ablation laser at 1064 nm onto a solid silver target. The pump lasers and the ablation laser were time-synchronised and the resonant laser intersected inside the ablation plume. A Time Of Flight Mass Spectrometer (TOF-MS) measured the ions signal.

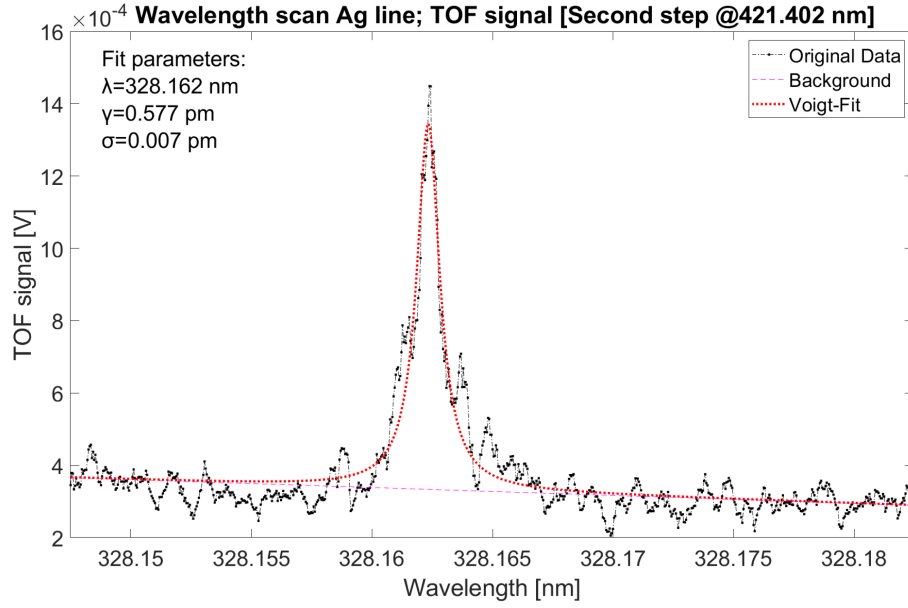


Figure 2.11: Graph representing the 28 pm scan for the first transition, while keeping the second transition fixed at 421.402 nm. From [73].

The resonance of the first transition can be recognised in Figure 2.11. The resonance profile is fit with a Voigt function, that is a convolution between a Gaussian curve and a Lorentzian curve.

$$V(x; \sigma, \gamma) = \int_{-\infty}^{+\infty} G(x'; \sigma) L(x - x'; \gamma) dx' \quad (2.5)$$

The Gaussian part has contributions from the Doppler broadening and the laser linewidth. The Lorentzian curve has contributions from the natural linewidth and the power broadening.

For both the Gaussian and Lorentzian curves, the FWHM can be expressed with simple relations based on a single characteristic parameter:

$$\text{FWHM}_{\text{Gaussian}} \approx 2.355\sigma \quad (2.6)$$

$$\text{FWHM}_{\text{Lorentzian}} = 2\gamma \quad (2.7)$$

An approximated formula for the FWHM of the Voigt curve is [73]

$$\begin{aligned} \text{FWHM}_{\text{Voigt}} \approx & 0.5346 \cdot \text{FWHM}_{\text{Lorentzian}} \\ & + \sqrt{0.2166 \cdot (\text{FWHM}_{\text{Lorentzian}})^2 + (\text{FWHM}_{\text{Gaussian}})^2} \end{aligned} \quad (2.8)$$

Using the parameters obtained from the fit of the spectrum in Figure 2.11, the FWHM of the Voigt curve results ~ 1.2 pm.

The natural linewidth for the investigated transition can be calculated from the transition probability A_i

$$\text{FWHM}_{\text{natural}} = \frac{A_i}{2\pi} \quad (2.9)$$

Using the data available in the Lines Data of the National Institute of Standards and Technology (NIST) Atomic Spectra Database (ASD) [74], the natural linewidth results ~ 8.0 fm.

The Doppler broadening can be calculated with [69]

$$\text{FWHM}_{\text{Doppler}} = \frac{2\nu_0}{c} \sqrt{\frac{2RT \ln 2}{M}} \quad (2.10)$$

where R is the gas constant, c is the speed of light and M is the molecular mass (107.87 g/mol for natural silver). In the temperature T range from 300 K (environmental temperature) to 3000 K, the Doppler width is in the range [0.2, 0.7] pm.

The power broadening increase the natural linewidth of the transition according to

$$\text{FWHM}_{\text{power}} = \text{FWHM}_{\text{natural}} \sqrt{1 + \frac{I}{I_{\text{sat}}}} \quad (2.11)$$

where I is the laser intensity at the central frequency of the transition ν during the pulse, and I_{sat} is the saturation intensity. For the case here discussed, the latter is calculated as

$$I_{\text{sat}} = \frac{\pi h A_i \nu^3}{3c^2} \quad (2.12)$$

where h is the Planck constant; resulting $8.3 \times 10^2 \text{ W m}^{-2}$. The laser has an average power of 20 μW and a beam diameter of 0.6 mm. The resulting laser peak intensity I is 198 MW m^{-2} . Then, the power-broadened linewidth is estimated to be as large as 4 pm, which exceeds the measured value reported above. This overestimation is likely due to the use of simplified formulas in a multi-level scheme. Nonetheless, this rough calculation indicates that power broadening contributes to the width of the observed Voigt profile comparably to the laser linewidth, which is about 1.1-1.2 pm at the central frequency of 328.163 nm.

The laser system of the SPES offline laser laboratory is versatile and enables the study of the ionisation schemes of different elements by tuning the wavelengths of the dye lasers. One of the limits of this experimental set-up is the maximum number of steps allowed: with two dye lasers available, only two resonant transitions can be provided. Three-steps schemes can be studied



Figure 2.12: Picture of the SPES online laser laboratory.

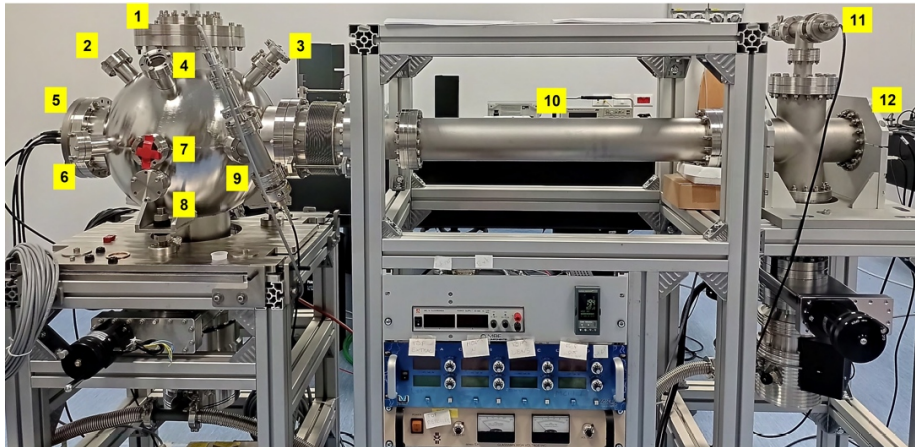


Figure 2.13: Picture of the Time Of Flight Mass Spectrometer (TOF-MS) present in the SPES online laser laboratory. The numbered tags indicate the main elements of the system and are described in detail in [60].

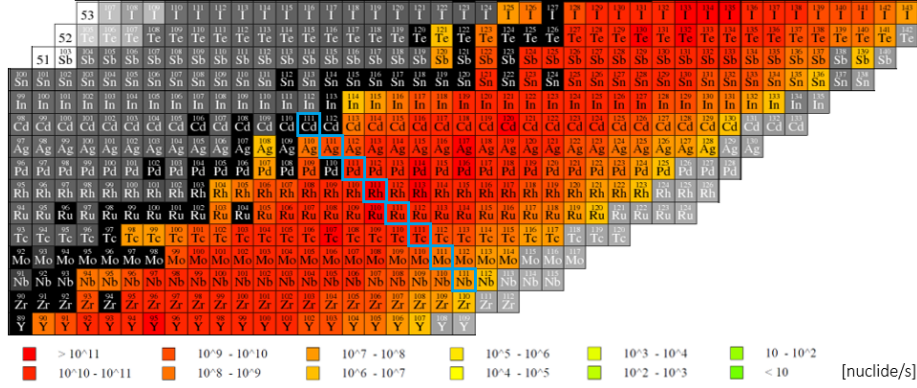


Figure 2.14: In-target production rates for fission of UC_x induced by a 40 MeV, 200 μA proton beam, calculated with FLUKA code. The isobars that belong to the β -decay chain that leads to ^{111}Ag are highlighted by blue frames. Adapted from [7].

in the SPES online laser laboratory, which hosts three Titanium:Sapphire (Ti:Sa) laser sources [75], shown in Figure 2.12. Similarly to the configuration adopted in the offline laser laboratory, the spectroscopy studies can be performed with two modalities: using a Hollow-Cathode Lamps (HCL) or using a TOF-MS. The TOF-MS, shown in Figure 2.13, was recently installed and is an upgraded version of the one available in the offline laser laboratory [60]. Notably, the control software for the Ti:Sa lasers has to be adapted for wavelength scans since it was supplied specifically for operating the lasers at fixed wavelengths. The software is written in LabVIEW and its source code is available for modifications.

2.3 Production estimation

The range of products available with the ISOL technique depends on the proton beam and the target material. The SPES commissioning plan foresees the sequential use of silicon, titanium and uranium carbides (SiC, TiC and UC_x respectively) [57]. Figure 2.14 shows the production rates for a 40 MeV, 200 μA proton beam impinging on the SPES UC_x target. These values are calculated using the FLUKA code [76]. As in Eq. (1.9), the production rate in-target P_{in} is given by the product between the number of incoming protons per unit time I_p , the reaction cross section σ and the number of target nuclei N_t per unit area:

$$P_{in} = I_p \sigma N_t \quad (2.13)$$

In real cases, this formula has to be corrected for the dependence of the cross section on the incident particles energy. In a thick target, the energy of the beam decreases as it crosses the material. Consequently, the formula can be expressed as:

$$P_{\text{in}} = I_p \rho \frac{N_A}{M} \int_{E_0}^{E_s} \frac{\sigma(E)}{-dE/dx} dE \quad (2.14)$$

where $-dE/dx$ is the stopping power of the incident particles in the target material.

In order to be used, the produced nuclei must travel through the entire beamline to reach the user setup. Consequently, the production rate available for the user is [77]

$$\begin{aligned} P &= P_{\text{in}} \epsilon_{\text{tot}} \\ &= I_p \sigma N_t \epsilon_{\text{tot}} \\ &= \frac{I}{q} \sigma \rho \Delta x \overbrace{\frac{N_A}{M}}^{N_t} \overbrace{\epsilon_{\text{target}} \epsilon_{\text{source}} \epsilon_{\text{transp}} \epsilon_{\text{collec}}}^{\epsilon_{\text{tot}}} \end{aligned} \quad (2.15)$$

where I is the proton beam current in A and q is the charge of a proton; σ is the cross section in barns; N_t is the number of target nuclei that are within the cross section Σ of the beam; ρ , Δx are the density, thickness of the target nuclei; M is the molecular mass of the Uranium atoms and N_A is the Avogadro constant. The yield for the user-available production is

$$Y = Y_{\text{in}} \epsilon_{\text{tot}} \quad (2.16)$$

where the *in-target yield* Y_{in} is the number of products normalised with the number of incoming particles [78].

After production, the radioactive nuclei need to diffuse from the target material and effuse toward the ion source. A necessary condition to avoid losing nuclei before beam formation, is that the transfer time from production to ionisation is less than or comparable to the half-life of the desired nuclide. As a matter of fact, the refractory elements are very difficult to observe since their release and transfer efficiency is very low [79]. Even if medical radionuclides have half-lives of at least about one hour, they can still be trapped in the material if they form chemical compounds or if they get stuck in closed porosities. For the release of ^{111}Ag , an experiment was conducted to study the compounds released from a graphite substrate where natural silver was deposited and heated up to 2000°C . The observed mass scan spectrum suggests that no volatile silver complexes were formed [7]. The ion



Figure 2.15: β decay chain with ^{111}Ag as daughter nucleus. From [36].

source ionises the neutrals of interest with efficiency ϵ_{source} . This efficiency depends on the ion source type; in general, it is strongly related to the chemical properties of the isotope (Z number). Passing through the beamline optics and through the mass separation stage, some beam particles are lost; the transport efficiency ϵ_{transp} accounts for these losses. Nuclear physics users of ISOL facilities are typically interested in detecting exotic beams; for these users, the detector efficiency ϵ_{det} must be taken into account. Instead, Eq. (2.15) represents the case of radionuclide production for subsequent applications; therefore, the last efficiency term is the collection efficiency ϵ_{collec} . This term accounts for the effect of the collimator placed just before the implantation site and for the self-sputtering effect.

Regarding the in-target production, it is important to underline that a specific nuclide can be produced both directly (thus as a product of the proton-target reaction) and indirectly. The latter means that the desired nuclide is the daughter nuclide of one or more radionuclides that are directly produced. Figure 2.15 shows the decay chain of β decays that produces ^{111}Ag (and consequently ^{111}Cd). The contribution to the production rate from the decay of parent nuclei can be even larger than the direct production itself, and it can be calculated using the Bateman equations [80].

For the production of ^{111}Ag at SPES, the following parameters can be used: proton current 200 μA ; proton energy 40 MeV; cross section for $^{238}\text{U}(\text{p},\text{F})^{111}\text{Ag}$ with 40 MeV protons equal to 2×10^{-4} b; uranium carbide density 13.6 g cm^{-3} ; single disk thickness 1.3 mm; total number of disks 7; molar mass for UC_4 286 g/mol; fraction of ^{238}U 83.2%. Using analytical

	half-life	nuclides/proton
^{111}Ag	7.4 d	$3.9(7) \times 10^{-7}$
^{111}Pd	23.6 min	$1.31(1) \times 10^{-5}$
^{111}Rh	11 s	$7.83(2) \times 10^{-5}$
^{111}Ru	2.1 s	$4.50(2) \times 10^{-5}$
^{111}Tc	350 ms	$1.28(1) \times 10^{-5}$
^{111}Mo	186 ms	$7.6(3) \times 10^{-7}$

Table 2.2: In-target production yields for ^{111}Ag radioactive isobars. Data from [81].

formulas to estimate the expected rate of production in-target for ^{111}Ag introduces several simplifications. Therefore, the Monte Carlo simulation software FLUKA was used to provide the ^{111}Ag activity estimation after 7 days of irradiation, eventually resulting in 83.0(5) GBq in-target. Notably, the direct production rate for ^{111}Ag is two order of magnitude smaller than the ones for the other isobars: ^{111}Pd , ^{111}Rh , ^{111}Ru , ^{111}Tc . Since these isobars have half-lives from few seconds to 23 min for β decay, they contribute to the production rate of ^{111}Ag . Table 2.2 reports the in-target yields for these radionuclides, data are from [81]. Assuming a total efficiency ϵ_{total} of 30 %, the expected collected activity of ^{111}Ag available for users is 24.9(2) GBq.

2.4 Collection on the SPES Tape Station

The typical cycle for a tape station is structured with the following steps:

1. during the time T_{irr} , radionuclides are produced in target, extracted and collected on the tape station;
2. during the time T_{tape} , the collected nuclides are moved from the irradiation spot to the detection position via tape rolling;
3. during the time T_{meas} , the detectors acquire the signal from the radioactive sample.

These steps are schematised in Figure 2.16. The formula used to estimate the production rate is [82]:

$$P = \lambda \frac{1}{\epsilon_{\text{tot}}(1 - e^{-\lambda T_{\text{irr}}})} \frac{1}{e^{-\lambda T_{\text{tape}}}} \frac{N_{\gamma}}{\epsilon_{\gamma} \Gamma_{\gamma}(1 - e^{-\lambda T_{\text{meas}}})} \quad (2.17)$$

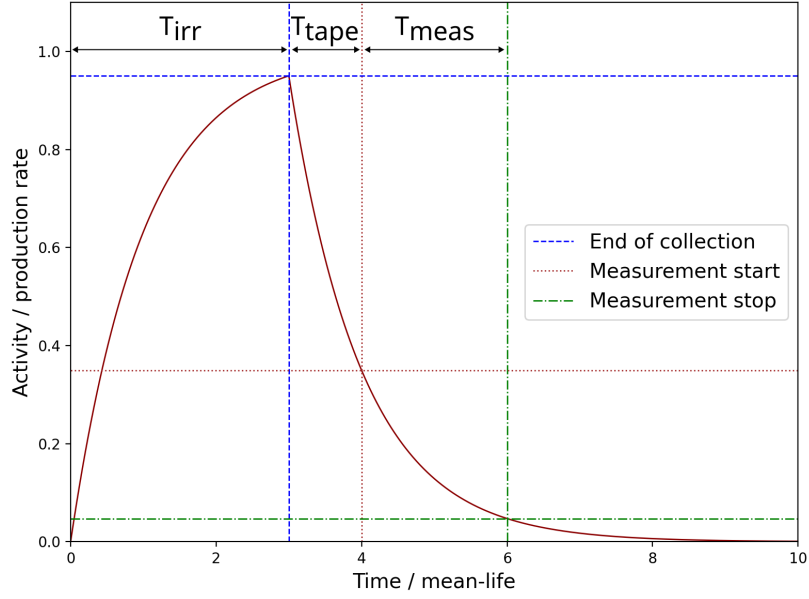


Figure 2.16: Measurement scheme for a tape station cycle.

where N_γ is the area of the full-energy peak of interest, ϵ_{tot} is the overall efficiency of the beamline described in Eq. (2.15). The detector absolute efficiency and the branching ratio for the gamma-ray of interest are indicated with ϵ_γ and Γ_γ respectively.

A second possibility is to use the detector system facing the irradiation site; in this case, the tape is not moved and the acquisition system of the STS is always active. The number of decay events per cycle is

$$\frac{N_{\text{dec}}}{N_c} = \int_0^{T_{\text{on}}+T_{\text{off}}} \lambda N(t) dt = \int_0^{T_{\text{on}}} \lambda \frac{P}{\lambda} (1 - e^{-\lambda t}) dt + \int_0^{T_{\text{off}}} \lambda \frac{P}{\lambda} (1 - e^{-\lambda T_{\text{on}}}) e^{-\lambda t} dt \quad (2.18)$$

where the number of nuclei at the start of the decay phase is equal to the number of nuclei accumulated at the end of the production phase:

$$N_{\text{off}}(t=0) = \frac{P}{\lambda} (1 - e^{-\lambda T_{\text{on}}}) \quad (2.19)$$

Solving both integrals is straightforward and leads to the following result

$$\frac{N_{\text{dec}}}{N_c} = \frac{P}{\lambda} (\lambda T_{\text{on}} + e^{-\lambda(T_{\text{on}}+T_{\text{off}})} - e^{-\lambda T_{\text{off}}}) \quad (2.20)$$

The time of a cycle can be defined as

$$T_c = T_{\text{on}} + T_{\text{off}} \quad (2.21)$$

On the other hand, the number of events detected in the full-energy peak is

$$N_\gamma = N_{\text{dec}} \Gamma_\gamma \epsilon_\gamma \quad (2.22)$$

Therefore, the production rate can be estimated

$$P = \lambda \frac{N_\gamma}{\Gamma_\gamma \epsilon_\gamma} \frac{1}{N_c} \frac{1}{\lambda T_{\text{on}} + e^{-\lambda T_c} - e^{-\lambda T_{\text{off}}}} \quad (2.23)$$

This formula can be applied independently by the half-life of the radionuclide. Dealing with radionuclides of medical interest, the half-life is typically at least a few hours. Therefore, acquiring multiple cycles is not necessary, and the formula can be simplified to the single-cycle case by imposing $N_c = 1$:

$$P = \lambda \frac{N_\gamma}{\Gamma_\gamma \epsilon_\gamma} \frac{1}{\lambda T_{\text{on}} + e^{-\lambda T_c} - e^{-\lambda T_{\text{off}}}} \quad (2.24)$$

2.5 IRIS development and installation

Design of a radionuclide implantation station

The ISOLPHARM Radionuclide Implantation Station (IRIS) development and installation has been described in a work recently submitted for publication and in Daiyuan Chen's PhD thesis [83, 81]. As the name suggests, IRIS setup is dedicated to the collection and characterisation of the radionuclides produced with the ISOL technique. The IRIS core is a tablet onto which the purified RIB impinges, implanting the radionuclides. Once the collection is over, a gamma-ray detector is used to quantify the amount of activity collected. After this Quality Control (QC) step, the radionuclide is available to be used for further studies. The development and installation of IRIS at SPES was planned and funded in the framework of two projects: the SPES-MED experiment and the ISOLPHARM-CORE PRIN project, described in the introduction.

Prior the IRIS design, a manual system for radionuclide collection only was foreseen [84]. In order to minimise the time spent close to the radioactive source by an operator and to provide QC, IRIS was designed [85, 86]. This setup features a set of mechanical and electronic components that move the tablets from the loading site to the irradiation site, then to the QC site, and finally to the shielded container. Figure 2.17 shows the status of the

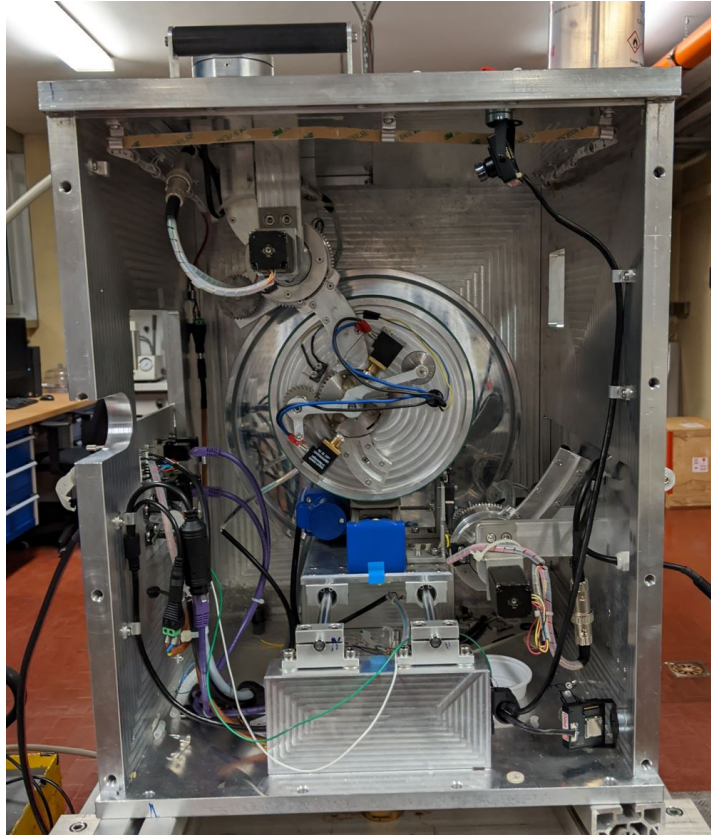


Figure 2.17: Picture showing the implantation station part of IRIS while decoupled from the beamline.

guides and buffers when the system was decoupled from the beamline. The motion is driven by a set of stepper motors and a pair of solenoids. Led strips and a set of Closed Circuit TeleVisions (CCTVs) were installed in some specific sites to monitor the critical points of the system. A dedicated electronic system was developed to power and control these elements. The control system interacts with the SPES Machine Protection System (MPS) to prevent IRIS operations from damaging the SPES beamline. To enable users to operate the machine easily, a simple Graphical User Interface (GUI) was developed. IRIS can be divided in two main parts: the Implantation Station (IS), where the RIB is stopped by a tablet, and the Offline Detection System (ODS), where the collected radioactive sample is characterised.

Implantation tablets

The tablets are realised with polymeric organic material in order to reduce the sputtering effect and maximise the collection efficiency of Eq. (2.15). Two types of material are currently considered: HydroxyPropyl MethylCellulose (HPMC) and Sorbitol (S100). The materials are available as pharmaceutical-grade powders. To prepare a tablet a well-defined amount is weighed (for instance 250 mg) and inserted into a stamp with 13 mm diameter. The stamp is placed in a manual press so that a specific pressure (for instance 10 t) is applied for a specific time (for instance 1 min). Tablets realised with this procedure and with these two materials have good mechanical resistance: they can fall from a height of two meters without breaking. This requirement is necessary to prevent the tablets from breaking during the loading phase. After irradiation, the deposited nuclides have to be extracted; this extraction is performed by dissolving the tablets in ultrapure water under magnetic stirring. The HPMC tablets slide more easily in the system guides, and they release the accumulated material in water by swelling. The S100 tablets exercise more friction when sliding but they dissolve very fast in water: less than 2 minutes [87]. The thickness of the tablets is a fundamental parameter for proper operation: if the tablets are too thick, they can cause jamming; if they are too thin, multiple tablets may overlap, also causing jamming. Via trial and error, the optimal thickness was determined to be 1.1(1) mm, where the uncertainty indicates that values in the range [1.0, 1.2] mm are still acceptable. Considering the density of S100, 1.40 g/cc, the optimal mass of powder to be weighed is 204(19) mg for each tablet. The relevant slides for the loading phase are shown in Figure 2.21b.

Operational workflow

Figure 2.18 shows the terminal part of the SPES beamline at 0° in the low energy experimental area. IRIS is attached to a diagnostic box, which is in turn connected to the SPES beamline through a gate valve. Since the diagnostic box is equipped with a turbo pump, IRIS can be vented and pumped back into vacuum independently of the SPES beamline. The setup features a sliding flange that allows the IRIS chamber to switch between two possible configuration:

- open chamber: the system is in air and decoupled with respect to the SPES beamline; the tablets can be loaded and unloaded;
- closed chamber: the system can be pumped into vacuum to perform the irradiation.

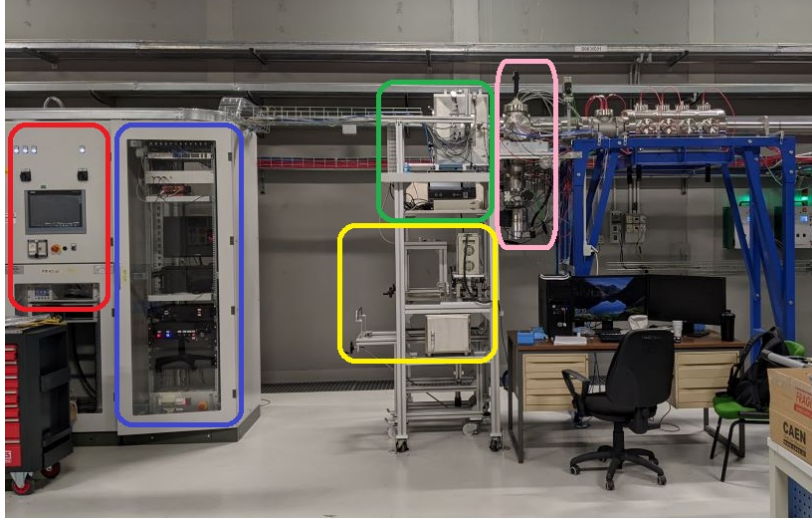


Figure 2.18: The ISOLPHARM Radionuclide Implantation Station (IRIS) at SPES. Colored rectangles indicate specific elements: red and blue are the vacuum and user racks; green and yellow are the collection and QC parts of IRIS; pink is the diagnostic box.

The irradiated tablets are unloaded one at a time to perform gamma-ray spectrometry on each tablet separately. After the QC, the tablets are dropped inside a vial that is placed in a shielded container mounted on a trolley. The trolley can be used to move the irradiated tablets to other sites, such as a radiochemical laboratory where the radionuclide of interest can be isolated. A lead safe is available right below the ODS to host the irradiated tablets.

Detectors for radionuclide characterisation

For the QC, two different gamma-ray detectors can be used: an inorganic scintillator and a germanium. The inorganic scintillator features a Lanthanum BromoChloride (LBC) crystal coupled to a Hamamatsu H15265-100-01 photomultiplier tube assembly with Super BiAlkali (SBA) photocathode. The germanium is a Mirion Reverse Electrode coaxial Ge detector (REGe™) GR3021 electrically cooled with the Mirion Cryo-Pulse 5 Plus cryostat. This pair of detectors, aimed at quantifying the activity at the end of a collection, constitutes the Offline Detector System (ODS).

A CAEN DT5780N module supplies the High Voltage (HV) needed to operate the germanium: -4500 kV. The same module is used as a digitizer (2 channels 14-bit 100 MS/s) for the energy signal coming out of the germanium

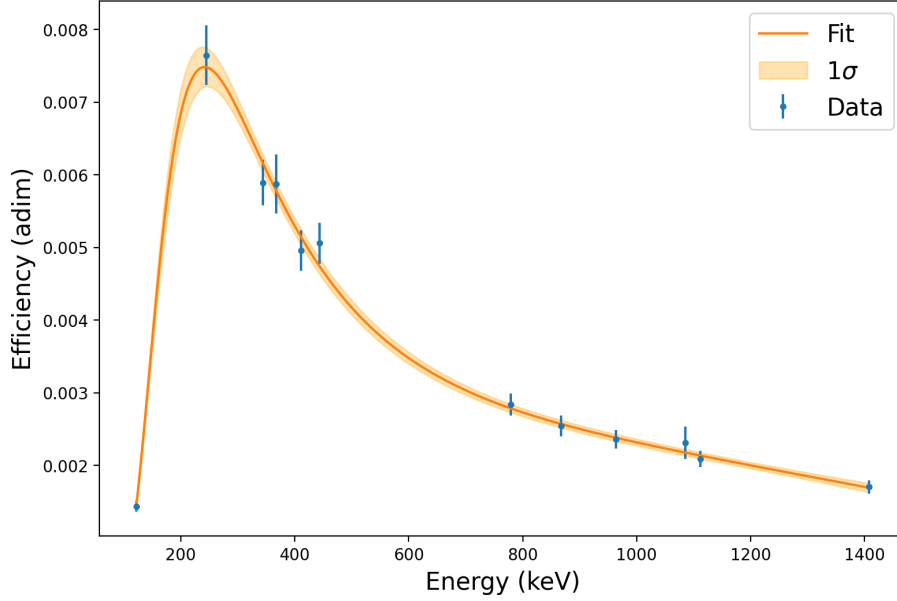


Figure 2.19: Efficiency curve of the IRIS germanium detector; the fit is performed using the logarithmic polynomial described in Eq. (2.25).

preamp. This signal is analysed through the Digital Pulse Processing for the Pulse Height Analysis (DPP-PHA) firmware. The second HV output is used to supply the LBC, operating at -1000 kV. The current drain at the operational point is $250\text{ }\mu\text{A}$ for the LBC and less than 100 nA for the germanium.

The LBC signal collected from the anode output of the PhotoMultiplier Tube (PMT) assembly is fed to a CAEN DT5725S (8 Channel 14-bit 250 MS/s Digitizer) that performs Digital Pulse Processing for Charge Integration and Pulse Shape Discrimination (DPP-PSD). CAEN CoMPASS software is used to set the HV and acquire the energy spectra. The remote control option can be enabled to set up, start and stop acquisitions directly from the GUI [88].

The germanium is the main detector, as it provides better energy resolution than the LBC, which can be used as a spare. Furthermore, having two detectors allows for coincidence measurements of gamma-rays. The LBC can also be used to monitor the intensity of the source, in order to avoid using the germanium to acquire samples that would have acquisition rates exceeding 10 kHz . Figure 2.19 shows the absolute efficiency of the germanium detector at the position closest to the sample. The function

Parameter	Value (adim)
a_0	$-4.90(3)$
a_1	$-0.13(9)$
a_2	$-1.95(6)$
a_3	$1.7(2)$
a_4	$-0.44(7)$

Table 2.3: Parameters for the fit of the absolute efficiency of the germanium shown in Figure 2.19.

used for the fit is

$$\ln \epsilon = a_0 + a_1 \ln \frac{E}{E_0} + a_2 \left(\ln \frac{E}{E_0} \right)^2 + a_3 \left(\ln \frac{E}{E_0} \right)^3 + a_4 \left(\ln \frac{E}{E_0} \right)^4 \quad (2.25)$$

where ϵ is the full-energy peak absolute efficiency; the energy E is normalised with $E_0 = 250$ keV to have an adimensional argument for the logarithm and to reduce the correlation between the parameters; a_i are constants [89]. The parameters a_i that fit the experimental data are reported in Table 2.3. For the energy of the main decay branch of ^{111}Ag (342 keV), the absolute efficiency for the full-energy peak is about 0.6 %.

As a future upgrade, the germanium detector will be moved to a position close to the irradiation site to enable monitoring of the activity build-up during the irradiation phase. Furthermore, the acquisition could benefit of a beta detector to perform β - γ coincidences to improve the Signal to Noise Ratio (SNR) in the energy spectra.

Control software for operations

As for the STS control system, the IRIS control system is based on EPICS and the GUI on the Phoebus version of CS-Studio [68]. The main control tab of the GUI, designed for routine operations, is visible in Figure 2.20. The user is prompted to press the correct button to proceed through the steps in the proper order. A visual check of the status of the critical components is possible in the CCTVs screen, shown in Figure 2.22. For instance, the CCTV dedicated to monitoring the loading phase is represented in Figure 2.21a.

Figure 2.23 shows in detail the mechanism related to the radionuclide collection part. There are three buffers (named *loading*, *central* and *unloading*) to host the tablets. A set of guides, two of which are movable (named *loading* and *unloading*), enables the tablets to pass from one buffer to the next one.

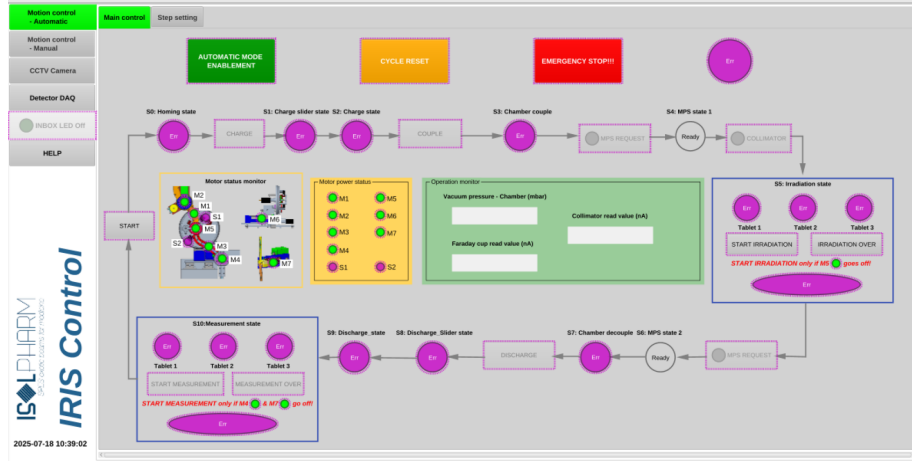
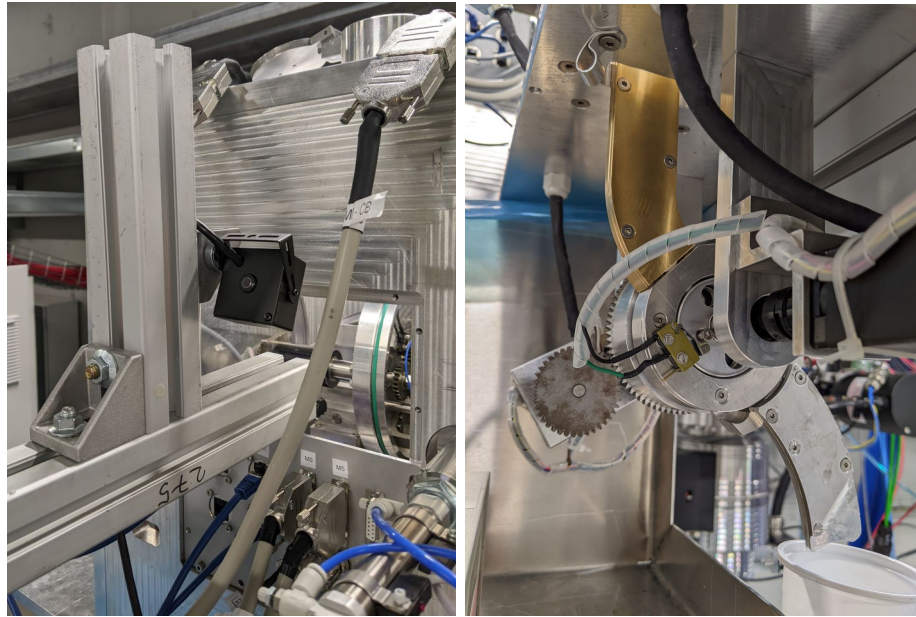


Figure 2.20: Screenshot of the main control tab of the IRIS Graphical User Interface (GUI).



(a) CCTV monitoring the loading (b) Prototype for offline tests of the loading phase.

Figure 2.21: Loading phase components and monitoring system.

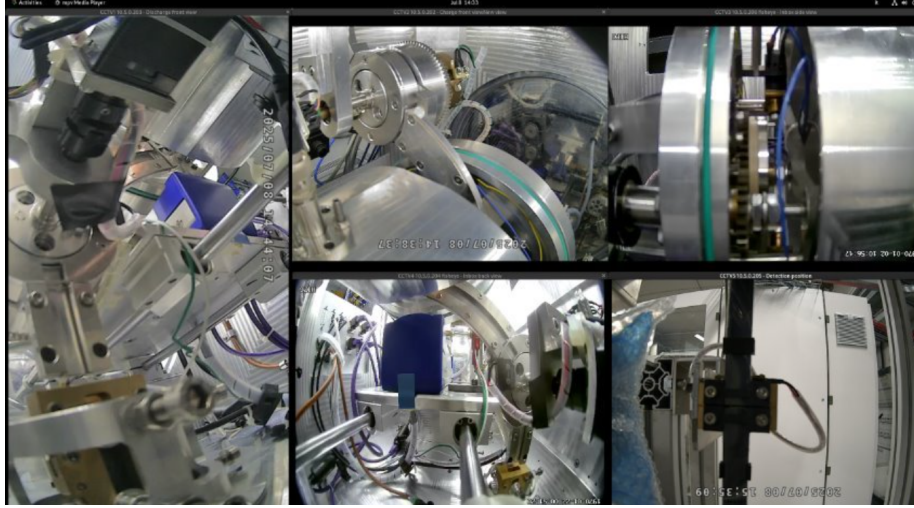


Figure 2.22: Screenshot of the CCTVs feeds. From the left window and continuing in a clockwise fashion, the critical points that can be observed are: the unloading funnel, the loading buffer and slide, the vacuum connection, the detection site, the unloading slide. From [90].

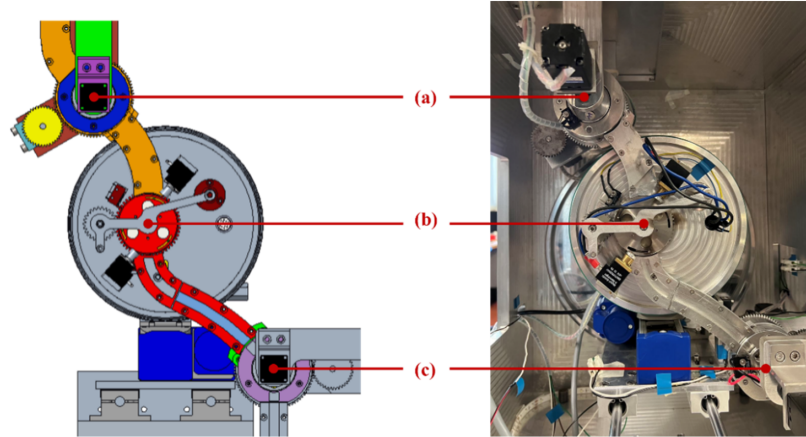


Figure 2.23: Front view of the IRIS motion system, consisting of (a) loading buffer and guide, (b) central irradiation buffer and (c) unloading buffer and guide. The loading and unloading guides are represented while ready to load and unload the central buffer respectively. From [83].

2.6 Conclusion

The production of ^{111}Ag at the SPES facility of INFN-LNL was investigated. The FLUKA code was used to predict the yield of the radionuclides produced in the proton-induced fission of the UC_x targets. In particular, the fission-driven production of ^{111}Ag was investigated. The production rate of Eq. (2.15) is affected by the efficiency related to the target release, ionisation, transport and collection steps. The ionisation efficiency can benefit from the use of the Resonant Ionisation Laser Ion Source technique. The resonant steps suitable for the ionisation of silver were identified in a series of experiments at the SPES offline laser laboratory.

For the radionuclide collection part, the IRIS system, comprising of mechanics, electronics and software, was installed in the ISOLPHARM beamline of the SPES low-energy experimental area. The IRIS implantation station (IS) is designed to be operated remotely and to minimise the dose received by an operator. The automatic workflow was commissioned offline ensuring a stable and reliable tablets handling.

The tests concerning the IS were carried out with tablets made of either sorbitol or hypromellose and with the following dimensions: diameter 13 mm and thickness in the [1.0,1.2] mm range (optimal value 1.1 mm). These materials were selected for their chemical properties, which make them suitable for subsequent dissolution in water and recovery of the implanted metal elements.

The Offline Detection System (ODS) comprises a germanium and an inorganic scintillator (LBC). The germanium features a full-energy peak absolute efficiency ranging from 0.2 % to 0.7 % for the energies of interest; in particular the main peak of ^{111}Ag at 342 keV can be detected with about 0.6 % efficiency.

To control the IS and the ODS, a custom software has been developed. This software is based on the EPICS architecture, the same architecture adopted throughout the SPES facility, ensuring seamless integration. For daily operations, an intuitive GUI has been developed, capable of preparing the system for collection and providing activity estimates.

In the future, the online commissioning of IRIS will be performed. The first tests will use stable beams to tune the system and maximise the collection efficiency. After this optimisation, the commissioning with Radioactive Ion Beams (RIBs) will be performed. IRIS weak points, that will emerge during real radionuclide collections at SPES, will be considered for the development of an upgraded version of the system.

Chapter 3

Detector Using MAPS for Beta-rays Observation (DUMBO) for ^{111}Ag

The content of this chapter is adapted from a work that is still in preparation to be submitted to a scientific journal.

3.1 Motivation

Developing a TRT candidate based on ^{111}Ag requires many tests both at the preclinical and clinical phases. The affinity and binding selectivity of a tracer-target pair can be assessed through in vitro autoradiography (ARG). In this imaging technique, the radiation source is within the sample itself. For comparison, in radiography, the sample is placed between the radiation source and the detector, Figure 3.1 illustrates this difference. Several autoradiography techniques have been developed, with spatial resolution from some micrometers to hundreds of micrometers. They are used with different types of samples (tissues, cells, etc.) for studying different phenomena.

The ISOLPHARM collaboration is developing a novel device for au-

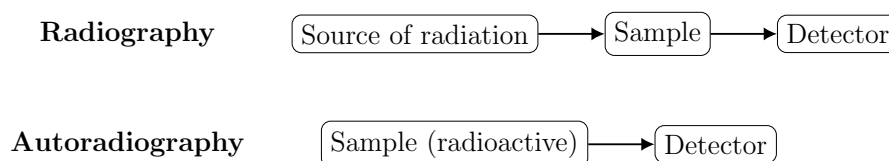


Figure 3.1: Scheme highlighting the differences between radiography and autoradiography.

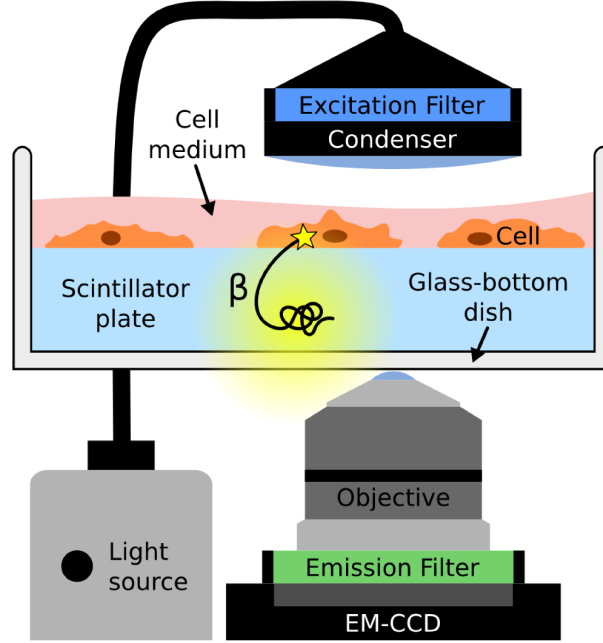


Figure 3.2: Radioluminescence microscope scheme. From [92].

toradiography, named Detector Using Maps for Beta-rays Observations (DUMBO). The development of this detector is the objective of one of the work packages of the ADMIRAL experiment, presented in the introduction. DUMBO was designed to be suitable for the energy range of the ^{111}Ag beta radiation [91].

State of the art of beta-imaging

Autoradiography of tissue slices provides higher spatial resolutions $< 0.2\text{ mm}$ than typical small animal in vivo scanners 2 mm [9, 93]. Emulsions and films can be used to get high spatial resolution but, on the other hand, they have low sensitivity and poor dynamic range. RadioLuminescence Microscopy (RLM) can be used to image cells without compromising the sensitivity or dynamic range of a digital sensor. In this method, an inverted microscope is used to image the dish in which the cell culture is placed on top of a scintillator plate with a thickness of $100\text{ }\mu\text{m}$. The radiotracer can be introduced into the cell culture. Following decay, the β -rays deposit their energy in the scintillator, producing optical photons. These optical photons are collected by a high-numerical-aperture objective and detected by a deep-cooled Electron-Multiplying Charge-Coupled Device (EM-CCD). Figure 3.2 shows the main elements of the RLM.

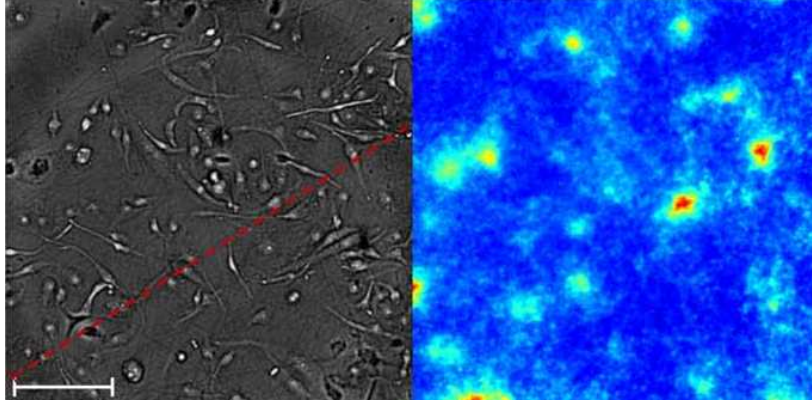


Figure 3.3: Brightfield (left) and radioluminescence (right) images of FDG uptake in single cells acquired with the RLM setup. The scalebar is 100 μm . From [92].

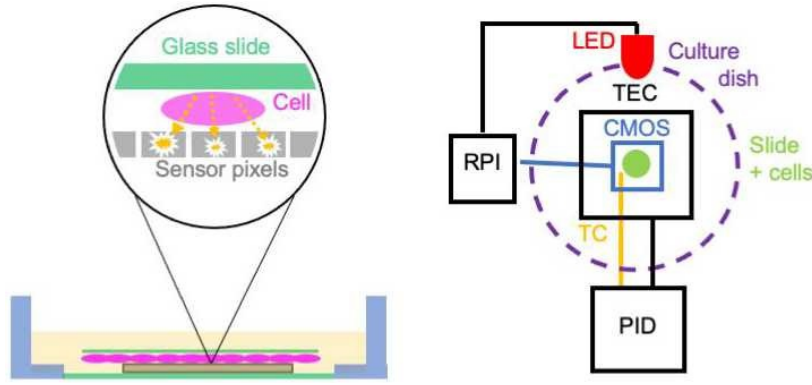


Figure 3.4: Lensless radiomicroscope scheme. From [25].

Radioluminescence, brightfield and fluorescence can be acquired with the same setup, enabling co-localisation [92]. Figure 3.3 shows an image acquired via RLM.

Imaging of beta-emitting radionuclides has been performed by a small number of laboratories using scintillator foils with RLM. Recently, a prototype employing a cost-effective Complementary Metal-Oxide-Semiconductor (CMOS) device was proposed; this detector, named the Lensless RadioMicroscope (LRM), was described in [25]. In this device, shown in Figure 3.4, the CMOS is used not as an optical-photon sensor but to detect the generated β rays directly. LRM can achieve a spatial resolution comparable to that typical of RLM. On the other hand, for LRM the cell culture must be deposited directly on top of the CMOS surface, to minimise the sample-detector distance. Consequently, the Field Of View (FOV) is limited to

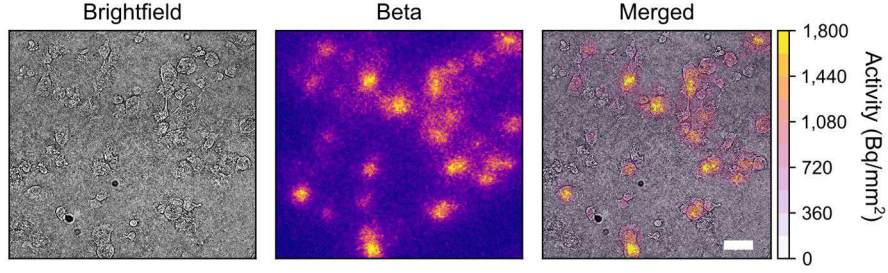


Figure 3.5: Brightfield (left) and beta (center) imaging of ^{18}F -FDG in breast cancer cells with the LRM setup. The two images can be overlapped for co-localisation (right). The scale bar is $50\text{ }\mu\text{m}$. From [25].

the sensor size, which is $3.79 \times 2.69\text{ mm}^2$ for the discussed prototype. The employed CMOS is the Raspberry Pi Camera Module v2.1 that mounts a Sony IMX219 8-megapixel sensor. The CMOS is read out through a Raspberry Pi computer. The sensor temperature is regulated using a Proportional-Integral-Derivative controller (PID) connected to a ThermoCouple (TC) and to a ThermoElectric Cooler (TEC). The LED can be used to produce the optical light needed for brightfield imaging. The entire system is enclosed in a light-tight box. LRM makes β - and α -imaging more accessible to the scientific community involved in *in vitro* radiopharmaceutical studies.

Figure 3.5 shows an image obtained with the LRM in a study of ^{18}F -FDG uptake by breast cancer cells. Notably, the single cells uptake can be distinguished.

DUMBO beta-imaging device

DUMBO is a beta-imaging device designed to provide non-invasive imaging of 3D cell cultures. The samples are placed in chambered coverslips where cell cultures can be grown in a 3D fashion. The cells position in scaffolds have varying height with respect to coverslip, posing a limit on the achievable spatial resolution. Having a layer of material between the sample and the detector, this device cannot achieve single-cell spatial resolution. On the other hand, DUMBO is easy-to-use and feature a large FOV. Therefore, it can be used as a complementary device to provide images on a different scale. In this work the development of this device and the first experiments aimed at its characterisation are presented.

Cell counting and foci assay are common experimental methods used in the preclinical studies of a radiopharmaceutical [94]. For these methods, the cell culture is typically grown on Petri dishes, which set a minimum

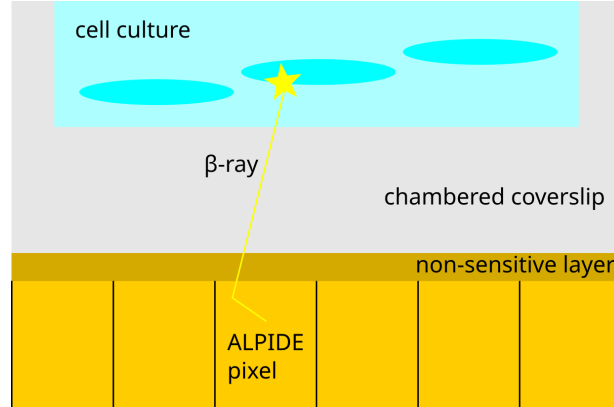


Figure 3.6: DUMBO acquisition scheme: cell cultures are grown inside a chambered coverslip; the radiotracer β -emission is detected by the ALPIDE sensor. The dimensions are not in scale.

limit on the sample-detector distance. Moreover, to image the whole dish area ($\sim 10\text{ cm}^2$), the imaging device must have a large FOV. DUMBO addresses these experimental needs thanks to its unusual sensor derived from high-energy physics: the ALice Pixel DEtector (ALPIDE).

3.2 Device technical description

ALPIDE chip

The core of the β detector developed by the ISOLPHARM collaboration is the ALice Pixel DEtector (ALPIDE), realised with Monolithic Active Pixel Sensors (MAPS), which are schematically represented in Figure 3.7. ALPIDE is made of 512×1024 pixels of $28\text{ }\mu\text{m} \times 28\text{ }\mu\text{m}$ area, for a total surface of about $1.5\text{ cm} \times 3\text{ cm}$ [96, 97]. Each pixel is read out using a binary scheme: hit or no hit. DUMBO readout chain consists of an Actel ProASIC Field Programmable Gate Array (FPGA) and a custom Printed Circuit Board (PCB). Dedicated firmware for the FPGA and user-level software were developed.

The ALPIDE chips have been developed to be used in the tracking system of the ALICE experiment at CERN-LHC [98]. Each chip has 512×1024 pixels realised with the Monolithic Active Pixel Sensor (MAPS) technology. Its high pixel density and low material budget make the ALPIDE a good candidate for medical application where achieving high spatial resolution is required [99, 100].

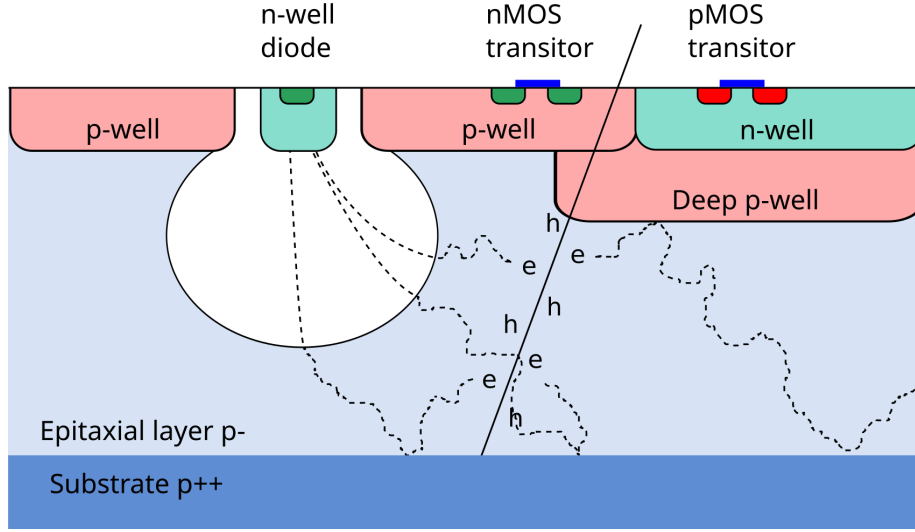


Figure 3.7: Schematic cross section of an ALPIDE pixel. Edited from [95].

The imaging potential of the ALPIDE chip was promptly recognised by the medical physics community. In fact, the chip has been used in the design of proton Computed Tomography (pCT) systems [101]. In particular, this chip is used in the tracking system for the pCT designed by the innovative Medical Protons Achromatic Calorimeter and Tracker (iMPACT) project [102]. This project was funded with a 1.8 M€ European Research Council (ERC) Consolidator Grant [103]. The ADMIRAL experiment joins this line of research by developing an ALPIDE-based detector for β -rays digital autoradiography.

It is interesting to compare DUMBO with the Lensless RadioMicroscope (LRM) presented in Section 3.1. The differences between these two imaging devices are summarised in Table 3.1. In particular, the simulations described in Section 3.3, indicate that DUMBO can reach a spatial resolution of about $200\text{ }\mu\text{m}$ while LRM has achieved $30\text{ }\mu\text{m}$ in real-case scenarios. The difference in the spatial resolution is mainly determined by the operational distance between the sample and the sensitive part of the detector. Since LRM works by placing the sample in direct contact with the chip surface, during multiple acquisitions the CMOS surface becomes contaminated and needs to be cleaned. DUMBO sensor is isolated from the radioactive sample to prevent contamination. The device was designed to host a chambered coverslip with $180\text{ }\mu\text{m}$ thickness. Additionally, $\sim 10\text{ }\mu\text{m}$ of electronics separate the coverslip from the sensitive elements of the ALPIDE. The difference in the FOV is mainly due to the difference in the sensors size. Moreover, DUMBO has a motorised mechanical frame that enables sample scanning, thereby virtually

	DUMBO	LRM
Minimum sample-detector distance	190 μm	0
Pixel size	28 μm	1.12 μm
Spatial resolution	200 μm	30 μm
Sensitive area (mm^2)	$(8 \times) 30 \times 15$	3.8×2.7

Table 3.1: Features comparison between the developed β -imaging device DUMBO and the Lensless RadioMicroscope (LRM).

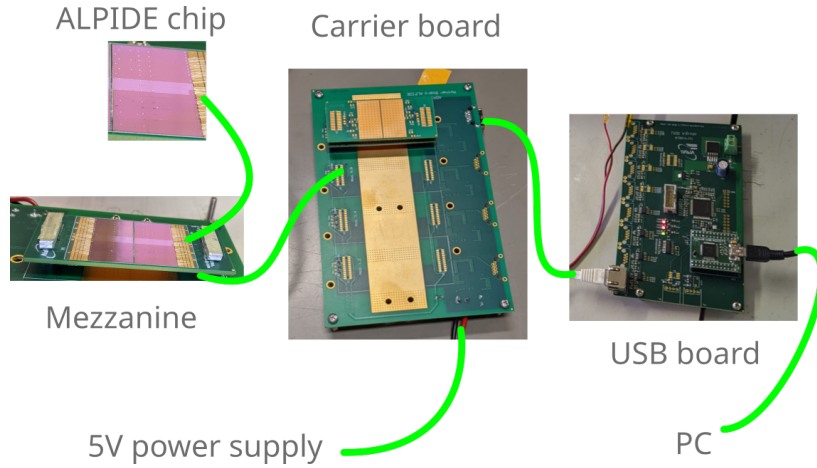


Figure 3.8: Scheme of the electronics implemented in DUMBO.

increasing the FOV.

DUMBO incorporates several ALice P π xel DEtectors (ALPIDE) chips to detect beta-rays emitted during the radioactive decay of radionuclides, such as ^{111}Ag . The current model features eight chips arranged in two rows and four columns, for a total sensitive area equal to $3 \times 12 \text{ cm}^2$. Instead, in the experiment described in Section 3.4, a smaller prototype with 2 chips ($3 \times 3 \text{ cm}^2$ sensitive area) was used.

DAQ

A desktop system featuring a single ALPIDE chip was already developed for testing purposes. This prototype featured a Field Programmable Gate Array (FPGA) Digilent Arty A7 and an Arduino shield [104]. To control this prototype, a custom python code was written. This code was modified to enable control of DUMBO. In fact, DUMBO features:

Address	Value	Description
0x0001	0x020A	continue readout at 20 MHz, no clustering
0x0004	0x0000	disable busy monitoring
0x0005	50000	strobe duration ($\simeq 1.25$ ms)
0x0006	5000	strobe gap ($\simeq 125$ μ s)
0x0010	0x0060	disable Manchester encoding
0x0602	0x0093	set reset voltage of the charge collecting node
0x060E	53	ITHR pixel charge threshold (about 0.5 nA)

Table 3.2: List of parameters and corresponding values chosen for the experiments. The description of the available parameters can be found in the ALPIDE manual [105].

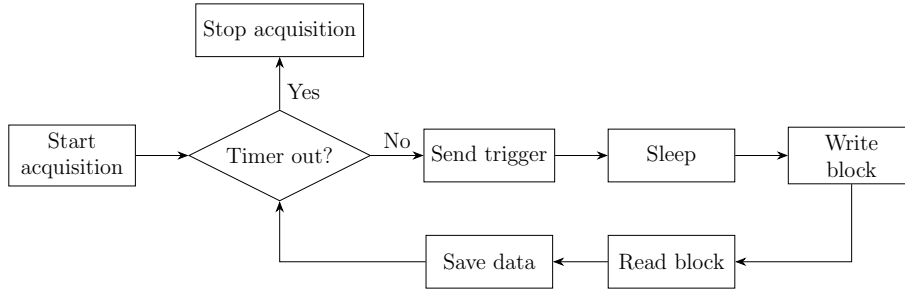


Figure 3.9: Scheme representing the workflow of the acquisition system.

- a custom electronic *carrier* board;
- four *mezzanine* boards that are plugged in the carrier board;
- two ALPIDE chips for each mezzanine;
- a *USB* board featuring a FT2232H Mini module and a small FPGA.

The carrier board has two banana connectors, which are used to supply the 5 V necessary to power the ALPIDE chips. During an acquisition, each ALPIDE chip typically absorbs 90 mA. In the experiment described in Section 3.4, the ALPIDE chips were powered by a RSPD 3303X-E bench power supply: output voltage from 0 to 32 V and output current up to 3.2 A. Each mezzanine has its own RJ45 socket mounted on the carrier; the corresponding sockets are hosted in the USB board; the connection is provided by Ethernet cables. A USB cable connects the USB board to a PC. A scheme showing the electrical connection is in Figure 3.8.

To control the ALPIDE chip, the differential control ports DCTRL_P e DCTRL_N [105] were employed. The same ports are used also to read

	horizontal (x-axis)	vertical (z-axis)
axis	ELGC-BS-KF-45-200-10P	ELGC-BS-KF-60-200-12P
adapter	EAMM-A-V32-42A	EAMM-A-V32-42A
motor	EMMT-ST-42-L-RMB	EMMT-ST-57-M-RM

Table 3.3: Description of the FESTO items used to move the sample.

the signal, with a maximum speed of 40 Mbps. Notably, a readout speed of 1200 Mbps could be achieved by using the dedicated ports. On the other hand, a specific electronics must be designed to sustain such speed. For the radionuclide activities considered in this context, the readout speed provided by the differential control ports is sufficient and does not constitute a limiting factor. A python code was developed to send the commands to the chip and to read the data. The communication with the USB board is managed by the `pySerial` module. After importing this module, the string containing the required messages were written [106]. The messages are used to manage the ALPIDE chip settings and to request the recorded data [105]. The values set for the parameters are reported in Table 3.2. A single data query is basically a four-characters string. To retrieve more than one single data from the chips, a string constituted by a chain (800) of single data queries is sent through the serial port. The chips accumulate the data during a programmed time delay (30 ms). Then, the pc reads the expected number of data bytes on the serial port and updates the hits list. Each hit consists of the coordinates of the triggered pixel. This cyclic readout continues until the acquisition time specified for the measurement elapses. This workflow is schematically represented in Figure 3.9.

Mechanical layout

To optimise the sensitive area of the ALPIDE chips and achieve the best available spatial resolution, a 3D movement between the sample and the ALPIDE chips is provided (see Figure 3.10). The core idea is to keep the ALPIDE chips stationary while the sample is moved around them. The detector mechanics were implemented using two ball screw axes with repetition accuracy of 15 μm . The list of components used is provided in Table 3.3. Each axis is coupled to a stepper motor with 1.8° steps and 5 % tolerance. The two motors automatically can move the sample in the xz-axes. To manually move the sample along the y-axis (the last of the three axes), a single-axis translation stage is mounted. The stage has a travel range of 6.5 mm actuated through a 10 μm graduated head. The motors

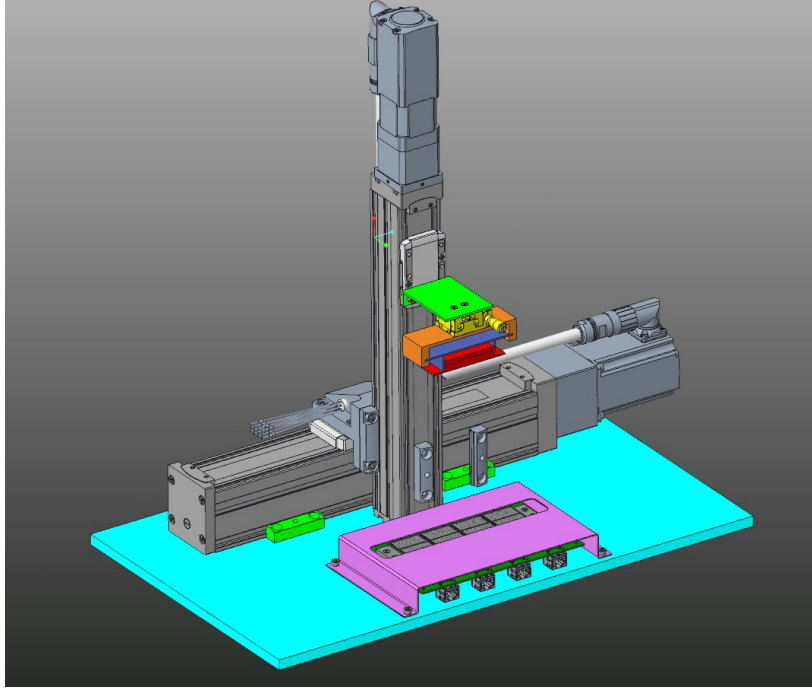


Figure 3.10: 3D model of DUMBO. The two motors used to provide the movement along the two axes are visible. The set of ALPIDE chips is fixed on an aluminium base.

are powered via the CMMT-ST-C8-1C-MP-S0 module. This module can be connected to a pc via Ethernet cable without the need for a PLC.

Software is available to move the motors; this is *Festo Automation Suite v2.9.1.1*. Several movement routines can be defined using the intuitive GUI of the software. The user can launch a single acquisition with default positioning, or acquire multiple images at different sample positions and later merge the data into a single image. A python library, named `festo-edcon`, is available and can be used to write python code to program the motors actions [107].

3.3 DUMBO digital twin

The Geant4 toolkit was used to build a Monte Carlo simulation framework to aid the planning and interpretation of the experimental results [40, 41, 42]. The simulation can be tuned according to the characteristics of the sample; the updated version is available online [108, 109]. Two different experimental conditions were addressed: cells in a Petri dish (2D geometry) and cells in

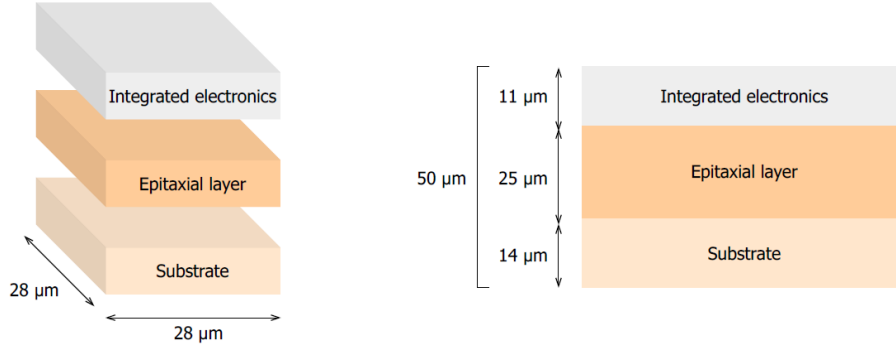


Figure 3.11: Structure of an ALPIDE pixel unit as simulated in Geant4. The diagram represents the three layers that compose one pixel. From [108].

a scaffold (3D geometry). In the 2D geometry, the Petri dish is built as a 35 mm diameter container with a $30\text{ }\mu\text{m}$ base made of Mylar. The cells are built as water spheres of $20\text{ }\mu\text{m}$ diameter dispersed in a water layer that has a thickness equal to $40\text{ }\mu\text{m}$. Each ALPIDE chip is a matrix with 512×1024 pixels with dimensions $28\text{ }\mu\text{m} \times 28\text{ }\mu\text{m}$ and a height of $50\text{ }\mu\text{m}$. Each pixel consists of: a $11\text{ }\mu\text{m}$ -thick layer made of silicon oxide (SiO_2) representing the integrated electronics; a $25\text{ }\mu\text{m}$ -thick silicon layer representing the epitaxial layer; and a $14\text{ }\mu\text{m}$ -thick silicon layer representing the substrate. Figure 3.11 shows a schematic of the described sensor structure. Only the epitaxial layers of each pixel are defined as sensitive volumes. In the 3D geometry, a hydrogel volume is built as a box made of 95 % water and 5 % GelMA (Gelatin Methacrylic Anhydride). Between the hydrogel and the detector, there is a $50\text{ }\mu\text{m}$ -thick layer of Mylar.

The primary particles are ^{111}Ag ions, generated at rest on the cells membrane. The probability distribution is uniform across the cell population and over the selected membrane. The physics lists adopted are: `G4EmStandardPhysics`, `G4DecayPhysics` and, for simulating ^{111}Ag and other radionuclides, `G4RadioactiveDecayPhysics`. Electronic neutrinos and antineutrinos are killed as soon as they are generated. The default range cut for secondary particles is used.

The output of the simulation is a ROOT file containing both histograms and tuples. The histograms contain pre-analysed data such as the hitmap and the energy spectrum. The tuples allow the user to study the correlation between hits of the same event. In particular, the clusters generated by single electron tracks are interesting since the DAQ system is able to recognise them and perform some case-specific operations, as described in section 3.2.

3.4 Experimental results

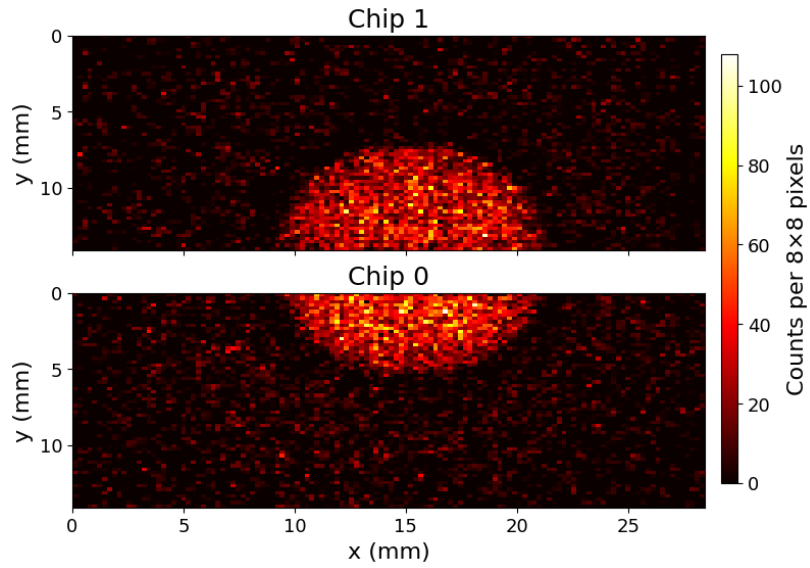
Experimental protocol

For the experiment described in this work, ^{111}Ag produced in the LENA laboratory of Pavia was used. The radionuclide was delivered in a water solution, that was inserted in three different types of containers: in plastic vials, in plastic phantoms and in GelMA phantoms [110]. The plastic vials had a diameter of 6 mm and 12 mm. The liquid gelatin was inserted in a chambered coverslip with a polymeric bottom [111]. The gelatin was cured using a UV lamp with 405 nm emission and 6 W power. The ^{111}Ag samples activity was measured using a germanium gamma-ray detector. Since the radioactive samples prepared for this experiment have heterogeneous shapes, a 10 % uncertainty for the activity estimations was considered. The plastic phantoms were made of Polyoxymethylene (POM) and their dimensions were chosen to closely match those of the GelMA phantoms.

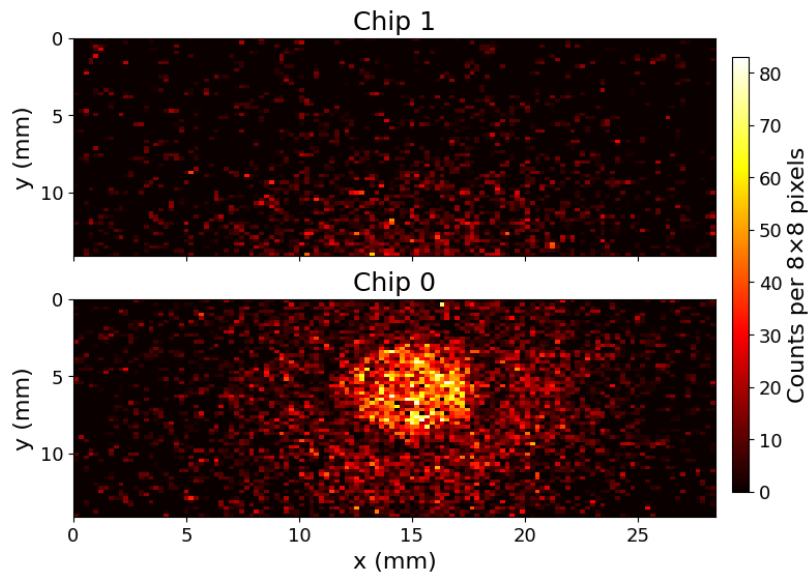
Images with vials and plastic phantoms

An experimental session was carried out to evaluate the performance of this device with the radionuclide of interest, ^{111}Ag . The radionuclide was produced at the LENA laboratory in Pavia and was available in aqueous solution. Several images were collected using samples with different amounts of activity and different shapes. The stock solution contained 7.92 MBq of ^{111}Ag in 1 mL of water. The stock solution inside a vial with 12 mm diameter was the first image acquired. The detector spatial resolution is sufficient to recognise the circular shape of the sample (Figure 3.12a). The space in between the two subplots represents the space that separates the sensitive areas of the two ALPIDE chips. This space is not to scale, so it does not represent the width of the non-sensitive area in vertical-axis unit. Also for the small vial containing 10 μL of the stock solution (79 kBq of ^{111}Ag), the circular shape can be recognised (Figure 3.12b). In both images, the darker corona around the central area corresponds to the plastic walls of the vials, which attenuate electrons more efficiently than the surrounding air.

Another set of acquisition was performed using plastic (POM) phantoms. Multiple phantoms were prepared for this experiment; for the sake of conciseness, only one is discussed in this thesis. The phantom is a $25 \times 65 \times 7 \text{ mm}^3$ POM brick, containing two pockets that host the radioactive solution. The pockets are 15 mm long and have different widths: 2 mm and 3 mm. A circular notch with a 3 mm diameter facilitates the insertion of

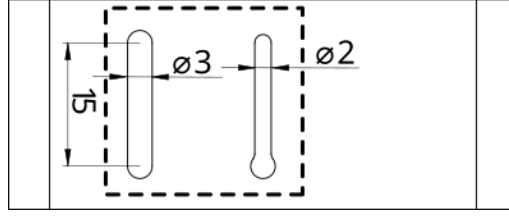


(a) 12-mm-diameter vial.

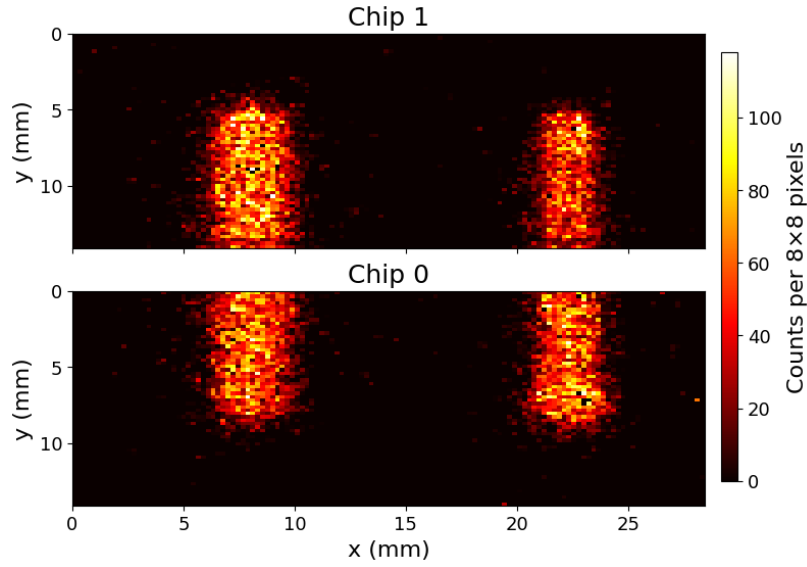


(b) 6-mm-diameter vial.

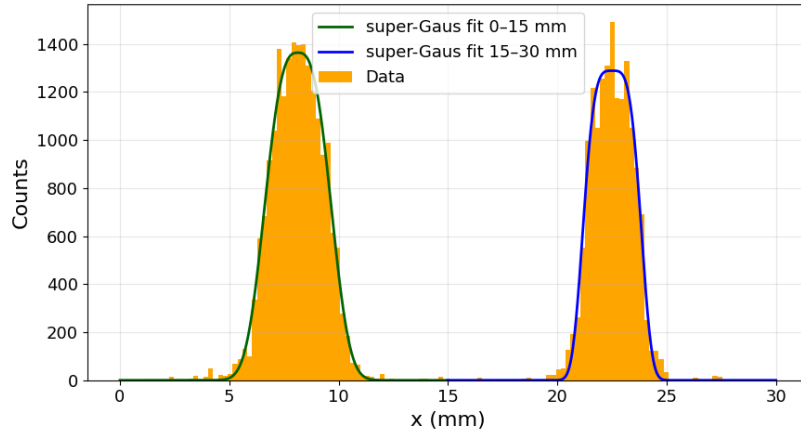
Figure 3.12: Image of vials containing ^{111}Ag solution. The hit maps have a 8×8 binning.



(a) Technical drawing of the phantom, with distances in millimeters. The dashed line indicates the phantom area within the FOV of the imaging device.



(b) Hitmap of the phantom. Binning 8×8 is used.



(c) Profile along the x-axis of chip 0, considering the lines with y in $[0.0, 5.0]$ mm.

Figure 3.13: Plastic phantom acquisition with ^{111}Ag solution.

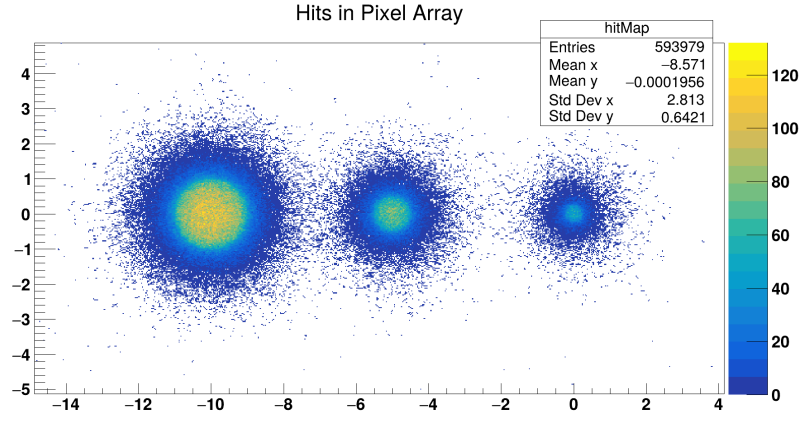
the solution using a micropipette. The bottom of each pocket is 0.2 mm thick. Figure 3.13b shows the image of the pockets acquired by DUMBO. The corresponding FOV is indicated with a dashed contour on the technical drawing in Figure 3.13a. An additional 1 mm-wide pocket was intended to be imaged, but it could not be filled with the radioactive solution due to leakage. The profile along the x-axis of the bins within [0.0, 5.0] mm of chip 0 is drawn in Figure 3.13c. The distribution of each pocket is fitted with a super-Gaussian function to better describe the flattop. The FWHMs are estimated from the standard deviation and they are equal to 3.15(4) mm and 2.65(4) mm, for the 3 mm and 2 mm pockets, respectively. The increase in FWHM relative to the source width is larger for the smaller source. This difference is likely due to the range of the emitted electrons in POM, which becomes more significant as the source size decreases. In the Continuous Slowing Down Approximation (CSDA), the range of 360 keV electrons, the average energy value for Ag-111, is about 0.8 mm [112].

Images with GelMA phantoms

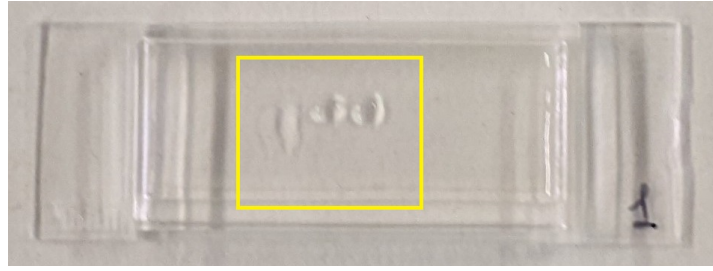
GelMA phantoms were produced to test an acquisition in conditions closer to those of interest. The ^{111}Ag is inserted in three wells prepared inside the phantom, highlighted by the yellow contour in Figure 3.14b. The sample is imaged by DUMBO, and the resulting image is shown in Figure 3.14c. The plan was to create three ^{111}Ag spots with different diameters: 0.5 mm, 1 mm, 2 mm. The expected result was calculated through a Geant4 simulation and featured three circular clusters with diameters close to those of the corresponding sources (Figure 3.14a). Instead, the drops of radioactive solution leaked out of the prepared well, and contaminated the surrounding area. In fact, the ^{111}Ag spots all appear to have the same dimensions. Moreover, the first spot on the left shows a more pronounced leakage of solution which can even be observed in picture of the phantom, in Figure 3.14b.

3.5 Discussion

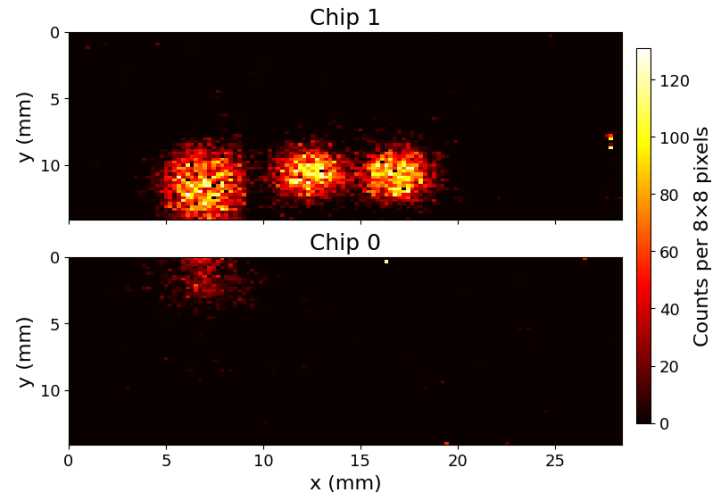
In general, including for DUMBO, β -imaging strongly depends on the sample-detector distance and on the sample shape. Therefore, sample preparation is a crucial step in optimising the detector response. The GelMA phantoms could not be realised with the desired geometry, as the ^{111}Ag solution easily leaked out of the prepared wells. The micropipette with 10 μL precision is



(a) Geant4 simulation of the 0.5 mm, 1 mm and 2 mm diameter wells with ^{111}Ag in GelMA. From [113].



(b) Picture of the GelMA phantom. The three ^{111}Ag spots inside the yellow square are imaged.



(c) Hitmap of the GelMA phantom.

Figure 3.14: GelMA phantom acquisition with ^{111}Ag solution.

not suitable for filling this wells, an alternative strategy needs to be designed for future experiments.

The ability to obtain quantitative information is limited by the slow speed of the acquisition routine. The detector count rate is dead-time limited at activities as low as 100 kBq. Consequently, no proportionality between the sample activity and the recorded counts could be established with the current system.

3.6 Conclusion

A novel device for beta-imaging named Detector Using MAPS for Beta-rays Observation (DUMBO) is presented in this chapter. The core of this device is the ALice Pixel DETector (ALPIDE), derived from the High Energy Physics experiment ALICE at CERN. DUMBO is designed to host several ALPIDE chips, each one is made of 1024×512 pixels, providing a sensitive area of $30 \times 15 \text{ mm}^2$. A dedicated front-end electronics was developed to control these chips and to acquire the detected signals.

To increase the sensitive area of the device, a motorised frame is installed to move the sample with respect to the ALPIDE chips. The motors can be controlled through a python script. Since the DAQ script is written in the same programming language, the motors control and detector acquisition parts can be integrated into a single program.

DUMBO design is suitable for the beta-decay properties of ^{111}Ag ; the first experiment with this radionuclide and with the complete DUMBO system is presented. Images of ^{111}Ag samples were obtained with DUMBO: including both vials and phantoms with well-defined geometries. The device spatial resolution predicted by the Geant4 simulations ($200 \mu\text{m}$) could not be verified. In fact, the phantoms fabricated for this experiment were not small enough to assess spatial resolutions below 1 mm.

Upgrades are needed on both the mechanics and electronics sides. In particular, the issue regarding the fragile bond could benefit of the implementation of MAPS foil with no exposed bonds [114]. Flipping the chip would allow to protect the integrated circuit from accidental damage without the need of an additional layer of material. Increasing the maximum acquisition rate of the DAQ is important to reduce the acquisition time and to recover the proportionality between the number of counts and the sample activity. In the future, tests will be performed to prove whether local activity quantification can be obtained.

Chapter 4

Gamma camera for ^{111}Ag

4.1 Motivation

Single Photon Emission Computed Tomography (SPECT) is an imaging technique commonly used in clinical diagnosis. It allows physicians to assess the functionality of a specific tissue and its perfusion. SPECT produces a 3D image representing the distribution of a radiotracer injected in the patient body [116]. The gamma camera is the workhorse imaging device for SPECT [117]. Invented by Anger in the late 1950s, its underlying concept remains relevant in modern imaging. SPECT equipment is being upgraded with new scintillation crystals and collimator designs to increase sensitivity and spatial resolution [118]. Figure 4.1 schematically illustrates the imaging procedure with a gamma camera.

Imaging of ^{111}Ag through its gamma-ray radiation has already been proved in preclinical experiments with rabbits [39]. This chapter describes the development of a gamma camera tailored to the ^{111}Ag radiation. Ma-

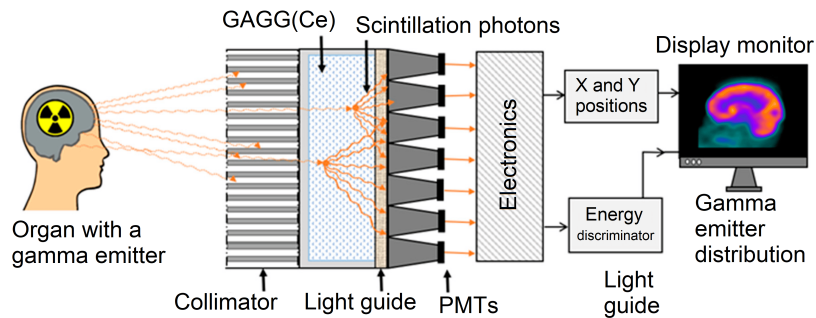


Figure 4.1: Scheme representing the basic components of an Anger scintillation camera and the imaging workflow. Adapted from [115].

materials from two reports are incorporated in this chapter: one is a proceeding on the Geant4 simulation of the device, submitted for the conference ICFDT7 [119]; the other describes the first measurements for the device characterisation, which will be submitted soon [120]. This work focuses exclusively on the features of a single, stationary gamma camera. Multiple projections and image-reconstruction algorithms were not investigated.

4.2 Device technical description

The developed gamma camera follows the typical structure of common models, such as the one shown in Figure 4.1. Namely, it consists of the following components:

- a collimator, that collimates the gamma-rays emitted by the radioactive source;
- a scintillator, in which the collimated gamma-rays are absorbed with the consequent emission of scintillation optical photons;
- a photon detector, that collects the produced optical photons.

In this section, the listed items will be described more in detail.

The collimator is a prototype made of tungsten with parallel and squared holes. The septa are 1 mm thick and the holes are 2 mm large (3 mm total pitch), while their length is 30 mm. The fabrication began with a tungsten foil of thickness corresponding to that desired for the septa; the foil was cut via Electrical Discharge Machining (EDM) with a comb-shaped pattern. The combs are stacked together in such a way to create a square geometry, and are finally enclosed in a metal case.

Two different commercial scintillators have been tested, both of them are arrays of Gadolinium Aluminium Gallium Garnet (GAGG) doped with Cerium. Both scintillators are not a single-block of material but assemblies of tightly packed rods, with a $1\text{ mm} \times 1\text{ mm}$ square cross-section. The first scintillator used had rods 26 mm long and was discarded due to insufficient light transmission to the photon detector. The second scintillator consists of a 23×23 array of rods, each 17 mm long. The rods are separated by 0.2 mm of BaSO_4 , a reflective material, to channel the optical photons. A 0.03 mm aluminium foil covers the lateral and bottom sides of the array. The total dimensions are $27.86 \times 27.86 \times 17.23\text{ mm}^3$.

The photon detector is a Hamamatsu S14160-3050HS-08 Silicon Photo-Multiplier (SiPM) with 64 different channels arranged in a 8×8 layout [121]. Each channel consists of 3584 pixels, each $50\text{ }\mu\text{m}$ in size, resulting in a

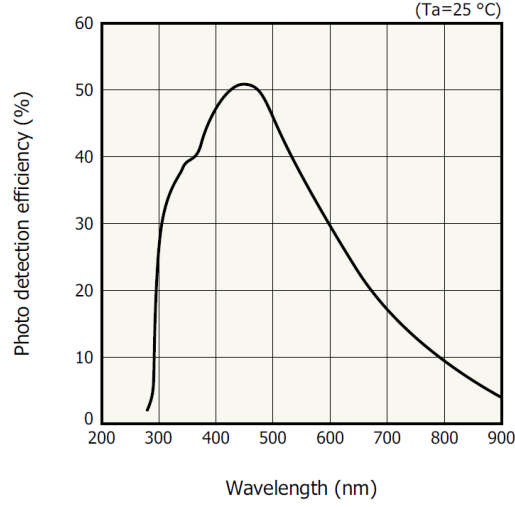


Figure 4.2: S14160-3050HS-08 quantum efficiency spectrum. From [121].

sensitive area of $3.0 \times 3.0 \text{ mm}^2$ per channel. The channels geometrical fill factor is 74 %, and they are separated by 0.2 mm of silicone resin. The total dimension of the SiPM results $25.8 \times 25.8 \times 1.35 \text{ mm}^3$. The window in front of the pixels has a refractive index of 1.57. The photon detection efficiency exceeds 10 % between 300 and 800 nm, reaching a maximum of approximately 50 % at 450 nm; the full spectrum is shown in Figure 4.2. The measurements were carried out at room temperature, using a SiPM bias voltage of 42 V.

A CAEN FERS-5200 unit is used for the readout, namely the A5202, which hosts two Citiroc-1A chips, for a total of 64 readout channels. Each channel includes a preamplifier, a fast shaper followed by a discriminator and a slow shaper with peak-sensing detector. To control and read out this board, the open source software Janus was used.

4.3 Prediction with Monte Carlo simulations

Description of the simulation

This section describes the development of the gamma camera digital twin, aimed at evaluating sensitivity and spatial resolution by varying key device parameters. The Monte Carlo simulation was realised using the well-known Geant4 toolkit for particle tracking in matter, widely used in medical

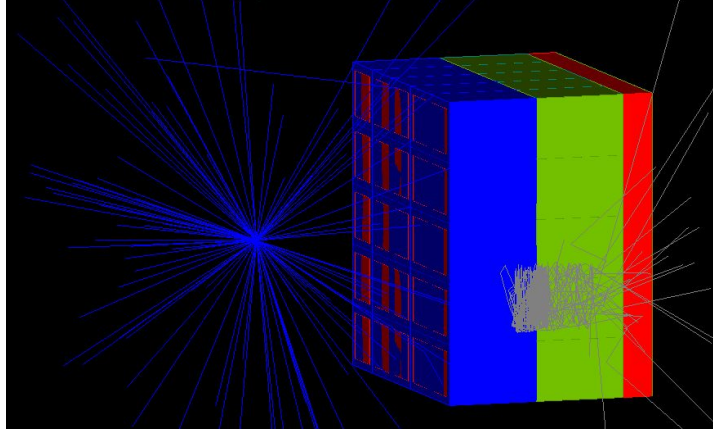


Figure 4.3: Graphical representation of the simulated gamma camera. Blue tracks indicate gamma-rays and gray tracks indicate scintillation photons.

applications [40, 41, 42]. The simulation includes all components of the gamma camera except the readout electronics [122].

The collimator is created by replicating a squared bore along the x and y axes in a tungsten block, assuming a coordinate system where the SiPM detector plane is parallel to the xy-plane and the collimator holes axes are aligned with the z-axis. Similarly, the scintillator is realised by replicating along the x and y axes a GAGG rod surrounded by an optical reflective wall. Single SiPM pixels within each channel are not modelled; the required data are obtained by counting the optical photons hitting each of the 64 sensitive volumes. The resulting geometry is shown in the Figure 4.3. The collimator, scintillator, optical coupler and SiPM are modelled using the parameters indicated in Section 4.2.

The physics library used to simulate the electromagnetic interactions is `G4EmStandard Physics_option3`. The `G4OpticalPhysics` library was called to simulate the scintillation processes occurring in the GAGG(Ce) crystals. For this purpose, the optical parameters describing the simulated GAGG(Ce) material are: scintillation yield of 54×10^3 optical photons per MeV, refractive index of 1.9 and absorption length of 645 mm [123]. For the radionuclides decay `G4RadioactiveDecayPhysics` and `G4DecayPhysics` are used.

Additional properties are assigned to the materials to define the behaviour of optical photons at the interfaces between volumes. The more modern `unified` model is used to prepare the simulation for potential upgrades. On the other hand, considering the options currently used, the same result would be obtained by adopting the `glisur` model. The interface type between each

GAGG rod and the surrounding reflector layer is set as `dielectric_metal`, ensuring that scintillation photons are reflected back. The GAGG-reflector interface finish is `polished`, making it a specular reflector. A more realistic diffuse reflecting surface was also tested, but it produced no significant difference in the simulation results, only an increase in computational time. Therefore, the inner surfaces of the GAGG rods were assigned mirror-like reflective properties. Geant4 enables to adjust the percentages of photons that are reflected and of those that are absorbed. Absorption at the reflector surface reduces the number of optical photons reaching the SiPM. Since the magnitude of this reduction is a stochastic process, the energy resolution worsens as surface absorption increases. After testing different values, the surface was modelled with 6% absorption. At this value the simulated energy spectra closely match those measured experimentally with ^{111}Ag . In particular, as shown in the next sections, the FWHM of the full-energy peak for a 342 keV gamma-ray is in close agreement with the experimental value. The optical interface at the bottom of each rod, where it contacts the optical coupler, uses the default settings (`dielectric_dielectric` type with `polished` finish and no absorption). With this configuration, each photon reaching the rod-coupler interface is propagated according to Snell's law, using the refractive indexes n_1 and n_2 of the two materials.

$$n_1 \sin \theta_1 = n_2 \sin \theta_2 \quad (4.1)$$

where θ_1 and θ_2 are the angle of incidence and refraction of the light ray with respect to the normal of the interface. The optical interface from the coupler to the SiPM is a fully transmitting one: all the optical photons continue along their trajectory regardless of the refraction indexes. Complete transmission was adopted for this interface because the default optical model resulted in an optical photon collection significantly lower than observed experimentally. Each of the 64 SiPM channels could be represented as a matrix of 3531 pixels with a 50 μm pitch, but this level of detail was considered unnecessary.

Image reconstruction procedure

The output files of the simulation are processed using the ROOT analysis software or the `uproot` Python package, coherently with the output data format [43]. The output file provides both simulated data unavailable in real experiments (primary energy and position, scintillator energy deposition, photon distribution) and measurable quantities (channel counts and coincidences). The images were reconstructed using the Center Of Gravity

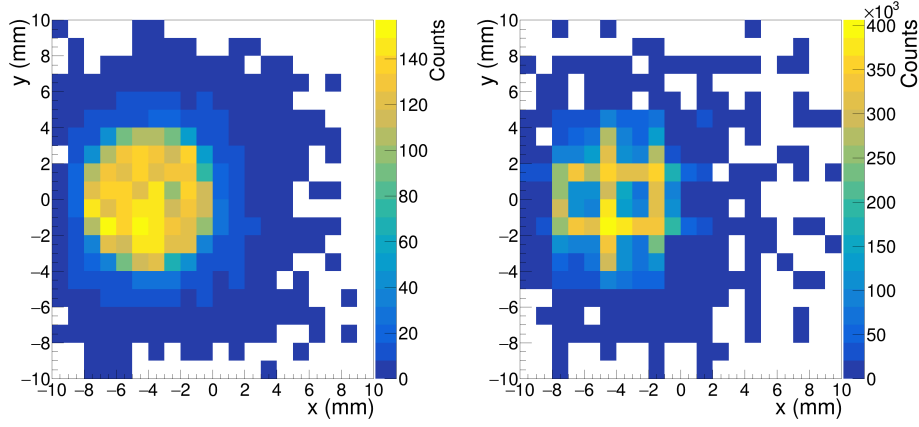


Figure 4.4: Simulation of a collimated beam of 342 keV gamma-rays impinging directly on the scintillator. On the left, the simulated deposited energy in the scintillator is shown; on the right, the image reconstructed from the SiPM signals with the center of gravity algorithm is shown.

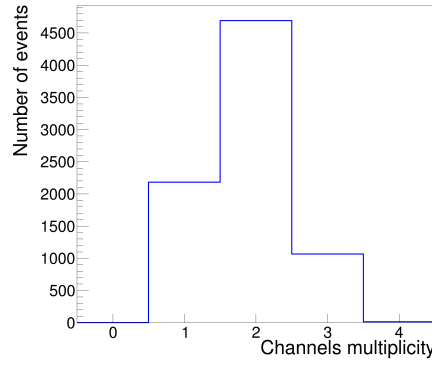


Figure 4.5: Triggered channels per event with a 342 keV gamma-rays source.

(COG) algorithm: the position of a single event is calculated as the average position of the triggered channels x_i weighed with the correspondent number of counts N_{Pi} [124]:

$$x_{\text{COG}} = \frac{\sum_{i=1}^{64} x_i N_{Pi}}{\sum_{i=1}^{64} N_{Pi}} \quad (4.2)$$

Figure 4.4 compares the image reconstructed using this algorithm with the image derived from the scintillator local energy deposition, which is available only in simulation. The source is a beam of 342 keV gamma-rays directed along the z-axis, with circular cross section of 8 mm diameter. No collimator was used, as this comparison focuses on the information loss of the photon detector regarding the source position. The COG counts are distributed

preferentially at the channels centers and along the lines that link them. This distribution suggests that only few channels are triggered in each event. Figure 4.5 confirms this observation: the maximum occurs for two-bins counts, and there are virtually no events above three-bins. The application of a smoothing filter could help the visualisation.

Comparison with analytical predictions

The gamma camera performance is determined mainly by the collimator, scintillator and SiPM. According to the literature on this topic, spatial resolution can be defined as FWHM of the single-pixel response for a line source [125]. It can be analytically computed as:

$$R = D \frac{z'_{\text{eff}}}{L_{\text{eff}}} \quad \text{with} \quad z'_{\text{eff}} = z_{\text{eff}} + L_{\text{eff}}, \quad L_{\text{eff}} = L - 2/\mu, \quad z_{\text{eff}} = z + 1/\mu \quad (4.3)$$

In this equation L is the length of the holes, D is the side of the square holes, z is the source-collimator distance and z' is the source-detector distance. The *eff* subscript indicates the corresponding *effective* quantity, corrected for the gamma-ray attenuation length $1/\mu$ in the material. This equation is only valid when the line source is parallel to the square holes sides.

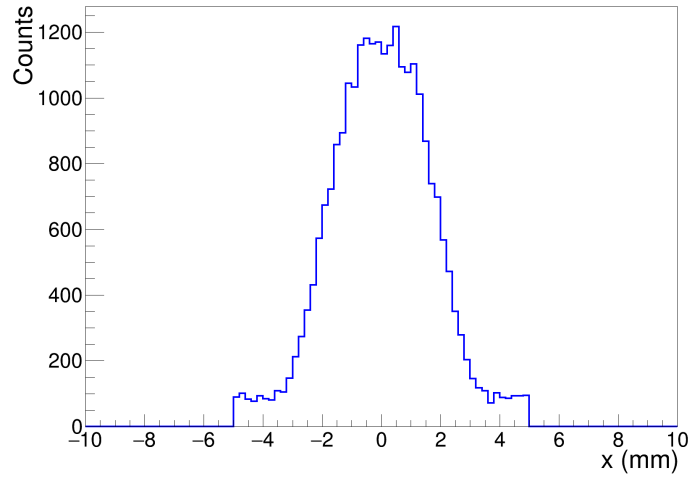


Figure 4.6: Distribution of ^{111}Ag main gamma-rays (energy 342 keV) generated in a line along the x-axis (with $x \in [-5, 5]$ mm, $y = 0$ mm, $z = 30$ mm) that are detected within the central hole of the collimator.

The total attenuation coefficient is calculated by the NIST tool XCOM, assuming a gamma-ray energy of 342 keV and tungsten material [126]. The

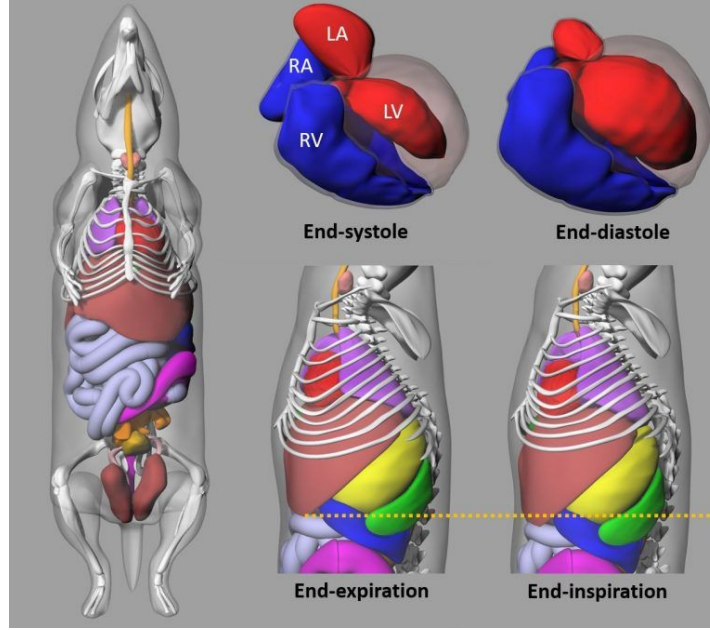


Figure 4.7: Representation of the 4-D MOBY phantom with models for heart and respiratory motions. From [127].

tool predicts $\mu/\rho = 0.253 \text{ cm}^2 \text{ g}^{-1}$ and an attenuation length equal to 2.1 mm. Using these values and those of the collimator designed for the gamma camera, the estimated spatial resolution for a line source positioned 30 mm from the collimator surface is $R = 4.48 \text{ mm}$. This analytical estimation can be compared with the results from the developed Monte Carlo simulation. Consistent with the boundary conditions described in the reference work [125], 1×10^9 events were simulated with a line distribution along the x-axis and placed 30 mm from the collimator surface. The graph in Figure 4.6 shows the single-pixel response function, obtained from the distribution of events detected within the central collimator hole. Subtracting the lateral baselines, the simulated FWHM can be estimated, resulting in 4.0(2) mm. The simulated FWHM is smaller than analytically calculated value. Differences were expected, as the formulas used in this field simplify the treatment of effects such as material attenuation and scattering.

MOBY phantom simulation

An important requirement for medical imaging simulations is to accurately model the subject anatomy. Phantoms were used to assess the gamma-camera suitability for preclinical experiments. The MOBY software was

used to generate attenuation and activity maps of a standard mouse, suitable for biodistribution experiments [128]. The mouse phantom anatomy was built from high resolution 3-D magnetic resonance microscopy data [129]. The user can change several parameters to shape the phantom according to the desired features. The mouse generated for this study had a scaling parameter of 0.78 along the x, y and z axes. No lesion was considered, and the activity inside the body was distributed uniformly. Only a single time frame was calculated, neglecting both cardiac and respiratory motions. A text file with the phantom voxels structure is imported within the Geant4 volume construction. The voxels are built using the `G4PhantomParameterisation` class, based on the imported data. In the user-defined primary generator class, the ROOT file containing the description of the radioactivity distribution in the mouse can be imported. In this way, the user can generate primaries (primary particles) within specific organs of the mouse.

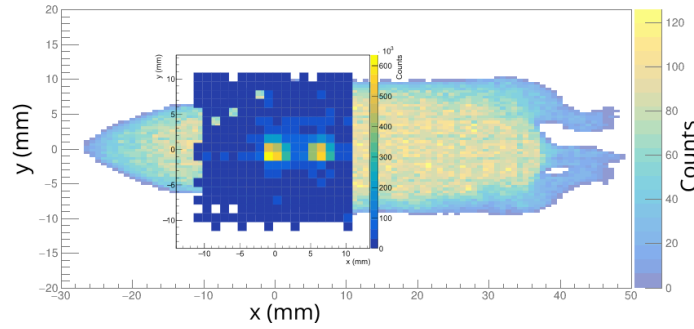


Figure 4.8: Simulated image with two tumours 5 mm apart inside a mouse model. The mouse shape in the background serves only to indicate the MOBY mouse geometry.

The MOBY phantom previously described was employed to simulate images of a tumours-bearing mouse. The tumours are simulated generating ^{111}Ag nuclei in a sphere of 1 mm diameter. Several simulations were run, changing the sphere x position while keeping constant the y and z positions. The sphere was positioned 10 mm distance from the collimator surface. The case with multiple tumours in a single mouse can be obtained by summing the output of each single-tumour acquisition. In the same fashion, a radioactive background from specific organs or the entire body can be added. Figure 4.8 shows the image obtained by simulating two tumours separated by 5 mm; additionally, a uniform ^{111}Ag background was generated throughout the mouse body. The same number of events, 1×10^8 , are generated in each tumour and in the background. In biodistribution experiments with mice, injected activities are typically close to 2 MBq. Considering such activity

for the ^{111}Ag source, the number of recorded events in Figure 4.8 would be collected with a 150 s-long acquisition.

4.4 Measurements with ^{111}Ag

^{111}Ag sample preparation

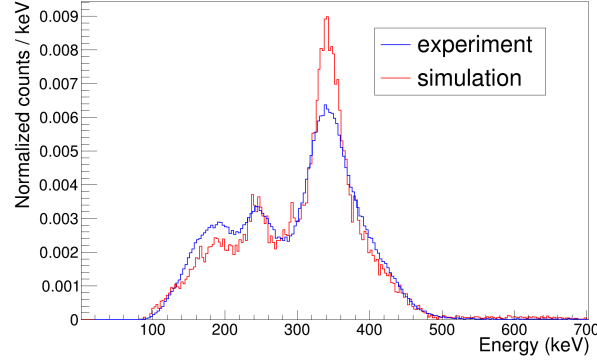
In May 2025 an experiment devoted to the gamma camera characterisation with ^{111}Ag was performed at the LENA facility in Pavia. Using the protocol described in Section 2, about 20 MBq of ^{111}Ag were produced for this experiment. The radioactive solution was inserted in three different types of container:

- small vial with inner diameter 8 mm
- big vial with inner diameter 13 mm
- mouse phantom

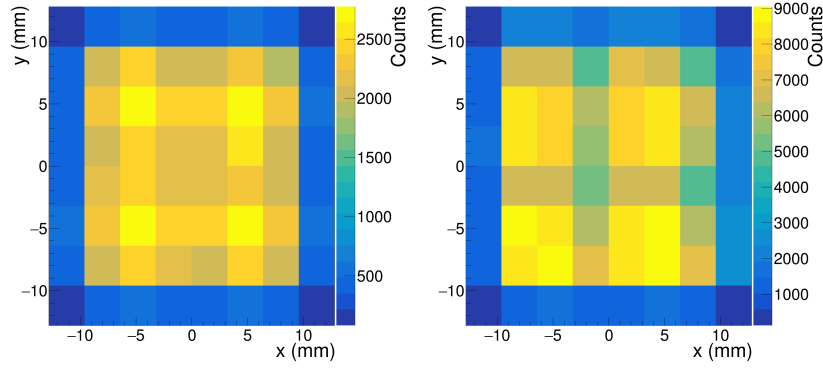
The mouse phantom is realised according to the Digimouse, a 3D whole body mouse atlas that was obtained from CT and cryosection data [130]. This atlas is made of a $380 \times 992 \times 208$ matrix, with 0.1 mm cubical voxels, from a 28 g nude normal male mouse. The phantom is made of a transparent material and consists of two parts: a bottom part resembling a multi-well plate and a top part serving as lead. Each well identifies a single organ or solid tumour.

Characterisation with vials

Figure 4.9 shows the energy spectrum and the hitmap for the acquisition with the stock solution of ^{111}Ag , positioned 20 cm from the scintillator surface, with no collimator. Both the experimental results and the simulated ones are shown. In the energy spectra, the 342 keV and 245 keV peaks can be distinguished. The 245 keV full-energy peak is almost overwhelmed by the background, while the 342 keV peak is above the noise. The energy spectra are calibrated using the two peaks at 245 keV and 342 keV and assuming a linear proportionality with no offset: $E[\text{keV}] = mE[\text{au}]$. The hitmaps are generated using a clustering algorithm: for each event, the COG is calculated considering only the pixel with the highest intensity and its 8 neighbouring pixels. The periphery of the hitmaps shows fewer counts, because the outer SiPM channels are not used for triggering. Adopting this triggering mask reduces noise in the acquisitions. Conversely, a uniform field



(a) Simulated and experimental total charge.



(b) Simulated 2D image.

(c) Experimental 2D image.

Figure 4.9: Acquisition of the large vial with 18.35 MBq of ^{111}Ag placed at about 20 cm along the central axis of the scintillator, without the collimator. The figure at the top shows the total energy distribution recorded by the SiPM. The two figures at the bottom show the 2D image reconstructed from the SiPM signal; left is the simulation and right is the experiment.

was expected from the acquisition; the visible patterns are likely artifacts resulting from the binning choice.

To estimate the spatial resolution of this system, an image with the ^{111}Ag inside a small vial was acquired. In this case, the spatial resolution is calculated as the FWHM of the peak in the image. Figure 4.10 shows the acquisition of the small vial placed at the center of the collimator surface. The activity of the small vial was 7.36 MBq at the start of the acquisition. The profiles of the central bin, for the experimental and the simulated images, are shown in Figure 4.10c. From the standard deviation of the Gaussian fit, the FWHM can be calculated as 2.355σ , obtaining 6.8 mm and 7.7 mm for the experimental and simulated images respectively.

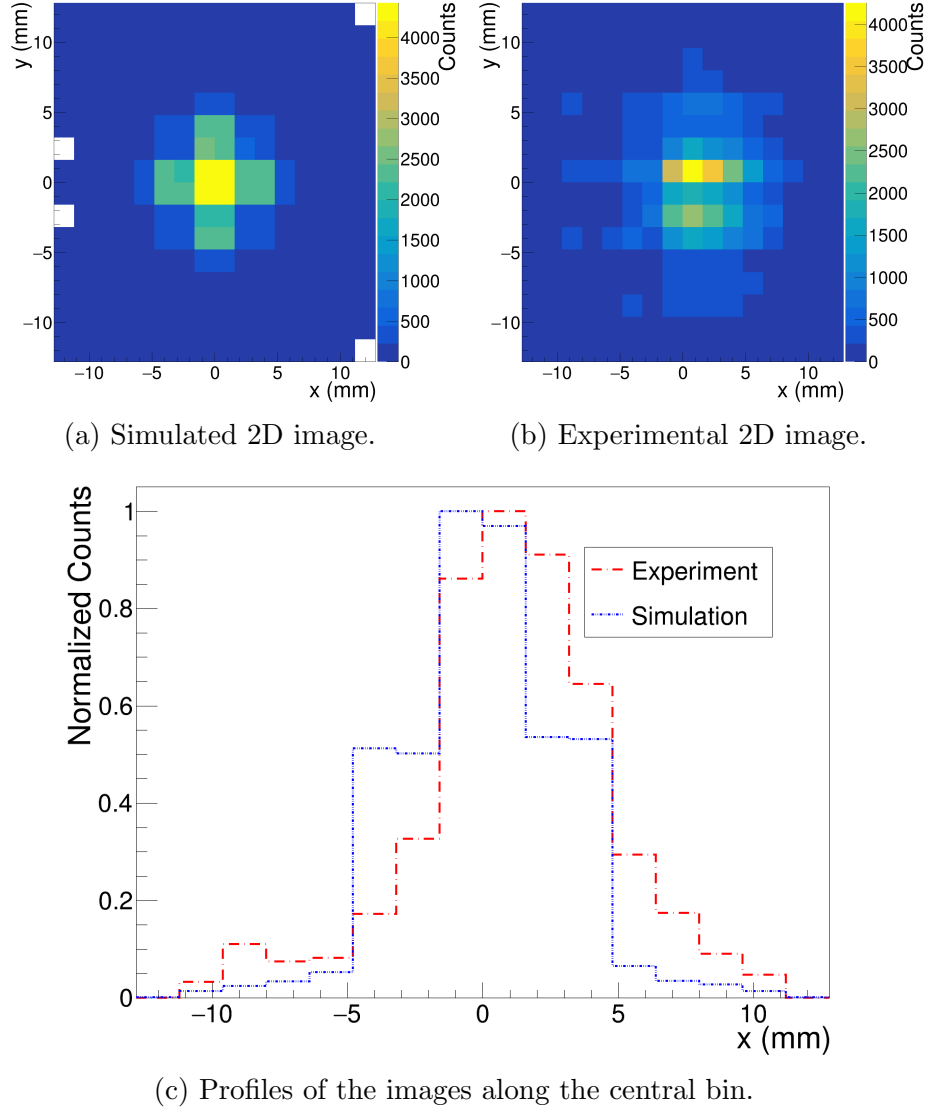


Figure 4.10: Images of the small vial filled with the ^{111}Ag solution with activity 7.36 MBq. The vial is placed in the central position on top of the collimator. Left is the simulated image and right is experimental one. From [120].

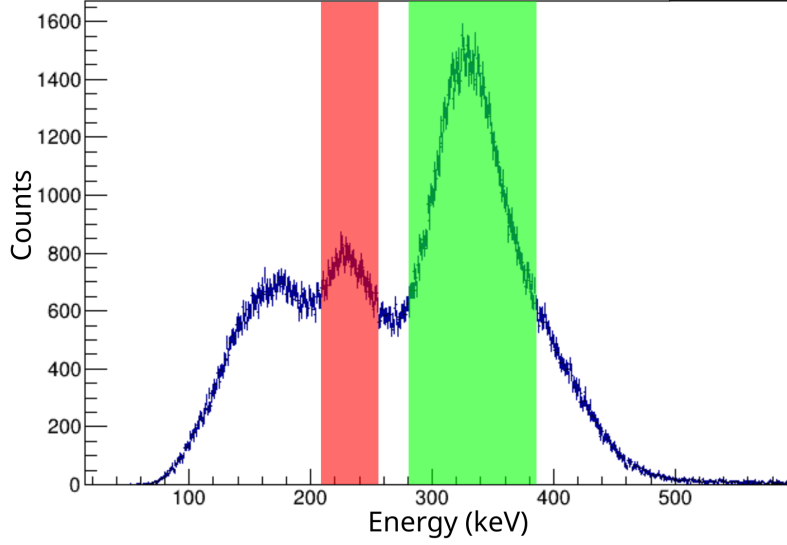


Figure 4.11: Total charge for the large vial acquisition with energy windows on the 245 keV (red band) and 342 keV (green band) peaks.

Energy window

Defining energy windows for the two peaks of ^{111}Ag is possible with the energy resolution of this device. The acquisition with the ^{111}Ag source in contact with the scintillator, thus without the collimator, was used to determine the calibration factor. The choice is convenient, since this run has the energy spectrum with the lowest noise. Gaussian curves were used to fit the two peaks, and to estimate the centroids with their uncertainty. Using the two pairs of points at 342 keV and 245 keV, the calibration factor can be estimated as 0.0828(3) keV/ch. The calibrated energy spectrum of the acquisition with the large vial is shown in Figure 4.11; for comparison, the non-calibrated energy spectrum was shown in Figure 4.9. The 342 keV peak has a FWHM of about 90 keV. Selecting the events in the [280, 385] keV range, reduces the contribution of the Compton scattering in the events position images. This filter can be regarded as an alternative to background subtraction. This method does not need an additional acquisition but, on the other hand, it does not remove the environmental sources of noise. If the acquisition is sufficiently fast, the environmental contribution can be neglected. The time required to gather enough statistics depends on the radionuclide activity.

Applying the energy window discards a portion of the recorded events, as they are deemed uninformative for source position reconstruction. Figure 4.12 compares two profiles of the single vial acquisition with collimator.

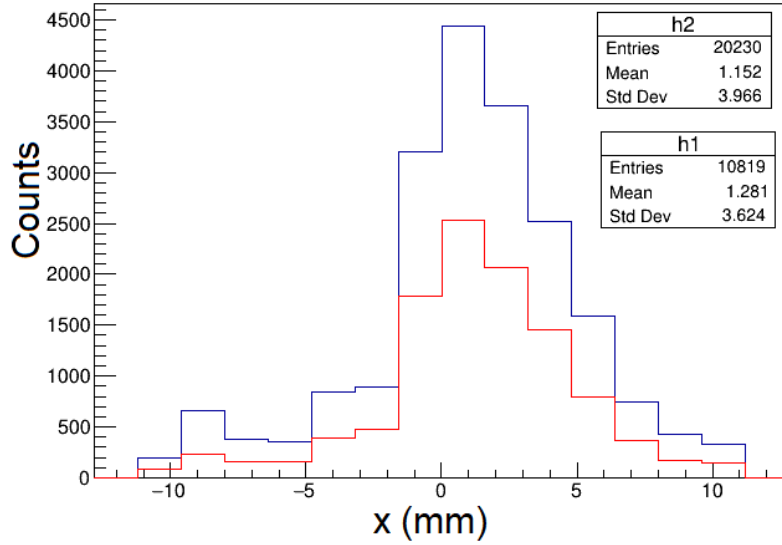


Figure 4.12: Acquisition of the small vial with 7.36 MBq of ^{111}Ag placed on top of the collimator in the central position with energy window centered on the 342 keV peak. The profile along the central position is shown for both the raw data (blue) and the filtered data with the energy window (red).

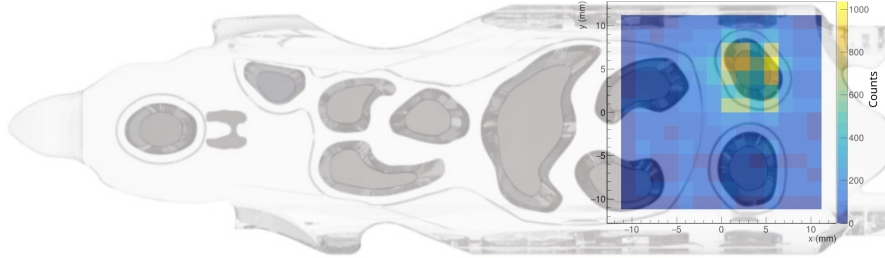


Figure 4.13: Acquisition of the phantom bladder filled with ^{111}Ag superimposed with the phantom geometry.

The one with more counts (blue line) is obtained from the raw data; the one with fewer counts (red line) is obtained by applying the energy window to the raw data. Both profiles represents a single-bin projection of the bins passing through the center of the 2D position histogram. The standard deviation of the filtered data profile (3.6 mm) is smaller than that of the raw data (4.0 mm).

Imaging of mouse phantom

The mouse phantom images were acquired to test the feasibility of in vivo imaging with this device. Three images were acquired, each corresponding to a different configuration of organ wells with the ^{111}Ag solution: one with the bladder only, one with the bladder and kidneys and one with the bladder, kidneys and liver. Since the gamma-ray collimation is provided by a parallel-holes collimator, the FOV of the gamma camera corresponds to the sensitive area of the SiPM: 5 cm^2 . Such FOV is not sufficient to cover the whole phantom in a single acquisition. Therefore, for each acquisition, the phantom was shifted with respect to the center of the gamma-camera to ensure that the organs of interest were within the FOV. Figure 4.13 shows the acquisition of the bladder as an example. The spatial resolution is sufficient to localise the organ of interest.

4.5 Conclusion

The design of a gamma-camera tailored to the ^{111}Ag gamma radiation is presented. The realised gamma-camera is based on a well-established design consisting of: a parallel-holes tungsten collimator, a pixelated GAGG(Ce) scintillator, a silicone resin optical coupler and a 64-channels SiPM. The DAQ is performed by a FERS-5200 unit and controlled via the open source software Janus. A digital twin of this gamma-camera was built using the Geant4 toolkit for Monte Carlo simulations. The digital twin includes all elements from the collimator to the SiPM, while the front-end electronics are omitted. The simulation begins with the decay of the ^{111}Ag atoms and ends with the SiPM channel-wise collection of the scintillation photons. The simulation output is used to predict experimental results and guide the choice of construction parameters. For instance, the collimator has square holes with 2 mm sides, separated by 1 mm-thick septa.

The characterisation of this gamma-camera with ^{111}Ag was performed at the LENA laboratory of Pavia. Experimental results indicate that the gamma-camera can reach a spatial resolution of at least 6.8 mm. A mouse-shaped phantom was imaged to predict the gamma-camera performance in a preclinical scenario. The gamma-camera successfully distinguished ^{111}Ag distributions inserted in different organ sites, suggesting its potential for in vivo imaging applications.

Chapter 5

Preclinical studies with ^{111}Ag

As with any drug development process, the creation of new radiopharmaceuticals requires extensive logistical and regulatory validation. Before they can be used in humans, they must undergo physicochemical and biological characterisation to prove their safety and suitability for the intended clinical application. This whole process is defined as *preclinical development* [9]. In general, specialised infrastructure and expertise are needed to carry out the aforementioned tests. The steps required to develop a radiolabelled drug suitable for clinical practice are summarised in Table 5.1. In this chapter, a series of preliminary preclinical experiments is described, aimed at investigating the potential of ^{111}Ag as a theranostic radionuclide. The preclinical evaluation can be roughly divided into three parts: physical and chemical properties assessment, in vitro evaluation and in vivo and ex vivo assessment. Each part evaluates specific criteria, with the last focusing on in vivo biodistribution, pharmacokinetics, toxicity and dose profile. Assessing all these aspects requires expertise from multiple fields, including physics, chemistry, biology and pharmaceuticals. Notably, adverse reactions to ther-

-
- | | |
|---|---|
| 1 | biological target identification and validation |
| 2 | lead molecule identification |
| 3 | lead molecule optimisation |
| 4 | labelling procedure development |
| 5 | preclinical assessment |
| 6 | upscaling of production |
| 7 | translation from preclinical to clinical phase |
-

Table 5.1: Phases required for the development of a radiopharmaceutical. From [9].

apeutic radiopharmaceuticals are primarily attributable to the radiation dose, rather than to the ligand properties. Such reactions are generally mild to moderate at therapeutic doses and minimal at diagnostics doses [131]. Biodistribution studies in mouse models were conducted using a multimodal imaging device, which is described in detail in the next section.

5.1 Characterisation of a multimodal imaging device

Multimodal imaging devices are widely used for preclinical studies. At the Center for Advanced Preclinical *in vivo* Research (CAPIR) laboratory in Catania, a Bruker In Vivo Xtreme (hereafter referred to as Xtreme) is used to perform the following imaging techniques:

- fluorescence;
- luminescence;
- digital autoradiography;
- X-Ray;
- reflectance.

The Xtreme uses a cooled, back-thinned CCD to detect optical photons. A phosphor screen is used to convert the high energy X-Rays or gamma-rays into optical photons detectable by the CCD.

The content of this section is adapted from the paper describing the phantom imaging activities carried out by the ISOLPHARM collaboration in 2023 [132]. The purpose of this study is to investigate a fast and reliable method for localising and quantifying ^{111}Ag activity for upcoming preclinical studies. To achieve this goal, imaging tests were performed of aqueous $^{111}\text{Ag}^+$ solutions contained in calibration phantoms. Images were acquired using Cerenkov Luminescence Imaging (CLI) and digital autoradiography (ARG). CLI is a cost-effective and faster alternative to standard nuclear imaging techniques for shallow imaging depths, as in the small animal studies planned within the ISOLPHARM collaboration [133, 134]. Indeed, CLI provides a valid method for imaging β^- -emitting radionuclides, such as ^{111}Ag . Several works demonstrated the possibility of performing *in vivo* imaging studies with nuclear medicine probes via CLI [135, 136]. However, due to the limited penetration depth of optical photons, CLI is more used in preclinical scenarios, even though some clinical tests have shown promising

Isotope	Half-life	Type	Mean Energy (keV)	Intensity (%)
^{68}Ga	68 m	$\beta+$	836	88
		γ	511	178
^{111}Ag	7.45 d	$\beta-$	360	92
		γ	342	6.7
		γ	245	1.2

Table 5.2: Decay features of ^{111}Ag and ^{68}Ga .

results [134]. In the future, clinical imaging with ^{111}Ag will rely on its highly penetrating gamma radiation, utilised in scintigraphy and SPECT. In the study presented in this chapter, digital autoradiography was used to acquire gamma-ray images of ^{111}Ag . Autoradiography is a consolidated technique based on the scintillation phenomenon, as in scintigraphy and SPECT [137, 138]. The analyses were complemented by the development of a simulation tool, to assist in the interpretation of the acquired images.

The same experiments were performed using ^{68}Ga , a positron emitter commonly used in nuclear medicine, to compare the ^{111}Ag data with those of a well-known radiotracer. ^{68}Ga emits positrons with an average energy of 836 keV [139], which subsequently annihilate generating two 511 keV gamma-rays. Table 5.2 summarises the decay characteristics of the ^{68}Ga and ^{111}Ag .

Material and experimental protocol

For the experiments presented in this chapter, ^{111}Ag is produced via neutron capture reaction on a palladium target, irradiated in the TRIGA Mark II nuclear reactor at the LENA laboratories in Pavia. For the purpose of the present work, 500 mg of natural palladium were irradiated for 8 hours in the central thimble of the reactor. The irradiated target was dissolved, and a reformulation process was used to obtain the aqueous solution containing $^{111}\text{Ag}^+$, which was delivered to the CApiR laboratory in Catania [140]. The details regarding the ^{111}Ag production procedure are described in Section 2.

The ^{68}Ga solution was supplied by the Cannizzaro Hospital of Catania, where it is routinely obtained from a $^{68}\text{Ge}/^{68}\text{Ga}$ generator for clinical practice.

The images were acquired using a Bruker In Vivo Xtreme, an optical planar imaging system designed for small animals and cell cultures. This system is capable of performing multimodal imaging analyses, including Bioluminescence Imaging (BLI), Multispectral VIS-NIR Fluorescence Imaging

(MS-FLI), Direct Radioisotopic Imaging (DRI), CLI and X-Ray Imaging. DRI is the Bruker proprietary name for ARG, the former will be used in the context of this work [141, 142].

The Xtreme is based on a reverse detection platform, with an optical system placed underneath the sample support, focusing the optical photons onto a 4 MP back-thinned -90°C deeply-cooled Charge-Coupled Device (CCD) camera. The camera has 4 MP (2048×2048), with each pixel measuring $13.5\mu\text{m}$ on a side. BLI, FLI and CLI utilise the optical light produced within the sample itself. Conversely, DRI and X-Ray imaging use a scintillator plate which converts high-energy radiation into visible and near-visible photons.

The instrument is equipped with animal chambers and beds. Anaesthesia and evacuation systems enable in vivo studies while ensuring animal welfare and end-user safety. The acquisition is managed by the Bruker Molecular Imaging (BMI) software package, version 7.5.2.22464. BMI allows the configuration of a large set of acquisition parameters, including illumination, excitation and emission filters, Field Of view (FOV) and camera exposure times. Even though the present study is based on the use of phantoms, these features will become crucial in upcoming in vivo experiments with mouse models and ^{111}Ag .

The phantoms were custom-made by the INFN-LNL workshop, with a design based on the Jaszczak phantoms [143]. They consisted of a set of three equally deep, parallel hollow rods with uniform cross sections. Each hole was positioned so that the minimum distance between two of holes was equal to their diameter. Three different models were produced by the LNL workshop, with cylinder diameters of 2, 3 and 5 mm. A fourth model was included, with each of the three holes having different diameter. The phantom controlled geometry allows for more precise and accurate quantitative analysis of the collected images. The phantoms were made of Poly Methyl MethAcrylate (PMMA), a transparent material that allowed Cerenkov photons to escape from the phantom volume. Figure 5.1 shows the top and lateral views of the phantom with 3 mm diameter holes.

The LBC detector is made of a Scionix LaBrCl(Ce) scintillator crystal and a Hamamatsu PMT model R6231-100-01, optically coupled with an ELJEN Technology EJ-560 silicone rubber band [46]. A 3D printed plastic case protects the detector sensitive components. The output signal from the detector is read out by a CAEN DT-5725SB digitiser. High voltage is provided by a CAEN DT547N module and configured using the custom-developed CAENHV_CTRL software. Data acquisition is managed by the open source Acquisition and Broadcast of Collected Data (ABCD) software [144]. The activity of a sample can be estimated from the acquisition

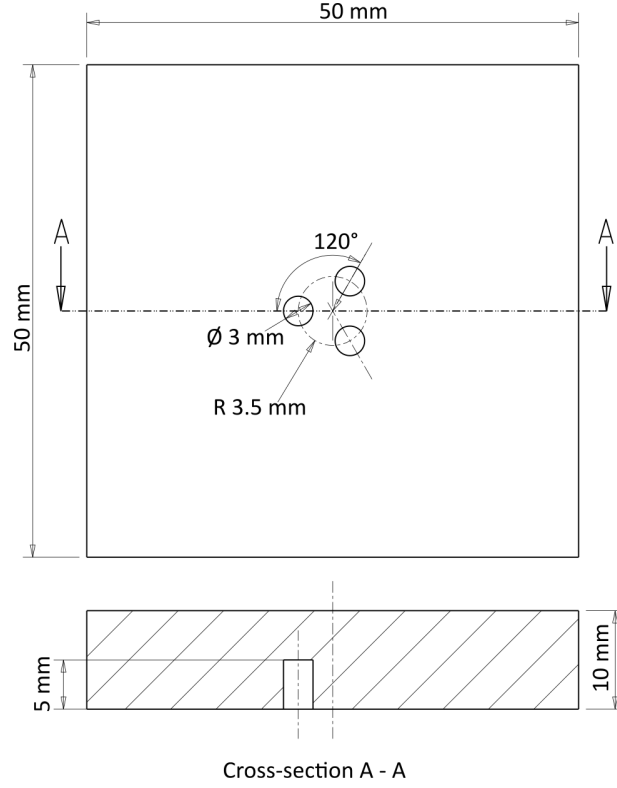


Figure 5.1: Phantom design scheme.

of a gamma-ray energy spectrum with the LBC detector. The formula that relates the counts to the activity is:

$$A = \frac{N}{\epsilon I_{\gamma} \Delta t} \quad (5.1)$$

where N is the number of counts in the full-energy peak associated with a specific transition, ϵ is the absolute efficiency at the energy of interest, I_{γ} is the branching ratio of the considered transition and Δt is the acquisition time in seconds (much shorter than the radionuclides half-lives). N is obtained fitting the peak of interest (342 keV for ^{111}Ag and 511 keV for ^{68}Ga). The Geant4 simulation of the detector used in the experiment was used to estimate ϵ [145].

At the beginning of the experiment, the activity of the $^{111}\text{Ag}^+$ and $^{68}\text{Ga}^{3+}$ stock solutions was measured, resulting 15.3 MBq and 247 MBq in volumes of 4.7 mL and 5 mL respectively. Both radioactive solutions were kept inside vials placed in a shielded container. The activity of the radioactive solutions was measured using the LBC detector, with a source-detector distance of 10 cm.

Nuclide	10 μL	30 μL	75 μL
^{68}Ga	362 kBq	1.1 MBq	2.7 MBq
^{111}Ag	31 kBq	94 kBq	236 kBq

Table 5.3: Activity of ^{68}Ga and ^{111}Ag at the start of the experiment according to the hole volume.

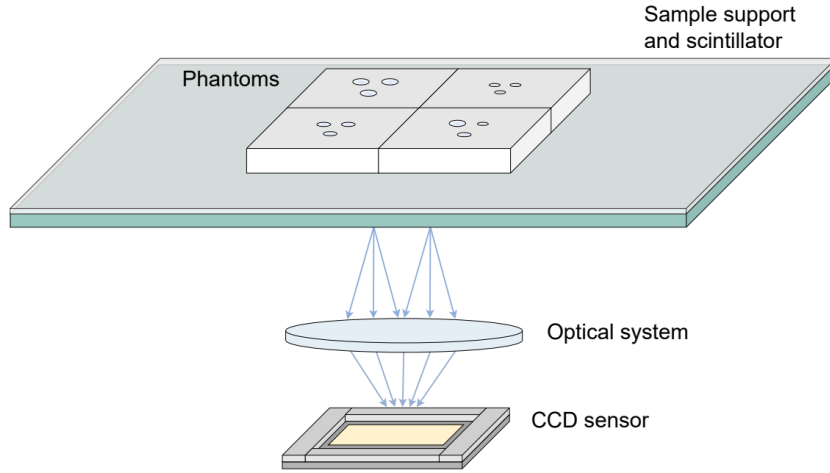


Figure 5.2: Scheme of the geometry used in the data collection. The scintillator, represented by the green screen right below the sample support, is only present in the DRI acquisition mode.

The holes of the phantoms were filled with either the ^{68}Ga or the ^{111}Ag solution using a micropipette. The inserted solution volume was determined by the diameter of the holes. Holes of 2, 3, and 5 mm diameter were filled with 10, 30, and 75 μL , respectively. The total activity for these volumes is reported in Table 5.3. The phantoms were covered in plastic wrap to avoid contaminations, and placed inside the Xtreme imaging cabinet to perform the acquisitions. The phantoms were placed on a sample holder consisting of a transparent plastic layer, with the holes facing upward. A total of four phantoms, one for each of the models described above, was used for the image acquisitions. A scheme of the setup is shown in Figure 5.2. The samples were placed in the center of the plate. The CLI and DRI images were acquired using the BMI software, with the CCD sensor set to the default 1×1 binning, and saved in the Digital Imaging and Communications

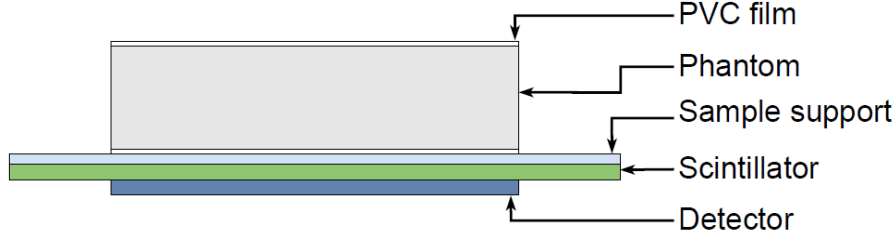


Figure 5.3: Scheme of the geometry used in the simulations. From [146].

in Medicine (DICOM) format.

Alongside the image acquisitions, the activity of each phantom was estimated from the measured activity per milliliter and the injected volume. A correlation between the collected light and the activity within the phantom holes was investigated for both imaging methods.

Simulation of the imaging device

Monte Carlo simulations were developed to support the analysis and to provide useful information for the upcoming in vivo studies. The simulations were developed using Geant4, version 11.0.0 [40, 41, 42]. Geant4, described in more detail in the introduction, is an open source software used to simulate the passage of particles in matter. The scheme of the setup used in the simulations is shown in Figure 5.3. The setup consisted of a PMMA phantom with holes filled with water, a protective film, a PVC sample holder, a $\text{Gd}_2\text{O}_2\text{S}$ scintillating screen and a silicon detector. The optical system used by the Xtreme to focus optical photons onto the sensor was not modelled, as the internal structure of the Xtreme was unknown. Therefore, the detector was positioned directly in contact with the scintillator for DRI or with the sample support for CLI. The physics lists employed in the developed simulations are `G4EmStandardPhysics_option4`, `G4OpticalPhysics`, `G4DecayPhysics` and `G4RadioactiveDecayPhysics`.

The primary particles were the nuclei of interest, namely ^{111}Ag and ^{68}Ga . They were generated at rest and ready to decay. The generation and propagation of optical photons were handled by the optical photons physics list, which required specifying the refractive index for each material.

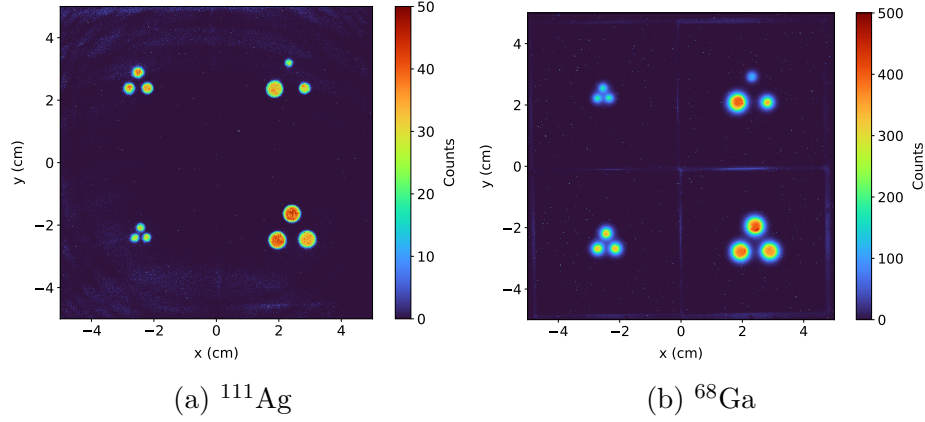


Figure 5.4: CLI images with ^{111}Ag a and ^{68}Ga b. For the ^{111}Ag image, phantoms diameters are 3 mm at top-left, mixed at top-right, 2 mm at bottom-left, 5 mm at bottom-right. For the ^{68}Ga image, phantoms diameters are 2 mm at top-left, mixed at top-right, 3 mm at bottom-left, 5 mm at bottom-right.

5.2 Imaging of ^{111}Ag phantoms

Cerenkov Luminescence Imaging of ^{111}Ag

The FOV of the device was sufficiently large to acquire the four phantom models in a single acquisition. Figure 5.4a and Figure 5.4b show the CLI acquisitions of the four phantoms with ^{111}Ag and ^{68}Ga , respectively. These images were obtained positioning the four phantoms inside the imaging cabinet and setting an exposure time of 10 minutes for silver and 3 minutes for gallium. In both images, the holes of each phantom are distinguishable, indicating a spatial resolution of at least 2 mm for the CLI method with the radionuclides used. Two differences between the radionuclide images can be observed: the image with ^{111}Ag features sharper edges, indicating higher spatial resolution but, on the other hand, the counts are significantly lower despite an acquisition time approximately the 3 times longer. Both observations can be attributed to the different energy spectra of the β -rays produced by the decay of the radionuclides. With a smaller average energy than ^{68}Ga positrons, ^{111}Ag electrons travel shorter distances within the material. Consequently, the light production is smaller and more localised [147]. Furthermore, the ^{68}Ga activity was approximately 5 times higher than that of ^{111}Ag at the time of acquisition.

Images were analysed to find a possible correlation between the collected light and the injected activity. Such correlation would enable the quantitative

Nuclide	$m(\text{kBq}^{-1} \text{s}^{-1})$	$q(\text{s}^{-1})$
^{68}Ga	21.8(7)	$-1.7(4) \times 10^3$
^{111}Ag	4.71(3)	2(39)

Table 5.4: Linear coefficients of the fits in the form $y = mx + q$ for ^{68}Ga and ^{111}Ag CLI images.

estimation of the local activity in future experiments. The images displayed clusters of signals corresponding to the radionuclide-filled holes. This structure suggests the use of clustering algorithms, such as the Density-Based Spatial Clustering of Applications with Noise (DBSCAN) [148].

The activity deposited in each hole was estimated using

$$A = V \cdot A_{\text{ml}} \quad (5.2)$$

where V is the volume of solution inserted in each hole and A_{ml} is the activity per milliliter of $^{111}\text{Ag}^+$ (or $^{68}\text{Ga}^{3+}$) solution at the time of the image acquisition. This activity was estimated from the measurements of the radioactive solution with the LBC detector. The estimated activity is corrected for the decay occurring during the time delay between the initial activity measurement and the image acquisition.

The total light output of the clusters showed a strong correlation with the activity. The Cerenkov images of both ^{111}Ag and ^{68}Ga yielded the same conclusions. The counts were normalised to the acquisition time. Figure 5.5 shows the counts per second as a function of the activity for the CLI data obtained with ^{111}Ag and ^{68}Ga . The linear fit was performed to highlight the linear correlation between these two quantities. The estimated linear coefficients are presented in Table 5.4.

Digital autoradiography of ^{111}Ag

A similar experimental procedure was performed to acquire DRI images of the four phantom models. Figure 5.6a and Figure 5.6b show the experimental images obtained with ^{111}Ag and ^{68}Ga , with an exposure time of 5 minutes and 30 seconds respectively.

A noticeable difference can be observed compared to CLI imaging: the holes within a single phantom are not distinguishable in DRI. Electrons with an energy of 360 keV have a mean Continuous Slowing Down Approximation (CSDA) range of about 1 mm in PMMA [149], meaning that the signal mainly originates from the gamma-rays emitted in the ^{111}Ag decay. In fact, most of the ^{111}Ag electrons cannot traverse the 5 mm thickness of

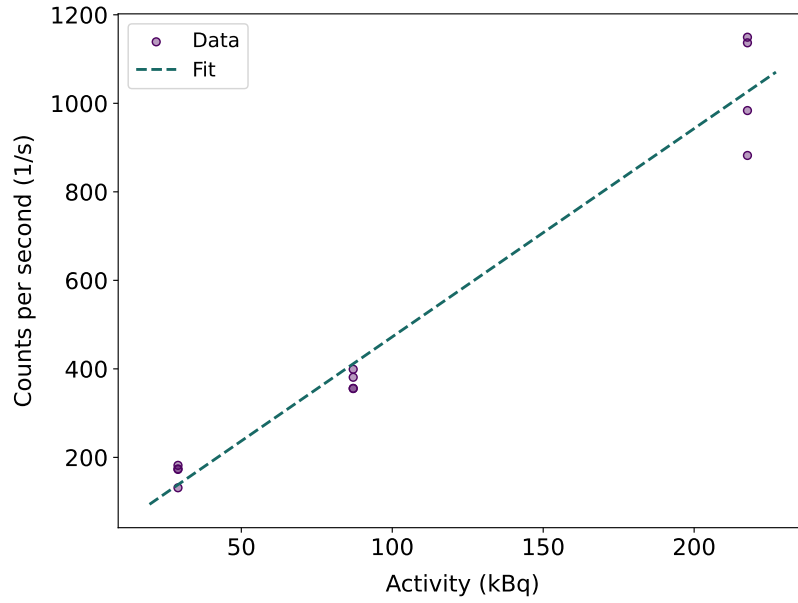
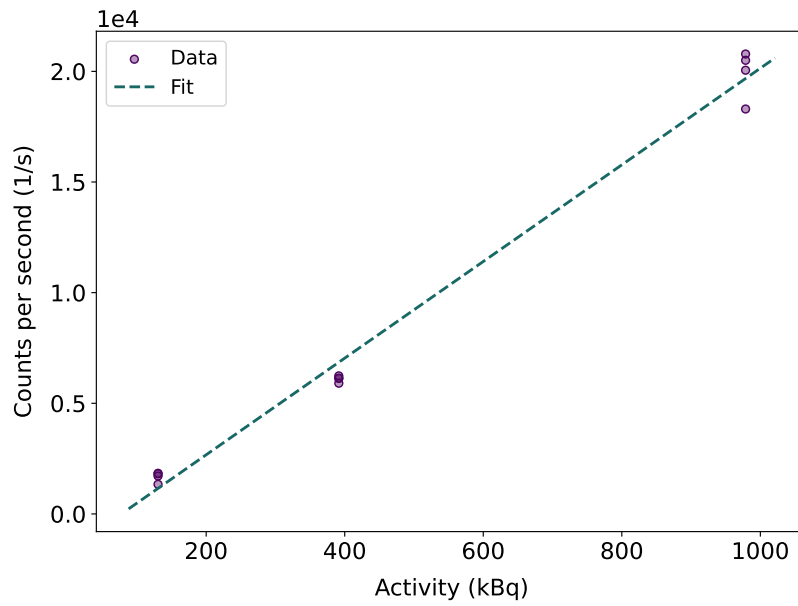
(a) ^{111}Ag correlation plot.(b) ^{68}Ga correlation plot.

Figure 5.5: Correlation plots with counts per second as function of the activity for each cluster in the CLI experimental image, dashed lines are linear fits. From [132].

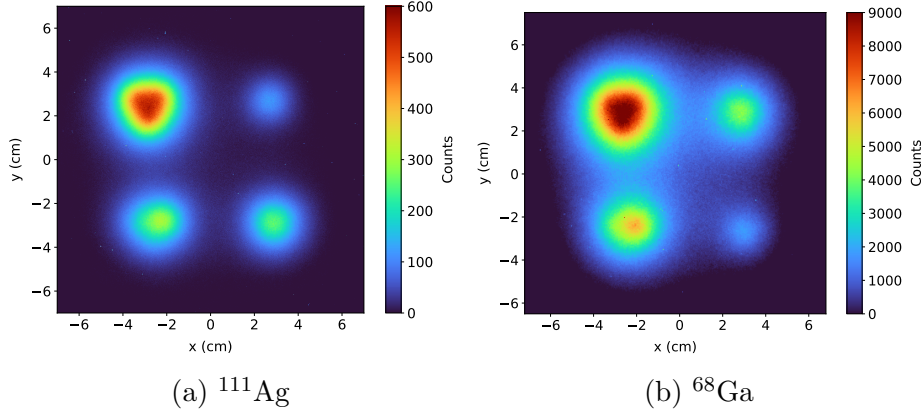


Figure 5.6: DRI images for the ^{111}Ag image, phantoms diameters are 5 mm at top-left, 2 mm at top-right, mixed at bottom-left, 3 mm at bottom-right. For the ^{68}Ga image, phantoms diameters are 5 mm at top-left, 3 mm at top-right, mixed at bottom-left, 2 mm at bottom-right.

PMMA separating the bottom of the holes from the scintillator screen. The same logic applies to the positrons generated in ^{68}Ga decay. Therefore, DRI images are generated only by the gamma-rays interacting with the scintillator plate. Considering the isotropic emission of such neutral particles and the fact that most of them traverse the PMMA without interacting, scintillation can occur far from the radioactive decay vertex. Consequently, the light distribution is broader than that in the CLI case, where the light production occurs only near the decay point.

5.3 Biodistribution of ^{111}Ag

The in vivo studies performed within the ISOLPHARM project were designed according to the 3R principles: replacement, reduction and refinement [150]. The aim of these studies is to evaluate the Pharmacokinetics (PK) of ^{111}Ag and of a ^{111}Ag -based radiopharmaceutical. The biological effect of ^{111}Ag has also been investigated, with a particular focus on the radiobiological mechanism, which differs from that of external beam radiotherapy [151].

Theoretical background

The biodistribution analysis considers the quantity called *injected activity*, which is defined as [152, 153]:

$$(\text{IA/g})_i = \frac{A_i(t_0)}{A_{\text{mouse}}(t_0)} \frac{1}{m_i} \quad (5.3)$$

where i is an index to each organ, m_i is the organ mass, $A_i(t_0)$ is the organ activity and $A_{\text{mouse}}(t_0)$ is the injected activity. Both activities are calculated at the injection time t_0 . To avoid contamination, the organs were placed in small vials before any measurement. To minimise the uncertainty in organ mass measurements, the tare from the vial masses should be subtracted:

$$m_i = M_i - M_{\text{vial},i} \quad (5.4)$$

On the other hand, a time-effective protocol is required to perform all necessary measurements within the limited time available after sacrifice. Therefore, a single value, the average vial mass, was subtracted from all mass measurements, as this procedure does not introduce an excessive uncertainty:

$$m_i = M_i - \langle M_{\text{vial}} \rangle \quad (5.5)$$

The activity values can be estimated from the full-energy peak areas measured by the LBC detector.

Consider a radioactive sample i with activity $A(t_i)$, the number of decays observed on average in the time interval $[t_{1,i}, t_{2,i}]$ is:

$$\Delta N_i = \int_{t_{1,i}}^{t_{2,i}} A_i(t) dt = A_i(t_{1,i}) \tau \left(1 - e^{-\frac{t_{2,i} - t_{1,i}}{\tau}} \right) \quad (5.6)$$

Turning the equation around, the activity calculated at the start of the acquisition can be written as:

$$A_i(t_{1,i}) = \frac{1}{\tau} \frac{\Delta N_i}{1 - e^{-\frac{t_{2,i} - t_{1,i}}{\tau}}} \quad (5.7)$$

For this formula, two limiting cases can be considered:

- when the acquisition time interval is much shorter than the radionuclide mean-life:

$$t_{2,i} - t_{1,i} \ll \tau \quad \implies \quad A_i(t_{1,i}) \simeq \frac{\Delta N_i}{t_{2,i} - t_{1,i}} \quad (5.8)$$

- when the acquisition time interval is much longer than the radionuclide half-life:

$$t_{2,i} - t_{1,i} \gg \tau \quad \implies \quad A_i(t_{1,i}) \simeq \frac{\Delta N_i}{\tau} \quad (5.9)$$

Since ^{111}Ag has a half-life of about seven days, the typical case corresponds to the first scenario. The relation between the decayed number of nuclei ΔN_i and the counts of the detector in the full-energy peak $\#_i$ is given by:

$$\#_i = \Delta N_i \Gamma \epsilon_{\text{abs}} \quad (5.10)$$

where Γ is the branching ratio of the specific channel and ϵ_{abs} is the absolute efficiency of the detector. Finally, the formula for short acquisition times results:

$$\text{IA/g} \simeq \frac{\#_i}{(t_{2,i} - t_{1,i}) \epsilon_{\text{abs}} \Gamma} \frac{1}{\exp\left(-\frac{t_{1,i} - t_0}{\tau}\right)} \frac{1}{A_{\text{mouse}}(t_0)} \frac{1}{M_i - M_{0,i}} \quad (5.11)$$

Experiment of March 2024

In March 2024, a biodistribution study was performed in healthy mice injected with ^{111}Ag . The radionuclide was produced at LENA with the protocol described in section 2. Two mice were injected with 60 μL of a solution containing ^{111}Ag . The first mouse was injected with 3.8 MBq and the second with 1.5 MBq. The solution was administered via intravenous tail injection. Images of the injected mice were acquired via autoradiography at several time-points, as shown in Figure 5.7. In this case, CLI did not provide sufficient light output. This fact can be an indication that the optical density of the mice tissues was too high. In all frames, the radionuclide is visible in the abdomen. In the first hours post-injection, ^{111}Ag traces are also present in the tail; as expected, this reflects the time required for the silver particles to circulate through the mouse body.

Three other mice were injected, but they were not included in this study because the radionuclide administration was unsuccessful. On the other hand, these failed administrations highlighted the non-negligible mortality risk associated with the injection of the solution. Several possible explanations were considered:

- physiological toxicity due to the formation of colloidal particles;
- toxicity from silver;
- toxicity from palladium contamination.

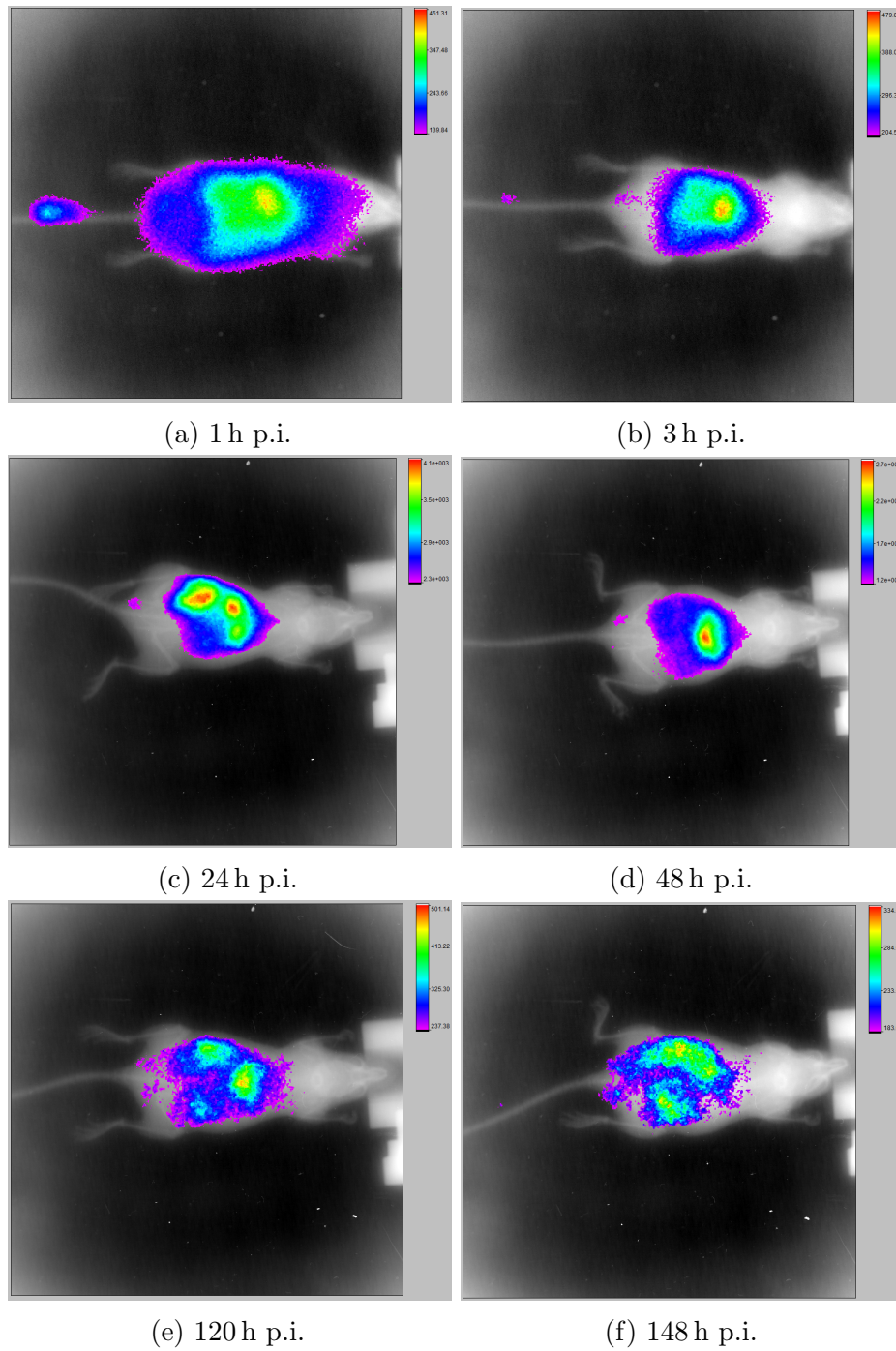


Figure 5.7: Autoradiography images of the mouse injected with 1.5 MBq of ^{111}Ag . Images are acquired at 1 h, 3 h, 24 h, 48 h, 120 h, 144 h post-injection. The gray-scale background is an X-Ray image.

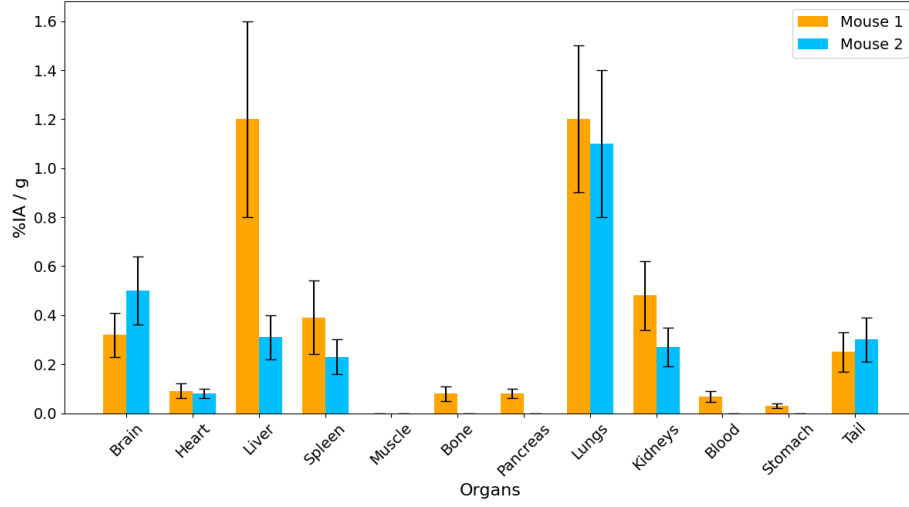


Figure 5.8: Mice biodistribution calculated as injected activity per gram per organ.

According to Paracelsus, the quantity determines whether a substance is a poison [154]. Based on this principle, silver toxicity is limited, as the 60 μL of solution contains only about 6 pmol, corresponding to a molar concentration of approximately 100 nmol L^{-1} . In vitro studies were conducted with palladium concentrations similar to those used in the experiments with mice in march 2024, and no cell toxicity related to palladium was observed. The mice that died after injection likely experiences physiological effects caused by the palladium component in the administered solution.

After the 144 h time-point, the mice were sacrificed, and the activity in each organ was measured ex vivo, as described in Section 5.3. Figure 5.8 shows the measured biodistributions. In accordance with the autoradiography images in Figure 5.7, the activity accumulates in the abdominal region, mainly in the lungs and liver. In particular, both mice show very high lung uptake.

The absolute efficiency of the detector is the primary source of uncertainty in the injected activity values. This uncertainty arises from the determination of the source-detector distance, which is difficult to evaluate under real experimental condition. The efficiency curve as a function of the source-detector distance was constructed using a Geant4 simulation [145]. Since each sample may occupy a different position within the vial, a uniform (box) distribution over a range of $\pm 4 \text{ mm}$ was assumed for the distance. This uncertainty leads to a corresponding error in the absolute efficiency estimation. Error propagation was applied, including contributions from both the sample mass and the counts in the full-energy peak.

5.4 Conclusion

The imaging potential of ^{111}Ag was assessed with a commercial multi-modal imaging device. Images are obtained with the Cerenkov Luminescence Imaging (CLI) technique and with digital AutoRadioGraphy (ARG). CLI demonstrated better spatial resolution compared to ARG: CLI could resolve cylinders with a 2 mm diameter, whereas ARG failed to distinguish even the 5 mm cylinders. On the other hand, CLI did not produce usable images in experiments with murine models. Therefore, ARG was employed for in vivo imaging of mice injected with a ^{111}Ag solution. The ARG images show accumulation of the radionuclide in the abdominal region. This result is confirmed by ex vivo biodistribution measurements, carried out for each explanted organ using a LBC gamma-ray detector. In particular, both mice exhibited preferential uptake in the lungs.

In the future, similar biodistribution studies will be conducted using solutions containing chelated ^{111}Ag and, subsequently, targeted ^{111}Ag . Within this framework, the present study with ^{111}Ag will serve as a reference for evaluating the targeting efficiency of the chosen targeting agent. The Prostate-Specific Membrane Antigen (PSMA) receptor, which is targeted by the recently approved radiopharmaceutical ^{177}Lu -PSMA-617, could be a suitable choice for the ^{111}Ag -based radiopharmaceutical.

Conclusion

Cancer is one of the leading causes of death; therefore, research in this field has an immediate impact on public health. Targeted Radionuclide Therapy (TRT) is a treatment protocol routinely used in clinical practice. This technique can be applied in a wide range of cases, thanks to the different physical characteristics of radionuclides, such as half-life, type of emission and corresponding energy. The work described in this thesis is part of the ISOLPHARM project, which aims to produce medical radionuclides using the Isotope-Separation On-Line (ISOL) technique. ISOLPHARM production will take place at the SPES facility, located at the Legnaro National Laboratories of the Italian National Institute for Nuclear Physics (INFN-LNL). Among the producible candidates, ^{111}Ag has attracted particular attention because it features decay properties suitable for medical applications: β -emission with a mean energy of 360 keV and γ -emission at 342 keV, with a half-life of 7 days. The ISOLPHARM project has been conducting experiments to demonstrate the suitability of this radionuclide for theranostic applications and to develop a radiopharmaceutical candidate. Achieving these goals, requires expertise from multiple fields, resulting in a multi-disciplinary collaboration. The work described in this PhD thesis contributes to this effort, addressing several aspects of the research: from radionuclide production at the ISOL SPES facility to preclinical experiments. Given the broad range of topics covered, this thesis has a strongly inter-disciplinary focus.

^{111}Ag is still studied by only a small number of research groups, partly because its production route is expensive. Producing this radionuclide via neutron capture reactions at nuclear research reactors requires enriched palladium targets to achieve high specific activities. In chapter 2, radionuclide production using the ISOL technique at SPES is discussed, with a focus on ^{111}Ag . The relevant equations for the production rate are presented, detailing the various contributing factors. The Resonant Ionisation Laser Ion Source (RILIS) provides high efficiency and high element selectivity. An ionisation scheme for the resonant steps of ^{111}Ag (and silver in general)

was studied. Regarding the collection of radionuclides in the final part of the ISOLPHARM beamline, the development and installation of the ISOLPHARM Radionuclide Implantation Station (IRIS) in the SPES low-energy experimental hall is described. IRIS can be conceptually divided into two parts: an Implantation Station (IS) and an Offline Detection System (ODS). The presented IRIS design emphasises remote operations to minimise the time operators spend near radioactive samples. The reliability of the IS was tested using thin tablets with diameter of 13 mm and thickness between 1.0 mm and 1.2 mm. The ODS consists of two detectors with different features: a germanium detector and an inorganic LBC scintillator. Both detectors were characterised and prepared for activity quantification of the collected radioactive samples. For the ^{111}Ag 342 keV gamma-ray, the germanium detector has a full-energy peak absolute efficiency of $\sim 0.6\%$. A GUI was designed to enable operators to manage the radionuclide collection workflow. Behind this intuitive GUI, lies an EPICS-based Input/Output Controller (IOC). Several materials were tested as substrates for implantation, with pharmaceutical-grade sorbitol and hypromellose selected as the most promising candidates. A second version of IRIS will be designed to address the weak points identified during real online radionuclide collections at SPES.

The development and characterisation of an innovative device for beta-imaging, named Detector Using MAPS for Beta-rays Observation (DUMBO), is presented in chapter 3. The sensitive part of this device consists of a set of ALice P*IX*el D*ET*ector (ALPIDE) chips, originally developed for the inner tracking system of the ALICE experiment at CERN. These chips have a sensitive area of approximately $30 \times 15 \text{ mm}^2$, composed of 1024×512 squared pixels with a side of $28 \mu\text{m}$. A front-end electronics system was developed to control and read out these chips. A pair of motors is used to move the sample relative to the ALPIDE chips, enabling micrometer-precision positioning and increasing the available Field Of View. A custom python script was implemented to perform data acquisition and control the motors. DUMBO is specifically designed to provide images of ^{111}Ag distributions. The first experiments with the complete DUMBO system, using ^{111}Ag provided by the LENA laboratory in Pavia, are described. Images of ^{111}Ag phantoms were obtained; nevertheless, several critical points of the system were identified. In particular, the mechanical stability of the ALPIDE chips and the DAQ protocol will be addressed in future upgrades.

A custom gamma-camera was designed, specifically suited for the energies of the ^{111}Ag gamma-rays: 245 keV and 342 keV. The device consists of the following components: a parallel-hole tungsten collimator with square geometry; a GAGG(Ce) scintillator array composed of 1 mm side rods; a silicone resin pad for optical coupling; a 8×8 channel SiPM; and a FERS-5200

unit board for readout. The choice of several design parameters was guided by Geant4 simulations of the device. The gamma-camera was characterised at LENA, which supplied the required ^{111}Ag solution. The estimated spatial resolution is approximately 6.8 mm, sufficient for imaging activity biodistributions in preclinical experiments. Indeed, images of a mouse phantom filled with the radioactive solution were acquired and different organs could be distinguished.

The first imaging tests with ^{111}Ag are described in chapter 5. These tests were performed using a multi-modal imaging device and custom phantoms containing a ^{111}Ag solution provided by LENA. Images of these phantoms were acquired using both Cerenkov Luminescence Imaging (CLI) and digital AutoRadioGraphy (ARG). ARG has lower spatial resolution than CLI but produces a higher light output. This difference was crucial in experiments with live mice, as the generated Cerenkov light was not able to penetrate the tissue for detection. ARG in vivo images of the mice showed accumulation of the radionuclide in the abdominal region. The same result was confirmed by ex vivo biodistribution studies using a dedicated gamma-ray detector. The lung tissue of the mice contained the highest injected activity per gram. In the future, the ISOLPHARM collaboration will carry out further preclinical experiments to investigate the efficacy of a ^{111}Ag -based radiopharmaceutical for cancer treatment.

Bibliography

- [1] *Global Cancer Observatory*. URL: <https://gco.iarc.who.int/> (visited on 12/22/2024).
- [2] Beilei Liu et al. “Exploring treatment options in cancer: tumor treatment strategies”. In: *Signal Transduction and Targeted Therapy* 9.1 (July 2024), p. 175. ISSN: 2059-3635. DOI: 10.1038/s41392-024-01856-7. URL: <https://doi.org/10.1038/s41392-024-01856-7>.
- [3] Mahdi Sadeghi, Milad Enferadi, and Alireza Shirazi. “External and internal radiation therapy: Past and future directions”. In: *Journal of Cancer Research and Therapeutics* 6.3 (2010). ISSN: 0973-1482. URL: https://journals.lww.com/cancerjournal/fulltext/2010/06030/external_and_internal_radiation_therapy__past_and.2.aspx.
- [4] Ravi A. Chandra et al. “Contemporary radiotherapy: present and future”. In: *The Lancet* 398.10295 (July 2021), pp. 171–184. ISSN: 0140-6736. DOI: 10.1016/S0140-6736(21)00233-6. URL: [https://doi.org/10.1016/S0140-6736\(21\)00233-6](https://doi.org/10.1016/S0140-6736(21)00233-6).
- [5] Michael R. Kilbourn and Peter J. H. Scott, eds. *Handbook of Radiopharmaceuticals: Methodology and Applications*. 2nd ed. Hoboken, NJ: Wiley, 2021, p. 768. ISBN: 978-1-119-50054-4.
- [6] National Research Council (US) and Institute of Medicine (US) Committee on State of the Science of Nuclear Medicine. *Advancing Nuclear Medicine Through Innovation*. Accessed: 2025-10-04. Washington, DC: National Academies Press (US), 2007. Chap. B, Glossary and Acronyms. URL: <https://www.ncbi.nlm.nih.gov/books/NBK1480/>.
- [7] Michele Ballan. “Sviluppo di bersagli per la produzione di radionuclidi di interesse medico secondo la tecnica ISOL”. PhD thesis. Università degli Studi di Ferrara, 2018. URL: <https://hdl.handle.net/11392/2488258> (visited on 01/05/2025).

- [8] F. F. Knapp and Ashutosh Dash. *Radiopharmaceuticals for Therapy*. Springer India, 2016. Chap. 16. ISBN: 9788132226079. DOI: 10.1007/978-81-322-2607-9_16. URL: http://dx.doi.org/10.1007/978-81-322-2607-9_16.
- [9] *Guidance for Preclinical Studies with Radiopharmaceuticals*. Radioisotopes and Radiopharmaceuticals Series 8. STI/PUB/2031. Vienna: International Atomic Energy Agency, 2023. ISBN: 978-92-0-139322-7. URL: <https://www.iaea.org/publications/14818/guidance-for-preclinical-studies-with-radiopharmaceuticals>.
- [10] Brian J. Burkett et al. “A Review of Theranostics: Perspectives on Emerging Approaches and Clinical Advancements”. In: *Radiology: Imaging Cancer* 5.4 (2023). PMID: 37477566, e220157. DOI: 10.1148/rycan.220157. eprint: <https://doi.org/10.1148/rycan.220157>. URL: <https://doi.org/10.1148/rycan.220157>.
- [11] Xijian Chen et al. “A Proof-of-Concept Study on the Theranostic Potential of ^{177}Lu -labeled Biocompatible Covalent Polymer Nanoparticles for Cancer Targeted Radionuclide Therapy”. In: *Chemistry - A European Journal* 30.9 (2024), e202303298. DOI: <https://doi.org/10.1002/chem.202303298>. eprint: <https://chemistry-europe.onlinelibrary.wiley.com/doi/pdf/10.1002/chem.202303298>. URL: <https://chemistry-europe.onlinelibrary.wiley.com/doi/abs/10.1002/chem.202303298>.
- [12] Kushal Chakraborty et al. “Advances in Radionuclides and Radio-labelled Peptides for Cancer Therapeutics”. In: *Pharmaceutics* 15.3 (2023). ISSN: 1999-4923. DOI: 10.3390/pharmaceutics15030971. URL: <https://www.mdpi.com/1999-4923/15/3/971>.
- [13] Amit Dey et al. “Recent Advancements, Limitations, and Future Perspectives of the use of Personalized Medicine in Treatment of Colon Cancer”. In: *Technology in Cancer Research & Treatment* 22 (2023). PMID: 37248615, p. 15330338231178403. DOI: 10.1177/15330338231178403.
- [14] Yu Wu et al. “Molecular mechanisms of tumor resistance to radiotherapy”. In: *Molecular Cancer* 22.1 (June 2023), p. 96. ISSN: 1476-4598. DOI: 10.1186/s12943-023-01801-2. URL: <https://doi.org/10.1186/s12943-023-01801-2>.
- [15] Pat Zanzonico. “The MIRD Schema for Radiopharmaceutical Dosimetry: A Review”. In: *Journal of Nuclear Medicine Technology* 52.2 (2024), pp. 74–85. ISSN: 0091-4916. DOI: 10.2967/jnmt.123.265668.

- eprint: <https://tech.snmjournals.org/content/52/2/74.full.pdf>. URL: <https://tech.snmjournals.org/content/52/2/74>.
- [16] *Dosimetry for Radiopharmaceutical Therapy*. Non-serial Publications. Vienna: International Atomic Energy Agency, 2024. ISBN: 978-92-0-139523-8. DOI: <https://doi.org/10.61092/iaea.xlzb-6h67>. URL: <https://www.iaea.org/publications/15002/dosimetry-for-radiopharmaceutical-therapy>.
- [17] Maija Radzina et al. “Novel radionuclides: demand, production and distribution for translational research in Europe”. In: *EJNMMI Radiopharmacy and Chemistry* 9.1 (Dec. 2024). ISSN: 2365-421X. DOI: 10.1186/s41181-024-00318-3. URL: <http://dx.doi.org/10.1186/s41181-024-00318-3>.
- [18] Desiree Erika Fiaccabrino, Peter Kunz, and Valery Radchenko. “Potential for production of medical radionuclides with on-line isotope separation at the ISAC facility at TRIUMF and particular discussion of the examples of ^{165}Er and ^{155}Tb ”. In: *Nuclear Medicine and Biology* 94-95 (2021), pp. 81–91. ISSN: 0969-8051. DOI: <https://doi.org/10.1016/j.nucmedbio.2021.01.003>. URL: <https://www.sciencedirect.com/science/article/pii/S0969805121000184>.
- [19] Charlotte Harrison. “Biopharma dives into tumor-seeking radioactive drugs”. In: *Nature Biotechnology* 43.5 (May 2025), pp. 653–656. ISSN: 1546-1696. DOI: 10.1038/s41587-025-02681-1. URL: <https://doi.org/10.1038/s41587-025-02681-1>.
- [20] Sophie Poty et al. “ α -Emitters for Radiotherapy: From Basic Radiochemistry to Clinical Studies—Part 1”. In: *Journal of Nuclear Medicine* 59.6 (2018), pp. 878–884. ISSN: 0161-5505. DOI: 10.2967/jnumed.116.186338. eprint: <https://jnm.snmjournals.org/content/59/6/878.full.pdf>. URL: <https://jnm.snmjournals.org/content/59/6/878>.
- [21] Clemens Kratochwil et al. “ ^{225}Ac -PSMA-617 for PSMA-Targeted α -Radiation Therapy of Metastatic Castration-Resistant Prostate Cancer”. In: *Journal of Nuclear Medicine* 57.12 (2016), pp. 1941–1944. ISSN: 0161-5505. DOI: 10.2967/jnumed.116.178673. eprint: <https://jnm.snmjournals.org/content/57/12/1941.full.pdf>. URL: <https://jnm.snmjournals.org/content/57/12/1941>.
- [22] Eline L. Hooijman et al. “Implementing ^{225}Ac labelled radiopharmaceuticals: practical considerations and (pre-)clinical perspectives”. In: *EJNMMI Radiopharmacy and Chemistry* 9.1 (Feb. 2024), p. 9.

- ISSN: 2365-421X. DOI: 10.1186/s41181-024-00239-1. URL: <https://doi.org/10.1186/s41181-024-00239-1>.
- [23] Duxin Sun et al. “Why 90% of clinical drug development fails and how to improve it?” In: *Acta Pharmaceutica Sinica B* 12.7 (2022), pp. 3049–3062. ISSN: 2211-3835. DOI: <https://doi.org/10.1016/j.apsb.2022.02.002>. URL: <https://www.sciencedirect.com/science/article/pii/S2211383522000521>.
- [24] F. F. Knapp and Ashutosh Dash. *Radiopharmaceuticals for Therapy*. Springer India, 2016. Chap. 2. ISBN: 9788132226079. DOI: 10.1007/978-81-322-2607-9_2. URL: http://dx.doi.org/10.1007/978-81-322-2607-9_2.
- [25] Justin S. Klein, Tae Jin Kim, and Guillem Pratz. “Development of a Lensless Radiomicroscope for Cellular-Resolution Radionuclide Imaging”. In: *Journal of Nuclear Medicine* 64.3 (2023), pp. 479–484. ISSN: 0161-5505. DOI: 10.2967/jnumed.122.264021. eprint: <https://jnm.snmjournals.org/content/64/3/479.full.pdf>. URL: <https://jnm.snmjournals.org/content/64/3/479>.
- [26] GM Currie et al. “Radionuclide production”. In: *Radiographer* 58.3 (2011), pp. 46–52. DOI: <https://doi.org/10.1002/j.2051-3909.2011.tb00155.x>. eprint: <https://onlinelibrary.wiley.com/doi/pdf/10.1002/j.2051-3909.2011.tb00155.x>. URL: <https://onlinelibrary.wiley.com/doi/abs/10.1002/j.2051-3909.2011.tb00155.x>.
- [27] Cari Borrás and Michael G. Stabin. *Radiotheranostics - A Primer for Medical Physicists I: Physics, Chemistry, Biology and Clinical Applications*. CRC Press, Jan. 2024. Chap. 11. ISBN: 9781003250913. DOI: 10.1201/9781003250913. URL: <http://dx.doi.org/10.1201/9781003250913>.
- [28] Kenneth S. Krane. *Introductory Nuclear Physics*. 2nd ed. New York: John Wiley & Sons, 1988. ISBN: 978-0-471-80553-3.
- [29] F. F. Knapp and Ashutosh Dash. *Radiopharmaceuticals for Therapy*. Springer India, 2016. Chap. 6. ISBN: 9788132226079. DOI: 10.1007/978-81-322-2607-9_6. URL: http://dx.doi.org/10.1007/978-81-322-2607-9_6.
- [30] *Manual for Reactor Produced Radioisotopes*. TECDOC Series 1340. Vienna: International Atomic Energy Agency, 2003. ISBN: 92-0-101103-2. URL: <https://www.iaea.org/publications/6407/manual-for-reactor-produced-radioisotopes>.

- [31] *Cyclotron Produced Radionuclides: Principles and Practice*. Technical Reports Series 465. STI/DOC/010/465. Vienna: International Atomic Energy Agency, 2008. ISBN: 978-92-0-100208-2. URL: <https://www.iaea.org/publications/7849/cyclotron-produced-radionuclides-principles-and-practice>.
- [32] Ferid Haddad et al. “ARRONAX, a high-energy and high-intensity cyclotron for nuclear medicine”. In: *European Journal of Nuclear Medicine and Molecular Imaging* 35.7 (July 2008), pp. 1377–1387. ISSN: 1619-7089. DOI: 10.1007/s00259-008-0802-5. URL: <https://doi.org/10.1007/s00259-008-0802-5>.
- [33] F. F. Knapp and Ashutosh Dash. *Radiopharmaceuticals for Therapy*. Springer India, 2016. Chap. 5. ISBN: 9788132226079. DOI: 10.1007/978-81-322-2607-9_5. URL: http://dx.doi.org/10.1007/978-81-322-2607-9_5.
- [34] A. Andrichetto et al. “The ISOLPHARM project: ISOL-based production of radionuclides for medical applications”. In: *Journal of Radioanalytical and Nuclear Chemistry* 322.1 (Oct. 2019), pp. 73–77. ISSN: 1588-2780. DOI: 10.1007/s10967-019-06698-0. URL: <https://doi.org/10.1007/s10967-019-06698-0>.
- [35] The ISOLPHARM collaboration. *ISOLPHARM – SPES beam for medicine*. URL: <https://isolpharm.pd.infn.it/web/> (visited on 12/24/2024).
- [36] *National Nuclear Data Center*. information extracted from the NuDat database. URL: <https://www.nndc.bnl.gov/nudat/> (visited on 12/24/2024).
- [37] Xavier Mougeot. “Atomic exchange correction in forbidden unique beta transitions”. In: *Applied Radiation and Isotopes* 201 (2023), p. 111018. ISSN: 0969-8043. DOI: <https://doi.org/10.1016/j.apradiso.2023.111018>. URL: <https://www.sciencedirect.com/science/article/pii/S0969804323003718>.
- [38] Bilge V. Salancı. “Radionuclide Pain Palliation Therapy”. In: *Radionuclide Therapy*. Ed. by Recep Bekiş, Berna Polack, and Murat Fani Bozkurt. Cham: Springer International Publishing, 2022, pp. 323–337. ISBN: 978-3-030-97220-2. DOI: 10.1007/978-3-030-97220-2_18. URL: https://doi.org/10.1007/978-3-030-97220-2_18.

- [39] Sankha Chattopadhyay et al. “Preparation and evaluation of a new radiopharmaceutical for radiosynovectomy, ^{111}Ag -labelled hydroxyapatite (HA) particles”. In: *Applied Radiation and Isotopes* 66.3 (Mar. 2008), pp. 334–339. ISSN: 0969-8043. DOI: 10.1016/j.apradiso.2007.09.003. URL: <http://dx.doi.org/10.1016/j.apradiso.2007.09.003>.
- [40] S. Agostinelli et al. “Geant4—a simulation toolkit”. In: *Nuclear Instruments and Methods in Physics Research Section A: Accelerators, Spectrometers, Detectors and Associated Equipment* 506.3 (2003), pp. 250–303. ISSN: 0168-9002. DOI: [https://doi.org/10.1016/S0168-9002\(03\)01368-8](https://doi.org/10.1016/S0168-9002(03)01368-8). URL: <https://www.sciencedirect.com/science/article/pii/S0168900203013688>.
- [41] J. Allison et al. “Geant4 developments and applications”. In: *IEEE Transactions on Nuclear Science* 53.1 (2006), pp. 270–278. DOI: 10.1109/TNS.2006.869826.
- [42] J. Allison et al. “Recent developments in Geant4”. In: *Nuclear Instruments and Methods in Physics Research Section A: Accelerators, Spectrometers, Detectors and Associated Equipment* 835 (2016), pp. 186–225. ISSN: 0168-9002. DOI: <https://doi.org/10.1016/j.nima.2016.06.125>. URL: <https://www.sciencedirect.com/science/article/pii/S0168900216306957>.
- [43] Rene Brun and Fons Rademakers. “ROOT — An object oriented data analysis framework”. In: *Nuclear Instruments and Methods in Physics Research Section A: Accelerators, Spectrometers, Detectors and Associated Equipment* 389.1 (1997). New Computing Techniques in Physics Research V, pp. 81–86. ISSN: 0168-9002. DOI: [https://doi.org/10.1016/S0168-9002\(97\)00048-X](https://doi.org/10.1016/S0168-9002(97)00048-X). URL: <https://www.sciencedirect.com/science/article/pii/S016890029700048X>.
- [44] Laboratorio Energia Nucleare Applicata (LENA). *Il Reattore*. URL: <https://lena.unipv.it/il-reattore/> (visited on 10/04/2025).
- [45] Marianna Tosato and Mattia Asti. “Lights and Shadows on the Sourcing of Silver Radioisotopes for Targeted Imaging and Therapy of Cancer: Production Routes and Separation Methods”. In: *Pharmaceuticals* 16.7 (2023). ISSN: 1424-8247. DOI: 10.3390/ph16070929. URL: <https://www.mdpi.com/1424-8247/16/7/929>.
- [46] L. Morselli et al. “Production and characterization of ^{111}Ag radioisotope for medical use in a TRIGA Mark II nuclear research reactor”. In: *Applied Radiation and Isotopes* 197 (2023), p. 110798. ISSN: 0969-8043. DOI: <https://doi.org/10.1016/j.apradiso.2023.110798>.

- URL: <https://www.sciencedirect.com/science/article/pii/S0969804323001513>.
- [47] R. E. Druschel and J. Halperin. *Thermal neutron cross section and resonance integral of 7.5-day silver-111*. Progress Report 3994. Oak Ridge National Lab. Reports. 1966, 7(1).
- [48] M Neves, A Kling, and R.M Lambrecht. “Radionuclide production for therapeutic radiopharmaceuticals”. In: *Applied Radiation and Isotopes* 57.5 (2002). A Special Issue dedicated to the memory of Richard M. Lambrecht 1943 - 2001, pp. 657–664. ISSN: 0969-8043. DOI: [https://doi.org/10.1016/S0969-8043\(02\)00180-X](https://doi.org/10.1016/S0969-8043(02)00180-X). URL: <https://www.sciencedirect.com/science/article/pii/S096980430200180X>.
- [49] Marco Mazzocco. “Radioactive Ion Beams: Production and Experiments at INFN-LNL”. In: *EPJ Web Conf.* 275 (2023), p. 01010. DOI: 10.1051/epjconf/202327501010. URL: <https://doi.org/10.1051/epjconf/202327501010>.
- [50] P. Van Duppen. “Isotope Separation On Line and Post Acceleration”. In: *The Euroschool Lectures on Physics with Exotic Beams, Vol. II*. Ed. by Jim Al-Khalili and Ernst Roeckl. Berlin, Heidelberg: Springer Berlin Heidelberg, 2006, pp. 37–77. ISBN: 978-3-540-33787-4. DOI: 10.1007/3-540-33787-3_2. URL: https://doi.org/10.1007/3-540-33787-3_2.
- [51] Gaia Pupillo et al. “Cyclotron-based production of innovative medical radionuclides at the INFN-LNL: state of the art and perspective”. In: *The European Physical Journal Plus* 138.12 (Dec. 2023), p. 1095. ISSN: 2190-5444. DOI: 10.1140/epjp/s13360-023-04564-3. URL: <https://doi.org/10.1140/epjp/s13360-023-04564-3>.
- [52] Charlotte Duchemin et al. “CERN-MEDICIS: A Review Since Commissioning in 2017”. In: *Frontiers in Medicine* 8 (2021). ISSN: 2296-858X. DOI: 10.3389/fmed.2021.693682. URL: <https://www.frontiersin.org/journals/medicine/articles/10.3389/fmed.2021.693682>.
- [53] C. Bernerd et al. “Production of innovative radionuclides for medical applications at the CERN-MEDICIS facility”. In: *Nuclear Instruments and Methods in Physics Research Section B: Beam Interactions with Materials and Atoms* 542 (Sept. 2023), pp. 137–143. ISSN: 0168-583X. DOI: 10.1016/j.nimb.2023.05.008. URL: <http://dx.doi.org/10.1016/j.nimb.2023.05.008>.

- [54] Davide Serafini, Patricija Kalnina, and Charlotte Duchemin. *Kromek CZT detector calibration for activity estimation of medical radionuclides at MEDICIS*. Tech. rep. CERN, 2025. URL: <https://edms.cern.ch/document/3230432/1>.
- [55] A. Andrichetto et al. “Low energy radioactive ion beams at SPES for nuclear physics and medical applications”. In: *Nuclear Instruments and Methods in Physics Research Section B: Beam Interactions with Materials and Atoms* 541 (2023), pp. 236–239. ISSN: 0168-583X. DOI: <https://doi.org/10.1016/j.nimb.2023.05.044>. URL: <https://www.sciencedirect.com/science/article/pii/S0168583X23002458>.
- [56] Lisa Centofante. “Study of a new target-ion source unit and beam line for an energy and power upgrade of the SPES project at INFN LNL”. PhD thesis. Università degli Studi di Brescia, 2022. URL: <https://hdl.handle.net/11379/555022> (visited on 01/05/2025).
- [57] S. Corradetti et al. “The SPES target production and characterization”. In: *Nuclear Instruments and Methods in Physics Research Section B: Beam Interactions with Materials and Atoms* 488 (2021), pp. 12–22. ISSN: 0168-583X. DOI: <https://doi.org/10.1016/j.nimb.2020.12.003>. URL: <https://www.sciencedirect.com/science/article/pii/S0168583X20305073>.
- [58] A. Andrichetto, S. Cevolani, and C. Petrovich. “Fission fragment production from uranium carbide disc targets”. In: *The European Physical Journal A - Hadrons and Nuclei* 25.1 (July 2005), pp. 41–47. ISSN: 1434-601X. DOI: [10.1140/epja/i2005-10064-8](https://doi.org/10.1140/epja/i2005-10064-8). URL: <https://doi.org/10.1140/epja/i2005-10064-8>.
- [59] O.S. Khwairakpam et al. “The SPES laser ion source: Time structure, laser enhancement and efficiency measurements with gallium at ISOLDE Offline 2”. In: *Nuclear Instruments and Methods in Physics Research Section B: Beam Interactions with Materials and Atoms* 548 (2024), p. 165249. ISSN: 0168-583X. DOI: <https://doi.org/10.1016/j.nimb.2024.165249>. URL: <https://www.sciencedirect.com/science/article/pii/S0168583X24000181>.
- [60] Omorjit Singh Khwairakpam. “Study, Development and Optimization of Laser Resonant Photo-Ionization processes applied to species of interest for the Isolpharm-SPES project”. PhD thesis. Università degli Studi di Siena, 2023. URL: <https://hdl.handle.net/11365/1247654> (visited on 01/05/2025).

- [61] F. Gramegna et al. “The SPES exotic beam ISOL facility: Status of the project, technical challenges, instrumentation, scientific program”. In: *Il Nuovo Cimento C* 5 (September-October 2018). DOI: 10.1393/ncc/i2018-18195-3. URL: <http://dx.doi.org/10.1393/ncc/i2018-18195-3>.
- [62] A. Monetti et al. “Study of the radionuclide deposition in the radioactive ion line of the Selective Production of Exotic Species (SPES) facility”. In: *Applied Radiation and Isotopes* 204 (2024), p. 111121. ISSN: 0969-8043. DOI: <https://doi.org/10.1016/j.apradiso.2023.111121>. URL: <https://www.sciencedirect.com/science/article/pii/S0969804323004748>.
- [63] Scientific Committees, European Commission (SCHER). *Does depleted uranium pose a radiation hazard?* European Commission, Directorate-General for Health and Consumers. 2010. URL: https://ec.europa.eu/health/scientific_committees/opinions_layman/depleted-uranium/de/1-3/4.htm (visited on 09/26/2025).
- [64] V.V. Zerkin and B. Pritychenko. “The experimental nuclear reaction data (EXFOR): Extended computer database and Web retrieval system”. In: *Nuclear Instruments and Methods in Physics Research Section A: Accelerators, Spectrometers, Detectors and Associated Equipment* 888 (2018), pp. 31–43. ISSN: 0168-9002. DOI: <https://doi.org/10.1016/j.nima.2018.01.045>. URL: <https://www.sciencedirect.com/science/article/pii/S0168900218300627>.
- [65] N. Otuka et al. “Towards a More Complete and Accurate Experimental Nuclear Reaction Data Library (EXFOR): International Collaboration Between Nuclear Reaction Data Centres (NRDC)”. In: *Nuclear Data Sheets* 120 (2014), pp. 272–276. ISSN: 0090-3752. DOI: <https://doi.org/10.1016/j.nds.2014.07.065>. URL: <https://www.sciencedirect.com/science/article/pii/S0090375214005171>.
- [66] S. Sarkar and L. Yaffe. “Nuclear charge distribution in the region of symmetric fission of ^{238}U by protons of energy 20–85 MeV”. In: *Canadian Journal of Chemistry* 54.15 (1976), pp. 2349–2358. DOI: 10.1139/v76-335. eprint: <https://doi.org/10.1139/v76-335>. URL: <https://doi.org/10.1139/v76-335>.
- [67] M. Montis et al. “EPICS Based Control System for SPES Tape Station for Beam Characterization: Motion System and Controls”. In: *Proc. ICALEPCS’19* (New York, NY, USA). International Conference on Accelerator and Large Experimental Physics Control Systems

17. <https://doi.org/10.18429/JACoW-ICALEPCS2019-MOPHA097>. JACoW Publishing, Geneva, Switzerland, Aug. 2020, pp. 440–443. ISBN: 978-3-95450-209-7. DOI: 10.18429/JACoW-ICALEPCS2019-MOPHA097. URL: <https://jacow.org/icalepcs2019/papers/mopha097.pdf>.
- [68] Massimo Giuseppe Martello. *Guida all'utilizzo di IRIS*. https://isolpharm.pd.infn.it/web/?page_id=4369. URL: https://isolpharm.pd.infn.it/web/?page_id=4369 (visited on 10/05/2025).
- [69] Wolfgang Demtröder. “Widths and Profiles of Spectral Lines”. In: *Laser Spectroscopy: Vol. 1 Basic Principles*. 4th ed. Berlin, Heidelberg: Springer Berlin Heidelberg, 2008. ISBN: 978-3-540-73418-5. DOI: 10.1007/978-3-540-73418-5. URL: <https://doi.org/10.1007/978-3-540-73418-5>.
- [70] V.I. Mishin et al. “Chemically selective laser ion-source for the CERN-ISOLDE on-line mass separator facility”. In: *Nuclear Instruments and Methods in Physics Research Section B: Beam Interactions with Materials and Atoms* 73.4 (Apr. 1993), pp. 550–560. ISSN: 0168-583X. DOI: 10.1016/0168-583x(93)95839-w. URL: [http://dx.doi.org/10.1016/0168-583X\(93\)95839-W](http://dx.doi.org/10.1016/0168-583X(93)95839-W).
- [71] CERN. *Motivation for RILIS*. <https://rilis-web.web.cern.ch/>. Accessed: 2025-11-29. 1990.
- [72] B Marsh. “Resonance Ionization Laser Ion Sources”. In: (2013). 61 pages, contribution to the CAS-CERN Accelerator School: Ion Sources, Senec, Slovakia, 29 May - 8 June 2012, edited by R. Bailey. DOI: 10.5170/CERN-2013-007.203. URL: <https://cds.cern.ch/record/1967371>.
- [73] Omorjit Singh Khwairakpam et al. “Resonant Laser Ionization and Fine-Structure Study of Silver in an Ablation Plume”. In: *Applied Sciences* 13.1 (2023). ISSN: 2076-3417. DOI: 10.3390/app13010309. URL: <https://www.mdpi.com/2076-3417/13/1/309>.
- [74] A. Kramida et al. NIST Atomic Spectra Database (ver. 5.12), [Online]. Available: <https://physics.nist.gov/asd> [2025, November 18]. National Institute of Standards and Technology, Gaithersburg, MD. 2024.
- [75] D. Scarpa et al. “New solid state laser system for SPES: Selective Production of Exotic Species project at Laboratori Nazionali di Legnaro”. In: *Review of Scientific Instruments* 93.8 (Aug. 2022), p. 083001. ISSN: 0034-6748. DOI: 10.1063/5.0078913. eprint: <https://pubs.aip.org/aip/rsi/article-pdf/doi/10.1063/5.0078913>

- 3/16612025/083001_1_online.pdf. URL: <https://doi.org/10.1063/5.0078913>.
- [76] The FLUKA Collaboration et al. “The FLUKA code: Overview and new developments”. In: *EPJ Nuclear Sci. Technol.* 10 (2024), p. 16. DOI: 10.1051/epjn/2024015. URL: <https://doi.org/10.1051/epjn/2024015>.
- [77] U. Köster. “How to produce intense and pure ISOL beams”. In: *Progress in Particle and Nuclear Physics* 46.1 (2001), pp. 411–412. ISSN: 0146-6410. DOI: [https://doi.org/10.1016/S0146-6410\(01\)00148-X](https://doi.org/10.1016/S0146-6410(01)00148-X). URL: <https://www.sciencedirect.com/science/article/pii/S014664100100148X>.
- [78] Sándor Takács. “Definitions of Yields: Problems and Confusions”. In: *EXFOR Workshop, 06–10 October 2014*. International Atomic Energy Agency (IAEA), NDS. Vienna, Austria, 2014. DOI: 10.6109/2/iaea.yemw-bzjx. URL: https://nds.iaea.org/nrdc/wksp_2014/present/takacs2.pdf.
- [79] A. Gottberg. “Target materials for exotic ISOL beams”. In: *Nuclear Instruments and Methods in Physics Research Section B: Beam Interactions with Materials and Atoms* 376 (2016). Proceedings of the XVIIth International Conference on Electromagnetic Isotope Separators and Related Topics (EMIS2015), Grand Rapids, MI, U.S.A., 11–15 May 2015, pp. 8–15. ISSN: 0168-583X. DOI: <https://doi.org/10.1016/j.nimb.2016.01.020>. URL: <https://www.sciencedirect.com/science/article/pii/S0168583X16000689>.
- [80] L. Moral and A. F. Pacheco. “Algebraic approach to the radioactive decay equations”. In: *American Journal of Physics* 71.7 (June 2003), pp. 684–686. ISSN: 1943-2909. DOI: 10.1119/1.1571834. URL: <http://dx.doi.org/10.1119/1.1571834>.
- [81] Daiyuan Chen. “Development of ISOLPHARM Radionuclide Implantation Station (IRIS) in the context of SPES-ISOLPHARM project”. submitted in 2025. PhD thesis. Università degli Studi di Padova.
- [82] M. Barbui et al. “Calculations and first results obtained with a SiC prototype of the SPES direct target”. In: *Nuclear Instruments and Methods in Physics Research Section B: Beam Interactions with Materials and Atoms* 266.19 (2008). Proceedings of the XVth International Conference on Electromagnetic Isotope Separators and Techniques Related to their Applications, pp. 4289–4293. ISSN: 0168-583X. DOI: <https://doi.org/10.1016/j.nimb.2008.05.049>. URL:

- <https://www.sciencedirect.com/science/article/pii/S0168583X08007222>.
- [83] Daiyuan Chen et al. “SPES Low-energy Beamline Status and Development of ISOLPHARM Radionuclide Implantation Station (IRIS)”. submitted to the Nuclear Instruments and Methods in Physics Research Section A journal in 2025.
 - [84] Serghei Popa. “Analisi e progettazione di un sistema di contenimento e movimentazione di un bersaglio per la raccolta di isotopi radioattivi di interesse medico”. MA thesis. University of Padova, 2018. URL: <https://hdl.handle.net/20.500.12608/25032>.
 - [85] Giorgio Bonavoglia. “Progettazione e sviluppo di un sistema di movimentazione di un bersaglio per la cattura di isotopi radioattivi di interesse medico”. MA thesis. University of Padova, 2020. URL: <https://hdl.handle.net/20.500.12608/22872>.
 - [86] Davide Martini. “Progettazione e sviluppo di un sistema di raccolta e movimentazione di bersagli per la deposizione di isotopi radioattivi di interesse medico”. MA thesis. University of Padova, 2021. URL: <https://hdl.handle.net/20.500.12608/22657>.
 - [87] Francesca Nicente. “Screening e sviluppo tecnologico di target di deposizione innovativi per la raccolta di radionuclidi medicali nell’ambito del progetto ISOLPHARM”. MA thesis. Università degli Studi di Padova, 2024. URL: <https://hdl.handle.net/20.500.12608/62059>.
 - [88] Damiano Cerioni. *Introduction to Research ISOLPHARM*. University internship. Tutor: Prof. Marcello Lunardon, Co-tutor: Davide Serafini. Università degli Studi di Padova, 2025.
 - [89] Michael Heines, Joris De Ridder, and Thomas E. Cocolios. “New best practices for efficiency fitting for accurate gamma-ray spectroscopy with semi-conductor detectors”. In: *Applied Radiation and Isotopes* 225 (2025), p. 112002. ISSN: 0969-8043. DOI: <https://doi.org/10.1016/j.apradiso.2025.112002>. URL: <https://www.sciencedirect.com/science/article/pii/S0969804325003471>.
 - [90] Daiyuan Chen and Massimo Giuseppe Martello. “The IRIS fancy GUI”. In: *Hands-on Workshop on IRIS Control Software*. Talk presented at the meeting. Oct. 17, 2025. URL: <https://agenda.infn.it/event/48323/#3-the-iris-fancy-gui> (visited on 09/26/2025).

- [91] Alberto Arzenton. “Radiobiological model for β -emitter radiopharmaceutical therapy in dynamic cell cultures in the framework of the ISOLPHARM project”. In: *Il Nuovo Cimento C* 46.3 (June 2023), pp. 1–10. ISSN: 03905551, 03905551. DOI: 10.1393/ncc/i2023-23072-3. URL: <https://doi.org/10.1393/ncc/i2023-23072-3>.
- [92] Guillem Pratx et al. “Radioluminescence Microscopy: Measuring the Heterogeneous Uptake of Radiotracers in Single Living Cells”. In: *PLOS ONE* 7.10 (Oct. 2012), pp. 1–9. DOI: 10.1371/journal.pone.0046285. URL: <https://doi.org/10.1371/journal.pone.0046285>.
- [93] Nicole Barthe et al. “Chapter 9 - High-resolution beta imaging”. In: *Handbook of Radioactivity Analysis: Volume 2 (Fourth Edition)*. Ed. by Michael F. L’Annunziata. Fourth Edition. Academic Press, 2020, pp. 669–727. ISBN: 978-0-12-814395-7. DOI: <https://doi.org/10.1016/B978-0-12-814395-7.00009-X>. URL: <https://www.sciencedirect.com/science/article/pii/B978012814395700009X>.
- [94] Alberto Arzenton. “Towards Ag-111 as a medical radionuclide: from production and laser photo-ionisation to cell dosimetry and radiation biophysics in the context of the ISOLPHARM project”. PhD thesis. Università degli Studi di Siena, 2024. DOI: 10.25434/arzenton-alberto_phd2024-11-11. URL: <https://hdl.handle.net/11365/1277135>.
- [95] B Abelev et al and (The ALICE Collaboration). “Technical Design Report for the Upgrade of the ALICE Inner Tracking System”. In: *Journal of Physics G: Nuclear and Particle Physics* 41.8 (July 2014), p. 087002. DOI: 10.1088/0954-3899/41/8/087002. URL: <https://dx.doi.org/10.1088/0954-3899/41/8/087002>.
- [96] M. Mager. “ALPIDE, the Monolithic Active Pixel Sensor for the ALICE ITS upgrade”. In: *Nuclear Instruments and Methods in Physics Research Section A: Accelerators, Spectrometers, Detectors and Associated Equipment* 824 (2016). Frontier Detectors for Frontier Physics: Proceedings of the 13th Pisa Meeting on Advanced Detectors, pp. 434–438. ISSN: 0168-9002. DOI: <https://doi.org/10.1016/j.nima.2015.09.057>. URL: <https://www.sciencedirect.com/science/article/pii/S0168900215011122>.
- [97] Alessandro Ferretti. “ALICE upgrades for Run 4 and Run 5”. In: *Nuclear and Particle Physics Proceedings* 324-329 (2023). QCD 22 is the 25th International Conference on Quantum Chromodynamics, pp. 26–29. ISSN: 2405-6014. DOI: <https://doi.org/10.1016/j.nu>

- clphysbps.2023.01.028. URL: <https://www.sciencedirect.com/science/article/pii/S2405601423000354>.
- [98] M. Mager. “ALPIDE, the Monolithic Active Pixel Sensor for the ALICE ITS upgrade”. In: *Nuclear Instruments and Methods in Physics Research Section A: Accelerators, Spectrometers, Detectors and Associated Equipment* 824 (2016). Frontier Detectors for Frontier Physics: Proceedings of the 13th Pisa Meeting on Advanced Detectors, pp. 434–438. ISSN: 0168-9002. DOI: <https://doi.org/10.1016/j.nima.2015.09.057>. URL: <https://www.sciencedirect.com/science/article/pii/S0168900215011122>.
- [99] Monika Varga-Kofarago. “Medical Applications of the ALPIDE Detector”. In: *Universe* 5.5 (2019). ISSN: 2218-1997. DOI: [10.3390/universe5050128](https://doi.org/10.3390/universe5050128). URL: <https://www.mdpi.com/2218-1997/5/5/128>.
- [100] F. Colamaria et al. “Study of the photon rejection of the ALPIDE pixel detector for medical applications”. In: *2019 IEEE 8th International Workshop on Advances in Sensors and Interfaces (IWASI)*. IEEE, June 2019, pp. 1–6. DOI: [10.1109/iwasi.2019.8791306](https://doi.org/10.1109/iwasi.2019.8791306). URL: <http://dx.doi.org/10.1109/IWASI.2019.8791306>.
- [101] M. Aehle et al. “The Bergen proton CT system”. In: *Journal of Instrumentation* 18.02 (Feb. 2023), p. C02051. DOI: [10.1088/1748-0221/18/02/C02051](https://doi.org/10.1088/1748-0221/18/02/C02051). URL: <https://dx.doi.org/10.1088/1748-0221/18/02/C02051>.
- [102] *iMPACT*. URL: <https://web.infn.it/GRIT/impact/> (visited on 01/12/2025).
- [103] Filippo Baruffaldi. “Studies for a proton tomography scanner”. MA thesis. Università degli Studi di Padova, 2018. URL: <https://hdl.handle.net/20.500.12608/25104>.
- [104] Gabriele Bortolato. “Sviluppo del firmware per il controllo del detector ALPIDE ed implementazione su FPGA”. Bachelor thesis. Università degli Studi di Padova, 2020. URL: <https://hdl.handle.net/20.500.12608/22415> (visited on 03/02/2025).
- [105] ALICE ITS ALPIDE development team. *ALPIDE Operations Manual*. Tech. rep. CERN, 2017. URL: <https://edms.cern.ch/document/1773020/1> (visited on 03/02/2025).
- [106] Chris Liechti. *pySerial: Python Serial Port Extension*. Versione X.Y. 2001. URL: <https://pyserial.readthedocs.io/>.
- [107] *festo-edcon*. 2025. URL: <https://festo-research.gitlab.io/electric-automation/festo-edcon/> (visited on 09/02/2025).

- [108] Vittoria Pavanello. “Performance study of a novel 2D imaging beta detector for medical applications”. MA thesis. Università degli Studi di Padova, 2023. URL: <https://hdl.handle.net/20.500.12608/51901>.
- [109] *DUMBO*. 2025. URL: <https://github.com/dserafini/DUMBO> (visited on 09/02/2025).
- [110] Cesare Gabriele Gaglio et al. “GelMA synthesis and sources comparison for 3D multimaterial bioprinting”. In: *Frontiers in Bioengineering and Biotechnology* Volume 12 - 2024 (2024). ISSN: 2296-4185. DOI: 10.3389/fbioe.2024.1383010. URL: <https://www.frontiersin.org/journals/bioengineering-and-biotechnology/articles/10.3389/fbioe.2024.1383010>.
- [111] *μ -Slide 1 Well*. 2025. URL: <https://ibidi.com/chambered-coverslips/314--slide-1-well.html> (visited on 09/05/2025).
- [112] Stephen Seltzer. *Stopping-Powers and Range Tables for Electrons, Protons, and Helium Ions, NIST Standard Reference Database 124*. en. 2017. DOI: 10.18434/T4NC7P. URL: <http://www.nist.gov/pml/data/star/index.cfm>.
- [113] Sofia Busatto. “Simulazione dei campioni di idrogel biologico caricati con Ag-111 e prime caratterizzazioni sperimentali con il beta detector DUMBO”. Bachelor’s Thesis. Università degli Studi di Padova, 2025.
- [114] S. Beol   et al. “The MAPS foil”. In: *Nuclear Instruments and Methods in Physics Research Section A: Accelerators, Spectrometers, Detectors and Associated Equipment* 1046 (2023), p. 167673. ISSN: 0168-9002. DOI: <https://doi.org/10.1016/j.nima.2022.167673>. URL: <https://www.sciencedirect.com/science/article/pii/S0168900222009652>.
- [115] Yassine Bouchareb et al. “Technological Advances in SPECT and SPECT/CT Imaging”. In: *Diagnostics* 14.13 (2024). ISSN: 2075-4418. DOI: 10.3390/diagnostics14131431. URL: <https://www.mdpi.com/2075-4418/14/13/1431>.
- [116] S Yandrapalli and Y Puckett. “SPECT Imaging”. In: *StatPearls [Internet]*. [Updated 2022 Oct 3]. Treasure Island (FL): StatPearls Publishing, Jan. 2025. URL: <https://www.ncbi.nlm.nih.gov/books/NBK564426/>.
- [117] *Clinical Applications of SPECT-CT*. Springer International Publishing, 2022. ISBN: 9783030658502. DOI: 10.1007/978-3-030-65850-2. URL: <http://dx.doi.org/10.1007/978-3-030-65850-2>.

- [118] George Crişan et al. “Radiopharmaceuticals for PET and SPECT Imaging: A Literature Review over the Last Decade”. In: *International Journal of Molecular Sciences* 23.9 (2022). ISSN: 1422-0067. DOI: 10.3390/ijms23095023. URL: <https://www.mdpi.com/1422-0067/23/9/5023>.
- [119] D. Serafini et al. *Monte Carlo simulation of the ISOLPHARM gamma camera for Ag-111 imaging*. 2025. arXiv: 2502.20112. URL: <https://arxiv.org/abs/2502.20112>.
- [120] Matteo Negrini et al. “The ISOLPHARM gamma-camera for Ag-111”. to be submitted in 2025.
- [121] Hamamatsu Photonics K.K. *MPPC (Multi-Pixel Photon Counter) S14160/S14161 series — Technical Datasheet*. https://www.hamamatsu.com/content/dam/hamamatsu-photonics/sites/documents/99_SALES_LIBRARY/ssd/s14160_s14161_series_kapd1064e.pdf. Cat. No. KAPD1064E04; Information current as of November 2024. Nov. 2024.
- [122] <https://github.com/dserafini/gamma-camera>. URL: <https://github.com/dserafini/gamma-camera> (visited on 02/16/2025).
- [123] Nagomi Uchida et al. “Attenuation characteristics of a Ce: Gd₃ Al₂ Ga₃ O₁₂ scintillator”. In: *Nuclear Instruments and Methods in Physics Research Section A: Accelerators, Spectrometers, Detectors and Associated Equipment* 986 (2021), p. 164725. ISSN: 0168-9002. DOI: <https://doi.org/10.1016/j.nima.2020.164725>. URL: <https://www.sciencedirect.com/science/article/pii/S0168900220311220>.
- [124] Gregorio Landi. “Properties of the center of gravity as an algorithm for position measurements”. In: *Nuclear Instruments and Methods in Physics Research Section A: Accelerators, Spectrometers, Detectors and Associated Equipment* 485.3 (2002), pp. 698–719. ISSN: 0168-9002. DOI: [https://doi.org/10.1016/S0168-9002\(01\)02071-X](https://doi.org/10.1016/S0168-9002(01)02071-X). URL: <https://www.sciencedirect.com/science/article/pii/S016890020102071X>.
- [125] H. Wiecezorek and A. Goedicke. “Analytical model for SPECT detector concepts”. In: *IEEE Transactions on Nuclear Science* 53.3 (June 2006), pp. 1102–1112. ISSN: 0018-9499. DOI: 10.1109/tns.2006.874954. URL: <http://dx.doi.org/10.1109/TNS.2006.874954>.
- [126] M.J. Berger et al. 2010. DOI: 10.18434/T48G6X. URL: <https://dx.doi.org/10.18434/T48G6X> (visited on 05/04/2025).

- [127] *MOBY/ROBY Phantoms*. <https://cvit.duke.edu/resource/moby-roby-phantoms/>. Center for Virtual Imaging Trials (CVIT), Duke University. Accessed: 2025-09-29. 2025.
- [128] William Segars and Benjamin Tsui. “4D MOBY and NCAT phantoms for medical imaging simulation of mice and men”. In: *Journal of Nuclear Medicine* 48.supplement 2 (2007), 203P–203P. ISSN: 0161-5505. eprint: <https://jnm.snmjournals.org/content>. URL: http://jnm.snmjournals.org/content/48/supplement_2/203P.4.
- [129] William.P. Segars et al. “Development of a 4-D digital mouse phantom for molecular imaging research”. In: *Molecular Imaging & Biology* 6.3 (2004), pp. 149–159. ISSN: 1536-1632. DOI: <https://doi.org/10.1016/j.mibio.2004.03.002>. URL: <https://www.sciencedirect.com/science/article/pii/S1536163204002173>.
- [130] Belma Dogdas et al. “Digimouse: a 3D whole body mouse atlas from CT and cryosection data”. In: *Physics in Medicine & Biology* 52.3 (Jan. 2007), p. 577. DOI: 10.1088/0031-9155/52/3/003. URL: <https://dx.doi.org/10.1088/0031-9155/52/3/003>.
- [131] M.R. Mititelu et al. “Overview of Adverse Reactions of Radiopharmaceuticals”. In: *Clinical Oncology* 43 (2025), p. 103857. ISSN: 0936-6555. DOI: <https://doi.org/10.1016/j.clon.2025.103857>. URL: <http://www.sciencedirect.com/science/article/pii/S0936655525001128>.
- [132] Davide Serafini et al. “ ^{111}Ag phantom images with Cerenkov Luminescence Imaging and digital autoradiography within the ISOLPHARM project”. In: *Applied Radiation and Isotopes* 215 (2025), p. 111562. ISSN: 0969-8043. DOI: <https://doi.org/10.1016/j.apradiso.2024.111562>. URL: <https://www.sciencedirect.com/science/article/pii/S0969804324003907>.
- [133] Nikunj B. Bhatt et al. “Practical Guidelines for Cerenkov Luminescence Imaging with Clinically Relevant Isotopes”. In: *Reporter Gene Imaging*. Springer New York, 2018. Chap. 15, pp. 197–208. ISBN: 9781493978601. DOI: 10.1007/978-1-4939-7860-1_15. URL: http://dx.doi.org/10.1007/978-1-4939-7860-1_15.
- [134] Benedict Mc Larney, Magdalena Skubal, and Jan Grimm. “A Review of Recent and Emerging Approaches for the Clinical Application of Cerenkov Luminescence Imaging”. In: *Frontiers in Physics* 9 (2021). ISSN: 2296-424X. DOI: 10.3389/fphy.2021.684196. URL: <https://www.frontiersin.org/articles/10.3389/fphy.2021.684196>.

- [135] R Robertson et al. “Optical imaging of Cerenkov light generation from positron-emitting radiotracers”. In: *Physics in Medicine & Biology* 54.16 (July 2009), N355. DOI: 10.1088/0031-9155/54/16/N01. URL: <https://dx.doi.org/10.1088/0031-9155/54/16/N01>.
- [136] Alessandro Ruggiero et al. “Cerenkov Luminescence Imaging of Medical Isotopes”. In: *Journal of Nuclear Medicine* 51.7 (2010), pp. 1123–1130. ISSN: 0161-5505. DOI: 10.2967/jnumed.110.076521. eprint: <https://jnm.snmjournals.org/content/51/7/1123.full.pdf>. URL: <https://jnm.snmjournals.org/content/51/7/1123>.
- [137] Eric G. Solon. “Autoradiography techniques and quantification of drug distribution”. In: *Cell and Tissue Research* 360.1 (Apr. 2015), pp. 87–107. ISSN: 1432-0878. DOI: 10.1007/s00441-014-2093-4. URL: <https://doi.org/10.1007/s00441-014-2093-4>.
- [138] Brian W. Miller. “Radiation Imagers for Quantitative, Single-particle Digital Autoradiography of Alpha- and Beta-particle Emitters”. In: *Seminars in Nuclear Medicine* 48.4 (July 2018), pp. 367–376. ISSN: 0001-2998. DOI: 10.1053/j.semnuclmed.2018.02.008. URL: <http://dx.doi.org/10.1053/j.semnuclmed.2018.02.008>.
- [139] Viviana Benfante et al. “An Overview of In Vitro Assays of ^{64}Cu -, ^{68}Ga -, ^{125}I -, and $^{99\text{m}}\text{Tc}$ -Labelled Radiopharmaceuticals Using Radiometric Counters in the Era of Radiotheranostics”. In: *Diagnostics* 13.7 (2023). ISSN: 2075-4418. DOI: 10.3390/diagnostics13071210. URL: <https://www.mdpi.com/2075-4418/13/7/1210>.
- [140] Marianna Tosato et al. “Chromatographic separation of silver-111 from neutron-irradiated palladium target: toward direct labeling of radiotracers”. In: *EJNMMI Radiopharmacy and Chemistry* 8.1 (Dec. 2023). ISSN: 2365-421X. DOI: 10.1186/s41181-023-00232-0. URL: <http://dx.doi.org/10.1186/s41181-023-00232-0>.
- [141] Okko Alitalo, Tomi Rantamäki, and Tuulia Huhtala. “Digital autoradiography for efficient functional imaging without anesthesia in experimental animals: Reversing phencyclidine-induced functional alterations using clozapine”. In: *Progress in Neuro-Psychopharmacology and Biological Psychiatry* 100 (June 2020), p. 109887. ISSN: 0278-5846. DOI: 10.1016/j.pnpbp.2020.109887. URL: <http://dx.doi.org/10.1016/j.pnpbp.2020.109887>.
- [142] Douglas L. Vizard et al. *Electronic imaging system for autoradiography*. U.S. pat. Feb. 12, 2002. URL: <https://patents.google.com/patent/US6346707B1/en> (visited on 03/12/2024).

- [143] Ronald J. Jaszczak. *Nuclear imaging phantom*. U.S. pat. Feb. 12, 1985. URL: <https://patents.google.com/patent/US4499375A/en> (visited on 11/27/2023).
- [144] Cristiano L. Fontana et al. “A distributed data acquisition system for nuclear detectors”. In: *International Journal of Modern Physics: Conference Series* 48 (Jan. 2018), p. 1860118. ISSN: 2010-1945. DOI: 10.1142/s2010194518601187. URL: <http://dx.doi.org/10.1142/S2010194518601187>.
- [145] Luca Morselli. *G4LBC*. URL: <https://github.com/lucamors/G4LBC> (visited on 04/09/2025).
- [146] Nicola Zancopè. “Analysis and interpretation of CLI and DRI images in view of a Ag-111 biodistribution experiment”. MA thesis. Università degli Studi di Padova, 2023. URL: <https://hdl.handle.net/20.500.12608/51912>.
- [147] Esther Ciarrocchi and Nicola Belcari. “Cerenkov luminescence imaging: physics principles and potential applications in biomedical sciences”. In: *EJNMMI Physics* 4.1 (Mar. 2017). ISSN: 2197-7364. DOI: 10.1186/s40658-017-0181-8. URL: <http://dx.doi.org/10.1186/s40658-017-0181-8>.
- [148] Martin Ester et al. “A density-based algorithm for discovering clusters in large spatial databases with noise”. In: *Proceedings of the Second International Conference on Knowledge Discovery and Data Mining*. KDD’96. Portland, Oregon: AAAI Press, Aug. 2, 1996, pp. 226–231. (Visited on 11/27/2023).
- [149] Stephen Seltzer. *Stopping-Powers and Range Tables for Electrons, Protons, and Helium Ions, NIST Standard Reference Database 124*. en. 1993. DOI: 10.18434/T4NC7P. URL: <http://www.nist.gov/pml/data/star/index.cfm>.
- [150] European Medicines Agency. *Regulatory acceptance of 3R (replacement, reduction, refinement) testing approaches - Scientific guideline*. URL: <https://www.ema.europa.eu/en/regulatory-acceptance-3r-replacement-reduction-refinement-testing-approaches-scientific-guideline> (visited on 01/03/2025).
- [151] Alberto Arzenton et al. “Benchmark of a biophysical model for the radiobiology of RNT with 125I-labelled agents”. In: *The European Physical Journal Special Topics* (July 2025). ISSN: 1951-6401. DOI: 10.1140/epjs/s11734-025-01752-3. URL: <https://doi.org/10.1140/epjs/s11734-025-01752-3>.

- [152] Lukas M. Carter and Pat B. Zanzonico. “MIB Guides: Preclinical Radiopharmaceutical Dosimetry”. In: *Molecular Imaging and Biology* 26.1 (Feb. 2024), pp. 17–28. ISSN: 1860-2002. DOI: 10.1007/s11307-023-01868-9. URL: <https://doi.org/10.1007/s11307-023-01868-9>.
- [153] A. Volpe, S. Lyashchenko, and V. Ponomarev. “Nuclear-Based Labeling of Cellular Immunotherapies: A Simple Protocol for Preclinical Use”. In: *Molecular Imaging and Biology* 26.4 (July 2024), pp. 555–568. ISSN: 1860-2002. DOI: 10.1007/s11307-024-01923-z. URL: <http://dx.doi.org/10.1007/s11307-024-01923-z>.
- [154] F. Peter Guengerich. “Mechanisms of Drug Toxicity and Relevance to Pharmaceutical Development”. In: *Drug Metabolism and Pharmacokinetics* 26.1 (2011), pp. 3–14. ISSN: 1347-4367. DOI: <https://doi.org/10.2133/dmpk.DMPK-10-RV-062>. URL: <https://www.sciencedirect.com/science/article/pii/S1347436715305449>.

Appendix A

Radioactivity for nuclear medicine

A.1 Radionuclide

The term *nuclide* was introduced in 1947 to identify a species of atom according to the number of protons and neutrons in its nucleus [1]. In the following years, the importance gained by some radionuclides, such as technetium-99m in nuclear medicine, determine the update of the definition. In modern times, a nuclide is a species of atom characterised by its mass number, atomic number and nuclear energy state [2]. A radioactive nuclide is called *radionuclide* [3]. Differently, the term *isotope* indicate nuclides having the same atomic number but different mass numbers. A radioactive isotope of a specified element is named *radioisotope*. The meaning behind each term is different and they should not be used inappropriately [4]. For completeness, *isobar* is one of several nuclides having the same number of nucleons in their nuclei.

Radionuclides decay according to the following equation:

$$\frac{dN}{dt} = -\lambda N \quad (\text{A.1})$$

where λ is the decay width. At time t a number $N(t)$ of nuclei is still present and a number $dN(t)$ has decayed in the time interval $[t, t + dt]$. Then, supposing a initial number N_0 of nuclei at the start ($t = 0$), the number of nuclei as a function of time t is:

$$N(t) = N_0 e^{-\lambda t} \quad (\text{A.2})$$

The inverse of the decay width is called mean life: $\tau = 1/\lambda$. The half-life, that is the time in which half of the original sample of radionuclides is present, is given by $T_{1/2} = \tau \ln 2$.

The *absorbed dose* is the energy absorbed per unit mass (of any material)[5]

$$D = \frac{d\langle E \rangle}{dm} \quad (\text{A.3})$$

where $\langle E \rangle$ is the mean energy imparted by ionising radiation to the matter contained in a volume element of mass dm . The units for this quantity are energy per mass, typically the Gray is adopted

$$1 \text{ Gy} = \frac{1 \text{ J}}{1 \text{ kg}} \quad (\text{A.4})$$

A.2 Effective disappearance half-life

Many materials are cleared from the body through biological or physiological processes, with a trend that can be modelled as an exponential decay function. The amount of a non-radioactive substance in the body at time t is [5]

$$X(t) = X_0 e^{-\lambda_b t} \quad (\text{A.5})$$

where X_0 is the initial amount and λ_b is the biological disappearance constant. Similarly to the radioactivity case, the biological half-life for removal is the time in which half of the remaining material is removed by biological processes. For a radioactive substance, the decay constant can be summed to give the effective disappearance constant

$$\lambda_e = \lambda_b + \lambda_p \quad (\text{A.6})$$

where λ_p indicates the physical decay constant (previously indicated with λ only).

Radionuclides with long half-lives are not used in nuclear medicine because they deliver the majority of the dose outside the window for imaging or therapy. Figure A.1 compares the dose in the therapy window for radionuclides with different half-lives. The contribution from biological clearance is considered so the effective half-lives are represented.

A.3 Decay chain

For the production of medical radionuclides, the decay chain of between radionuclides must be considered. Consider the following decay chain until

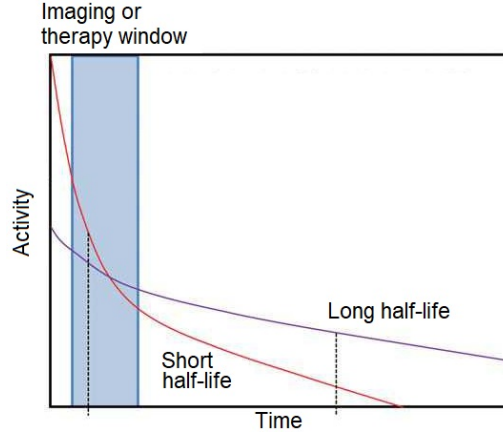


Figure A.1: Schematic representation of the patient dose as a function of time for radionuclides with different half-lives. Adapted from [4].

the stable substance k :

$$N_1 \xrightarrow{\lambda_1} N_2 \xrightarrow{\lambda_2} N_3 \xrightarrow{\lambda_3} \dots \xrightarrow{\lambda_{k-1}} N_k \quad (\text{A.7})$$

The differential equation that describes the number of nuclei of a species is

$$\frac{dN_i}{dt} = \lambda_{i-1}N_{i-1} - \lambda_i N_i \quad (\text{A.8})$$

where $i \neq 1$. The solutions for this differential equation are represented by the Bateman equations.

Suppose to have only two radioactive species in the chain. If the decay constant of the parent is much smaller than the daughter, $\lambda_1 \ll \lambda_2$, the number of nuclei as a function of time is [6]

$$\begin{aligned} A_1(t) &\approx \lambda_1 N_1(0) \\ A_2(t) &= N_1(0)\lambda_1(1 - e^{-\lambda_2 t}) \xrightarrow{t \rightarrow \infty} N_1(0)\lambda_1 \end{aligned} \quad (\text{A.9})$$

This is a secular equilibrium case because the production rate of the daughter nucleus is equal to its decay rate.

A.4 Radionuclide sample properties

In the guidelines of the International Atomic Energy Agency (IAEA) regarding the quality control in the production of radiopharmaceuticals, there are the definitions for the following terms that will be used later [7]:

Specific activity The activity of the radionuclide per mass of the radionuclide or other isotopes of the same element present in a sample. The unit of measurement is [Bq/g].

Radionuclidic purity The proportion of the activity of the radionuclide concerned to the total radioactivity of the radiopharmaceutical. The unit of measurement is [%].

In general, radiopharmaceuticals aim to maximise both the specific activity and the radionuclidic purity.

References

- [1] Truman P. Kohman. “Proposed New Word: Nuclide”. In: *American Journal of Physics* 15.4 (July 1947), pp. 356–357. ISSN: 0002-9505. DOI: 10.1119/1.1990965. eprint: https://pubs.aip.org/aapt/ajp/article-pdf/15/4/356/12064518/356_2_online.pdf. URL: <https://doi.org/10.1119/1.1990965>.
- [2] “nuclide”. In: (2025). DOI: doi:10.1351/goldbook.N04257. URL: <https://doi.org/10.1351/goldbook.N04257>.
- [3] “radionuclide”. In: (2025). DOI: doi:10.1351/goldbook.R05116. URL: <https://doi.org/10.1351/goldbook.R05116>.
- [4] GM Currie et al. “Radionuclide production”. In: *Radiographer* 58.3 (2011), pp. 46–52. DOI: <https://doi.org/10.1002/j.2051-3909.2011.tb00155.x>. eprint: <https://onlinelibrary.wiley.com/doi/pdf/10.1002/j.2051-3909.2011.tb00155.x>. URL: <https://onlinelibrary.wiley.com/doi/abs/10.1002/j.2051-3909.2011.tb00155.x>.
- [5] Michael G. Stabin. *Fundamentals of Nuclear Medicine Dosimetry*. 1st ed. eBook ISBN 978-0-387-74579-4, Softcover ISBN 978-0-387-74578-7. New York, NY: Springer New York, 2008, pp. VII, 237. ISBN: 978-0-387-74578-7. DOI: 10.1007/978-0-387-74579-4. URL: <https://doi.org/10.1007/978-0-387-74579-4>.
- [6] Marco Mazzocco. *Phenomenology of Radioactive Decays*. Slide del corso. 2021.

- [7] *Quality Control in the Production of Radiopharmaceuticals*. TECDOC Series 1856. Vienna: International Atomic Energy Agency, 2018. ISBN: 978-92-0-107918-3. URL: <https://www.iaea.org/publications/13422/quality-control-in-the-production-of-radiopharmaceuticals>.

Appendix B

Kromek CZT detector calibration for activity estimation of medical radionuclides at MEDICIS

This appendix reports the activity carried out at CERN-MEDICIS. The same content, with minor differences, is also available online [1].

B.1 Introduction

Targeted Radionuclide Therapy (TRT) is a clinical technique used to treat cancer. MEDICIS (MEDical Isotopes Collected from ISolde) is a facility at CERN dedicated to the production of radionuclides of medical interest (such as those employed in TRT drugs) for use in research centres and hospitals. These radionuclides are typically produced by irradiating a target at the nearby ISOLDE facility with a high-energy proton beam (1.4 GeV). During irradiation, several types of nuclear reactions occur, generating a wide variety of radionuclides within the target. After irradiation, the target unit is transferred from ISOLDE to the MEDICIS front-end. These units are compatible with both facilities and consist of an aluminium, water-cooled vacuum vessel. Inside the vessel, a tubular tantalum oven contains the irradiated target material. The target unit is heated to high temperatures (often exceeding 2000 °C) to promote the diffusion and effusion of the nuclides of interest. The effused nuclides then pass through an ion source, where they are ionised. The resulting ions are accelerated by a 60 kV potential difference between the ion source and the extraction electrode, forming

Nuclide	$T_{1/2}$	Reference activity		Measurement activity	
		\mathcal{A} (kBq)	Date	\mathcal{A} (kBq)	Date
^{152}Eu	13.517 y	1966	01/01/2024	1916	21/06/2024
^{133}Ba	10.551 y	478.98	02/11/2023	458.46	01/07/2024
^{60}Co	5.28 y	124.26	08/01/2024	116.46	04/07/2024
^{43}K	22.3 h	-	-	-	-

Table B.1: Radioactive sources used for the detector calibration and test.

a Radioactive Ion Beam (RIB). A dipole magnet is subsequently used to select the desired nuclide, which can be implanted onto thin metallic (Al or Zn) or NaCl-coated foils for dispatch to biomedical laboratories for further investigation [2].

A gamma-ray detector is used to monitor the activity during the collection process. In particular, by knowing the rate at which collection occurs, the operator can adjust the operation parameters in the front-end control software. A second gamma-ray detector is positioned further away from the collection point to extend the dynamic range of the measureable activity. For this more distant location, a different model was chosen. This model features a smaller crystal volume, which reduces the detector efficiency and thereby increases the maximum activity that can be measured. The aim of this internship is to characterise this detector and to compare its performance with the detectors already installed.

B.2 Materials and Methods

The gamma-ray detector used in this study is a Kromek GR05. This model contains a CZT (Cadmium Zinc Telluride) crystal cube of 0.5 cm side (faces of 0.25 cm² and volume of 0.125 cm³) [3]. This crystal is a semiconductor that can operate at room temperature. To be ready for acquisition, simply one USB cable needs to be connected from the detector to the data-acquiring PC. The detectors already installed in front and below the collection chamber are Kromek GR1, that are characterised by a crystal with two times the GR05 side: faces of 1 cm² and volume of 1 cm³. At present, acquisitions with these Kromek detectors can only be performed with Kromek MultiSpect software [4].

An offline setup was built to characterise the detectors before the online installation. Figure B.1 shows such setup: there is the sample holder where the sealed source is positioned, then the flange separating the detector from

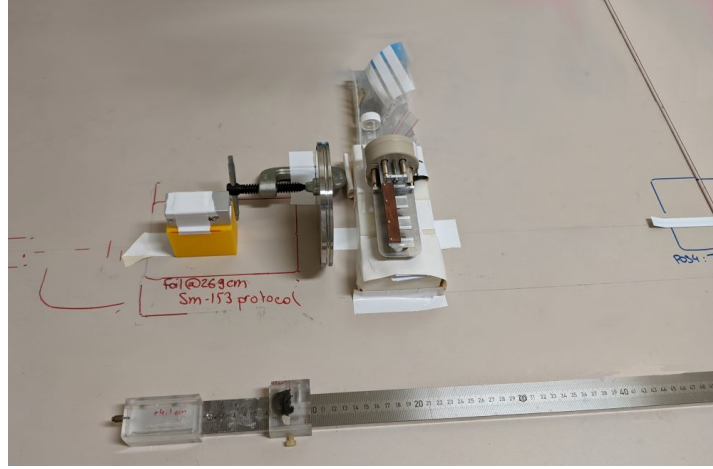


Figure B.1: Offline setup for detector characterisation.

Radionuclide	Energy (keV)	Intensity Γ (%)	σ_{Γ} (%)
^{152}Eu	121.7817	28.53	0.16
	244.6974	7.55	0.04
	344.2785	26.59	0.20
	411.1165	2.237	0.013
	443.9606	2.827	0.014
	778.9045	12.93	0.08
	867.38	4.23	0.03
	964.057	14.51	0.07
	1408.013	20.87	0.09
^{133}Ba	276.3989	7.16	0.05
	302.8508	18.34	0.13
	356.0129	62.05	0.00
	383.8485	8.94	0.06
^{60}Co	1173.228	99.85	0.03
	1332.492	99.9826	0.0006
^{43}K	220.632	4.80	0.06
	372.760	86.80	-
	593.390	11.26	0.08
	617.490	79.2	0.6
	1021.698	1.96	0.03

Table B.2: Gamma lines of interest for the measured sources. Data are retrieved from the NNDC [5].

the collection chamber and finally the detector itself. The characteristics (half-life, reference activity, activity at the start of the acquisition) of the radioactive sources that are used in this activity are reported in Table B.1. Furthermore, The gamma lines of interest are described in Table B.2, indicating their energy, intensity (Γ) and the uncertainty associated to the intensity. Since radionuclides of medical interest typically emit gamma-rays with low energy ($\lesssim 300$ keV), it is important to get as much calibration points as possible in this region.

Finally, the calibration curve was tested measuring a foil where ^{43}K has been implanted. The features of this source are reported again in Tables B.1 and B.2. The procedure to characterise this type of detectors is described in Patrīcija Kalniņa's master thesis [6]. For the sake of clarity it will be described again in this section.

Energy calibration

The first step is to determine which energy corresponds to each channel in the energy spectra. Energy calibration is carried out comparing the full-energy peaks in the raw energy spectra (in bins) with the ones recorded in the online database. The pairs of points are then fitted with a first grade polynomial:

$$\text{energy [keV]} = c_0 [\text{keV}] + c_1 [\text{keV/ch}] \cdot \text{energy [ch]} \quad (\text{B.1})$$

or a second grade polynomial:

$$\begin{aligned} \text{energy [keV]} = & c_0 [\text{keV}] + c_1 [\text{keV/ch}] \cdot \text{energy [ch]} + \\ & + c_2 [\text{keV/ch}^2] \cdot (\text{energy [ch]})^2 \end{aligned} \quad (\text{B.2})$$

The results of the energy calibration are described in Section B.3 and in particular in Table B.3.

Efficiency calibration

It is necessary to estimate the detector efficiency to relate the number of recorded pulses to the activity of the source. The *absolute peak efficiency* as a function of energy is defined as [7]:

$$\frac{\text{number of events in the full energy peak}}{\text{number of radiation quanta emitted by source}} \equiv \frac{\mathcal{N}}{N_{\text{tot}}} \quad (\text{B.3})$$

MultiSpect software refers to \mathcal{N} as *net counts*. The formula used to retrieve the source activity is:

$$\text{activity} = \frac{\mathcal{N}}{\Gamma \Delta t \epsilon} \equiv \mathcal{A} \quad (\text{B.4})$$

where Δt is the acquisition time interval, Γ is the branching ratio and ϵ is the efficiency. It should be emphasised that the efficiency is a function of the energy: $\epsilon(E)$. Solving for the efficiency:

$$\epsilon[\text{adim}] = \frac{\mathcal{N}[\text{counts}]}{\Gamma[\text{adim}]\Delta t[s]\mathcal{A}[\text{Bq}]} \quad (\text{B.5})$$

Acquiring the gamma-ray energy spectrum for a calibration source of known activity enables the estimation of the efficiency values at the energies of the available full-energy peaks. The detected counts \mathcal{N} of the full-energy peak of interest are estimated by fitting with a Gaussian curve:

$$G(A, \mu, \sigma; x) = A \cdot \exp\left(\frac{(x - \mu)^2}{2\sigma^2}\right) \quad (\text{B.6})$$

on top of a linear background:

$$P(c_0, c_1; x) = c_0 + c_1 \cdot x \quad (\text{B.7})$$

So that the fitting function is:

$$G(A, \mu, \sigma; x) + P(c_0, c_1; x) \quad (\text{B.8})$$

The estimated number of counts is then given by the area Σ of the Gaussian curve without the background [8]:

$$\mathcal{N} = \Sigma = \sqrt{2\pi} \cdot A \cdot \underbrace{\frac{\sigma}{\Delta_{\text{bin}}}}_{1 \text{ ch}} \quad (\text{B.9})$$

The fit with the function described in Equations (B.6)-(B.8) was performed testing different programs:

- Kromek MultiSpect [4]
 - with automatic procedure
 - with manual ROI definition
- FitzPeaks [9]
- Scipy [10]

In this report only Kromek MultiSpect automatic and Scipy will be discussed. The other two programs behave in a similar way, therefore, for them only the resulting efficiency values are reported in section B.3.

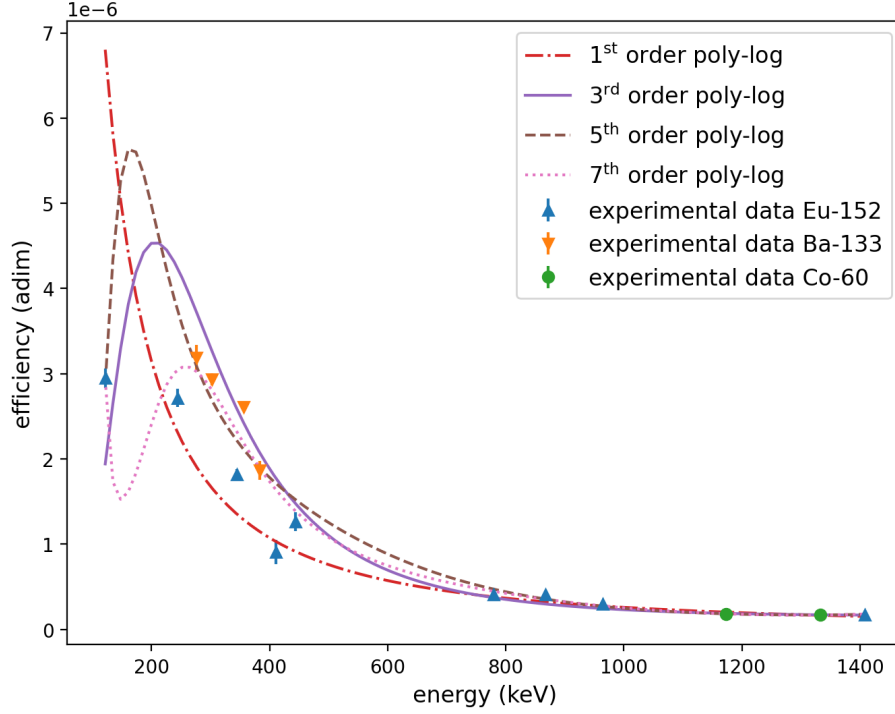


Figure B.2: Plot of the efficiency logarithm values \mathcal{L} fitted with logarithm polynomials of different grades. The solid lane indicates the 3rd order.

The errors are given by the error propagation formula

$$\begin{aligned}\sigma_\epsilon &= \epsilon \sqrt{\left(\frac{\sigma_{\mathcal{N}}}{\mathcal{N}}\right)^2 + \left(\frac{\sigma_{\mathcal{A}}}{\mathcal{A}}\right)^2 + \left(\frac{\sigma_\Gamma}{\Gamma}\right)^2} \\ &= \epsilon \sqrt{\left(\frac{\sigma_A}{A}\right)^2 + \left(\frac{\sigma_\sigma}{\sigma}\right)^2 + \left(\frac{\sigma_{\mathcal{A}}}{\mathcal{A}}\right)^2 + \left(\frac{\sigma_\Gamma}{\Gamma}\right)^2}\end{aligned}\quad (\text{B.10})$$

assuming no error in the acquisition time Δt .

A fit is performed on the natural logarithm of the efficiency values using the following curve:

$$\begin{aligned}\ln \epsilon &= a_0 + a_1 \ln \frac{E}{E_m} + a_2 \left(\ln \frac{E}{E_m} \right)^2 + a_3 \left(\ln \frac{E}{E_m} \right)^3 \\ &\equiv \mathcal{L}(a_0, a_1, a_2, a_3; E)\end{aligned}\quad (\text{B.11})$$

where E_m is a normalisation factor. MultiSpect software uses a polynomial of logarithms as well but with the possibility to consider up to the 7th order. As shown in Figure B.2, higher order terms should be neglected as they

introduce unpredictable oscillations between the experimental data points. The normalisation factor E_m can be chosen to minimise the correlation between the a_i parameters [11]. In this work, $E_m = 250$ keV was adopted.

The efficiency of the detector for the investigated energy range is obtained by taking the exponential of the fitting curve:

$$\epsilon = \exp(\mathcal{L}(E)) \quad (\text{B.12})$$

In order to estimate the corresponding uncertainty, first the variance of the logarithm of the efficiency is estimated:

$$\begin{aligned} \text{Var}(\mathcal{L}) = & \text{Var}(a_0) + (\ln(E/E_m))^2 \text{Var}(a_1) + \\ & + (\ln(E/E_m))^4 \text{Var}(a_2) + (\ln(E/E_m))^6 \text{Var}(a_3) + \\ & + 2(\ln(E/E_m)) \text{Cov}(a_0, a_1) + 2(\ln(E/E_m))^2 \text{Cov}(a_0, a_2) + \\ & + 2(\ln(E/E_m))^3 \text{Cov}(a_0, a_3) + 2(\ln(E/E_m))^3 \text{Cov}(a_1, a_2) + \\ & + 2(\ln(E/E_m))^4 \text{Cov}(a_1, a_3) + 2(\ln(E/E_m))^5 \text{Cov}(a_2, a_3) \end{aligned} \quad (\text{B.13})$$

where $\text{Cov}(a_i, a_j)|_{i \neq j}$ correspond to the off-diagonal elements of the covariance matrix and $\text{Var}(a_i)$ to the diagonal ones. Then the error propagation formula is applied again:

$$\text{Var}(\epsilon) = \epsilon^2 \text{Var}(\mathcal{L}) \quad (\text{B.14})$$

Taking the square root of this variance, the uncertainty of the efficiency in Equation (B.12) is obtained:

$$\sigma_\epsilon = \sqrt{\text{Var}(\epsilon)} = \epsilon \sqrt{\text{Var}(\mathcal{L})} \quad (\text{B.15})$$

From the fitting curve for the detector efficiency a set of artificial data points is generated to be used as input for MultiSpect fitting algorithm. This procedure allows to have a better control during the fit, especially in the low energy region ($\lesssim 300$ keV) where the efficiency curve is steepest. The artificial points are fitted as represented in Figure B.10b. The resulting set of parameters can be saved within the program to be used later for any available energy spectrum. Knowing the efficiency curve for the detector and the radionuclide being measured, Kromek can automatically count the number of events in a full-energy peak of interest to estimate the activity of the source. This procedure, and more in general the estimation of sources activity with Kromek MultiSpect and SciPy, is schematised in Figure B.3. It must be noted that only Kromek MultiSpect is able to analyse in real time the data that are being acquired from the CZT. SciPy and the others

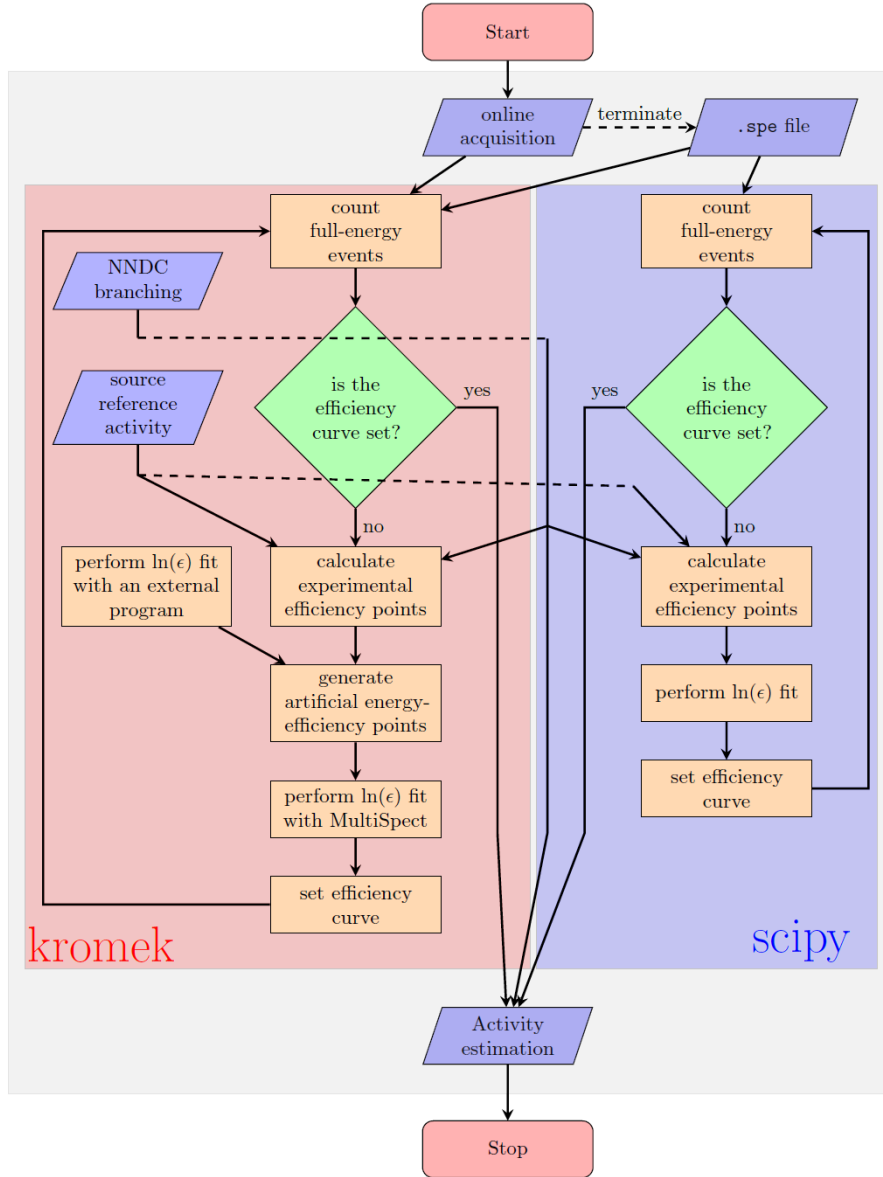


Figure B.3: Diagram illustrating the steps to estimate the activity of a radioactive source with a Kromek CZT detector.

external software can access the data only at the end of the acquisition when the energy spectrum is saved in a `.spe` file.

Describing more in details the approach with SciPy, a module named `optimize` was used. The latter provides a function that can be used to fit a set of data: `curve_fit`. This function needs in input:

- fitting function $\rightarrow \mathcal{L}$ from Equation (B.11)
- set of data points $\rightarrow \{(E_i, \mathcal{L}_i)\}_{i=1, \dots, n}$

Moreover, one can supply also

- set of starting values for the parameters $\rightarrow \{a_0, a_1, a_2, a_3\}$
- uncertainties for the data points $\rightarrow \sigma_{\mathcal{L}, i}$

The fit is performed minimising the square of the residuals by changing the parameters values. Namely, the function being minimised is

$$\chi^2 \equiv \sum_{i=1}^n \frac{(\mathcal{L}(\bar{a}, E_i) - \mathcal{L}_i)^2}{\sigma_{\mathcal{L}, i}^2} \quad (\text{B.16})$$

where $\mathcal{L}(\bar{a}, E_i)$ refers to the values of the function in Equation (B.11) calculated at the energies E_i . The latter identifies the energies for which the experimental values of the efficiency logarithms \mathcal{L}_i were calculated. n is the number of experimental data points. The uncertainties on \mathcal{L}_i determine the weight of the data point during the fit. If these uncertainties are not specified, they are assumed unitary for all the data points. The results for the efficiency calibration are reported in Section B.3.

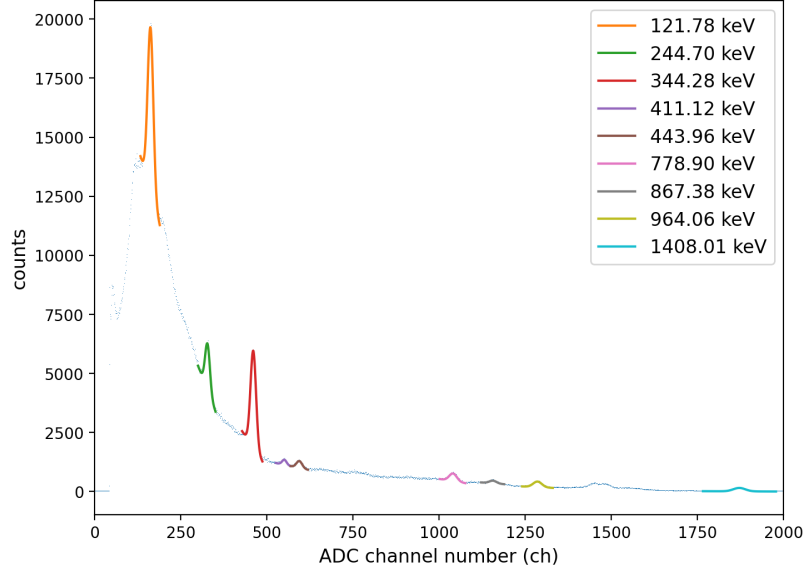


Figure B.4: ^{152}Eu energy spectrum with Gaussian fitting curves superimposed to the main full-energy peaks. A linear background is assumed within the fit range.

Equation	Parameter	value
Linear	c_0 (keV)	$-2.40(52)$
	c_1 (keV/ch)	$0.752\,57(52)$
Quadratic	c_0 (keV)	$0.75(36)$
	c_1 (keV/ch)	$0.7435(9)$
	c_2 (keV/ch ²)	$0.000\,004\,4(4)$

Table B.3: Optimised parameters for the efficiency fit with the functions described in Equation (B.1) and (B.2).

B.3 Results

As an example, the energy spectrum of ^{152}Eu acquired with MultiSpect is represented in Figure B.4. The full-energy peaks are fitted with the function described in Equation (B.8). The energy resolution of the detector is not sufficient to separate the two peaks at 1085 keV and 1112 keV. Therefore these two peaks are not considered in the following analysis.

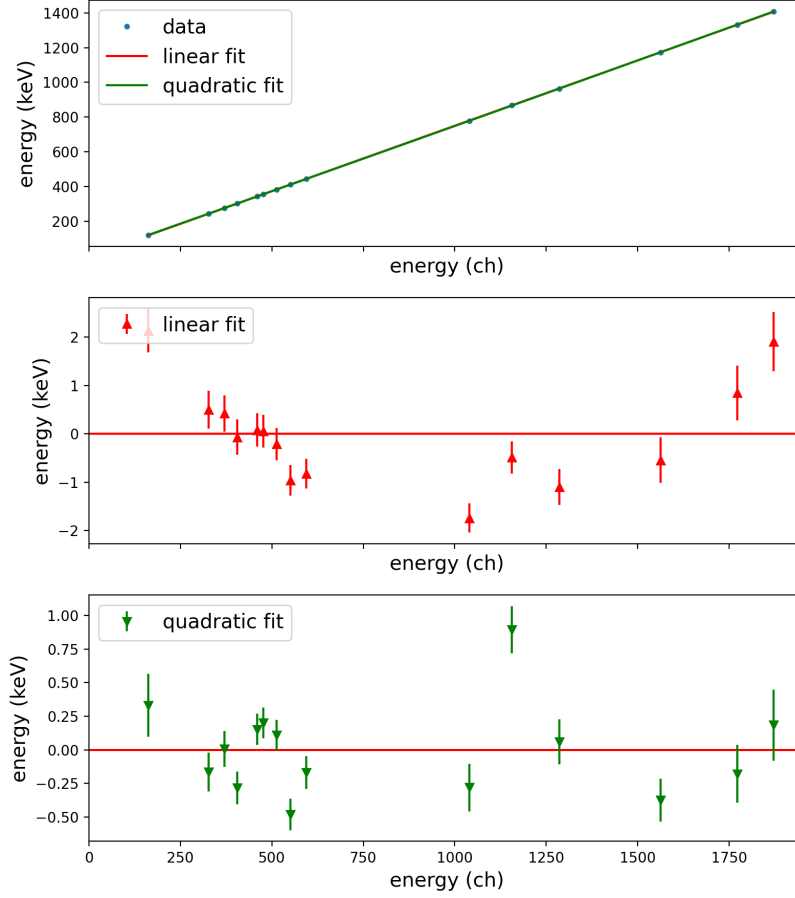


Figure B.5: Energy calibration plot (top) with polynomial fits, the quadratic component is small so linear and quadratic fits overlap. Residuals are shown for both linear (middle) and quadratic (bottom) functions.

Energy calibration

In Figure B.5 the energy calibration fits are presented for both linear and quadratic fits. Looking at the linear fit residuals, a quadratic trend appears. For this reason, another fit with a second-order polynomial was performed, obtaining better residuals. On the other hand, for the scope of this detector, the linear calibration is sufficient to recognise the full-energy peaks of the radionuclides. The optimal parameters for both fits are reported in Table B.3.

The uncertainties of the values on the energy (keV) axis are calculated using the error propagation formula. For the linear formula in Equation (B.1):

$$\sigma_y^2 = \sigma_A^2 + x^2 \sigma_B^2 + 2x \text{Cov}(A, B) \quad (\text{B.17})$$

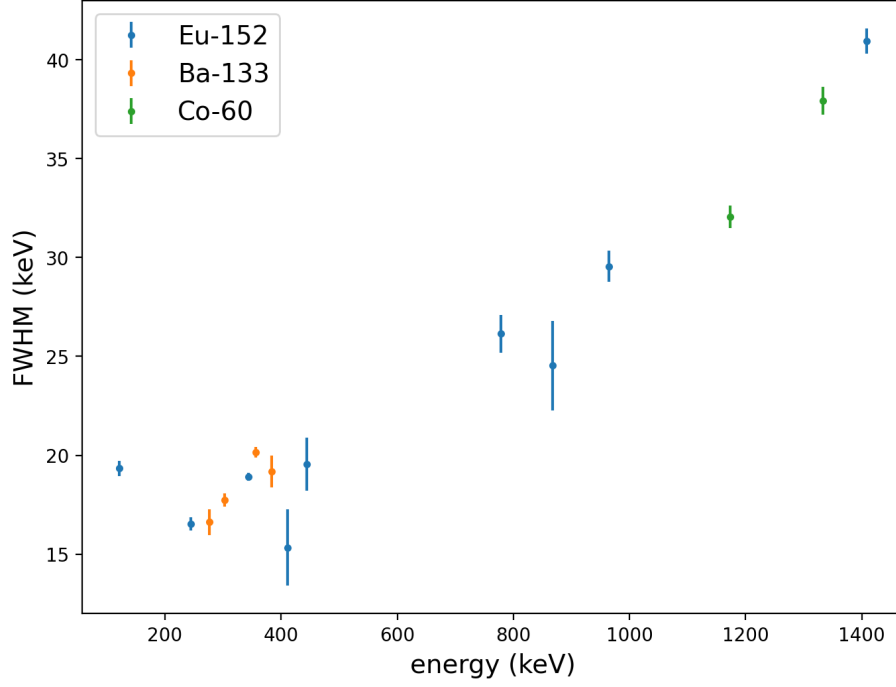


Figure B.6: FWHM estimated for the peaks of ^{152}Eu , ^{133}Ba , ^{60}Co .

and for the quadratic formula in Equation (B.2):

$$\begin{aligned} \sigma_y^2 = & \sigma_A^2 + x^2 \sigma_B^2 + x^4 \sigma_C^2 \\ & + 2x \text{Cov}(A, B) + 2x^2 \text{Cov}(A, C) + 2x^3 \text{Cov}(B, C) \end{aligned} \quad (\text{B.18})$$

where x and y indicate the channel and the energy in keV respectively.

The energy resolution as a function of the energy is plotted in Figure B.6. The point at ~ 121 keV has a value much higher than the trend, this fact could be a consequence of the high background contribution at low energy. Furthermore, the efficiency rapidly decreases toward lower energy values therefore it is possible that the detector energy resolution is affected too.

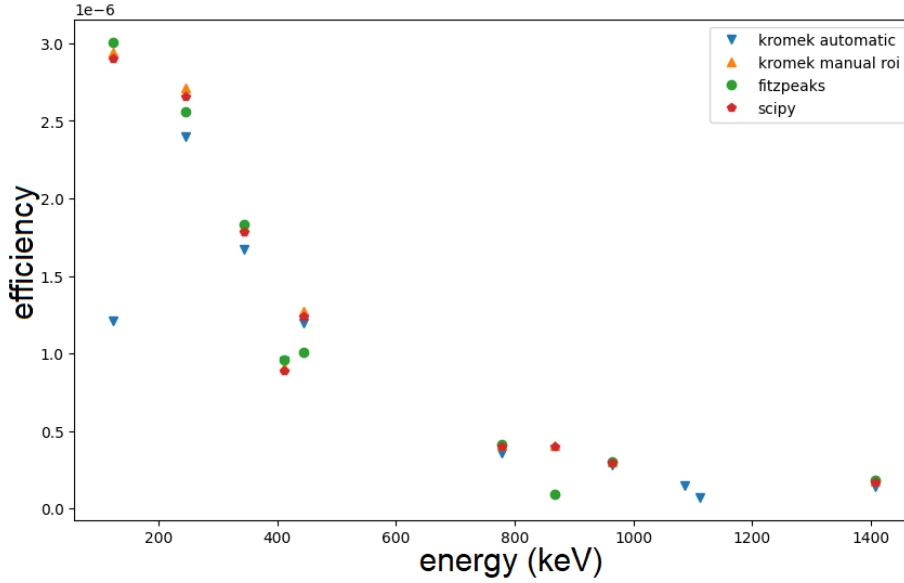


Figure B.7: Comparison between the efficiency values obtained analysing the ^{152}Eu spectrum with different software programs.

Efficiency calibration

The energy spectra of ^{152}Eu , ^{133}Ba and ^{60}Co sources were acquired, to calibrate the chosen detector and to determine its efficiency curve; the steps for these procedures are described in Section B.2. Figure B.7 shows the efficiency values for the gamma-ray lines available of ^{152}Eu as calculated by the four analysis programs under evaluation. The plotted values are reported in Table B.7 of Section B.3.

To continue with the fit of the data points, only the points related to the SciPy program were considered. The efficiency for the detector as a function of energy is represented in Figure B.8. Different radionuclides are plotted with different markers. The data at energy $\gtrsim 600$ keV are better fitted than the data at lower energy. However, the opposite situation is preferable since the radionuclides of medical interest usually emits gamma-rays in the low energy range.

The function in Equation (B.11) is used to fit the data from all three radionuclides at the same time. The optimised parameters are reported in Table B.4 and the correspondent covariance matrix in Table B.5. From the elements of this matrix the uncertainties of the efficiency can be calculated as described in Equations (B.13) and (B.15).

Figure B.9 shows the activity estimation obtained using Equation (B.4). In this estimation the efficiency values are the ones obtained from the curve

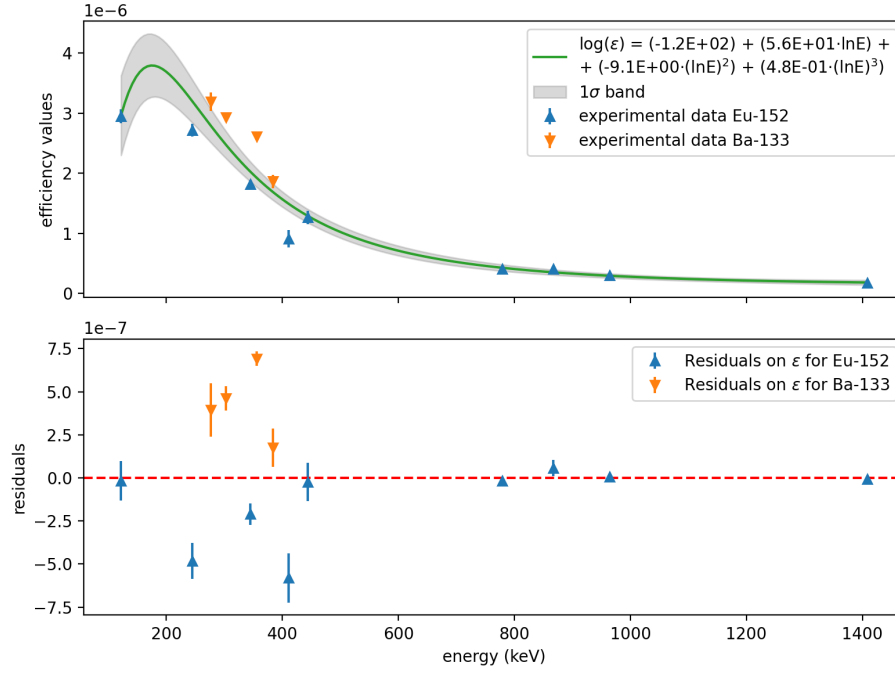


Figure B.8: Plot of the efficiency values (top) obtained with different sealed sources for the GR05 detector. The fitting curve is superimposed to the data and the residuals are shown in the bottom plot.

	value (adim)
a_0	$-193(48)$
a_1	$90(22)$
a_2	$-14.7(35)$
a_3	$0.78(18)$

Table B.4: Optimised parameters for the efficiency fit with the function described in Equation (B.11).

	a_0 (adim)	a_1 (adim)	a_2 (adim)	a_3 (adim)
a_0	2.26e3	-1.06e3	1.66e2	-8.56e0
a_1	-	5.03e2	-7.87e1	4.07e0
a_2	-	-	1.23e1	-6.37e-1
a_3	-	-	-	3.31e-2

Table B.5: Covariance matrix for the efficiency fit with the function described in Equation (B.11).

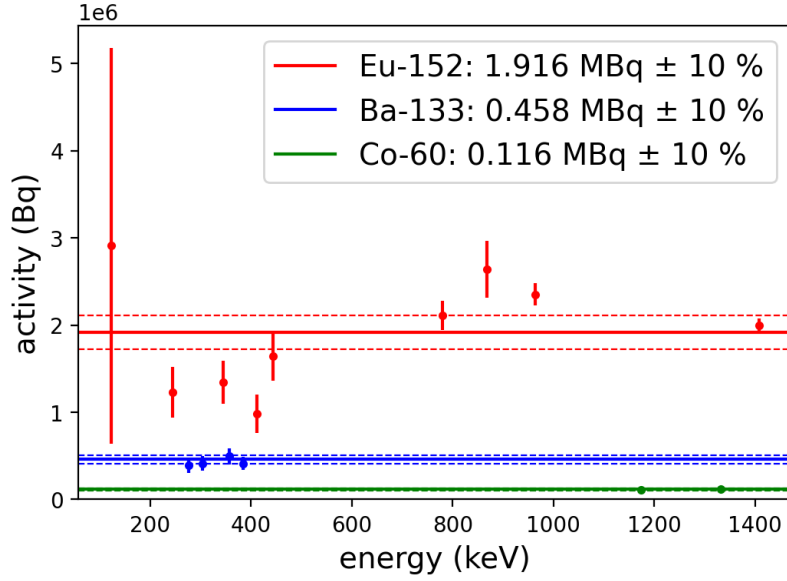
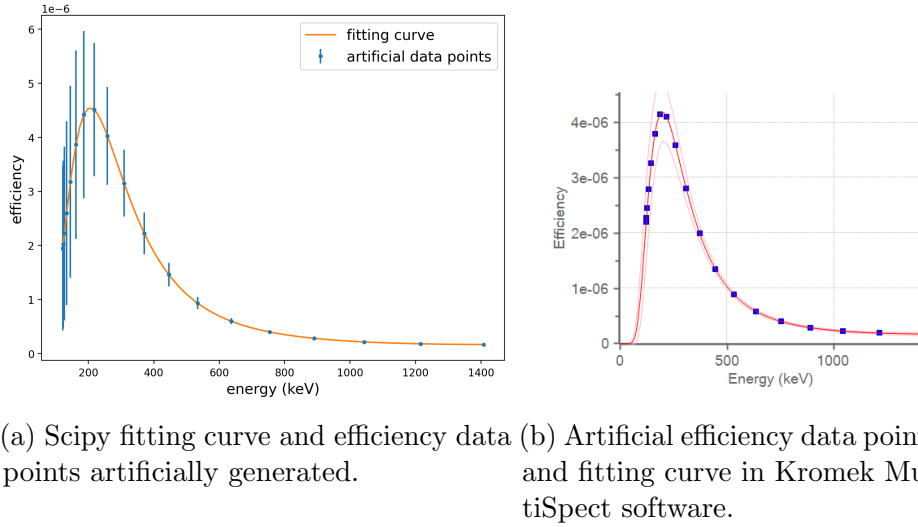


Figure B.9: Estimation of the activity of the calibration sources using the efficiency curve fitting the experimental data.



(a) Scipy fitting curve and efficiency data (b) Artificial efficiency data points and fitting curve in Kromek MultiSpect software.

Figure B.10: Efficiency curve configuration in Kromek MultiSpect.

fitting the efficiency data, thus considering Equation (B.11) and (B.12) with parameters values of Table B.4.

The Kromek software is able to estimate the activity of a radionuclide if an efficiency curve is configured. The curve is configured through a fit performed directly by Kromek program. As described in Section B.2,

Radionuclide	Energy (keV)	Activity (MBq)		
		Scipy	Kromek	Reference
^{152}Eu	121.7817	2.6(22)	1.05(35)	1.916
	244.6974	1.37(38)	1.22(14)	
	344.2785	1.51(25)	1.38(11)	
	411.1165	1.09(22)	1.14(17)	
	443.9606	1.79(26)	1.75(18)	
	778.9045	2.13(26)	1.86(14)	
	867.38	2.63(45)	-	
	964.057	2.32(35)	2.17(17)	
	1408.013	1.98(51)	1.58(28)	
^{133}Ba	276.3989	0.44(10)	0.395(41)	0.45846
	302.8508	0.46(9)	0.428(39)	
	356.0129	0.55(9)	0.467(36)	
	383.8485	0.46(7)	-	
^{60}Co	1173.228	0.11(2)	0.094(14)	0.11646
	1332.492	0.11(3)	0.107(11)	

Table B.6: Comparison between the activity values calculated by Kromek MultiSpect, Scipy and the reference ones.

Figure B.10a shows a set of artificial data points efficiency versus energy that are generated according to the fitting curve for ^{152}Eu , ^{133}Ba and ^{60}Co data sets. A total of 20 of them was generated, with denser sampling in the low energy region (< 300 keV). Supplying more points, the Kromek software is able to obtain the same curve fitted by the external software (such as SciPy). Table B.6 shows the activities calculated starting from each peak of the analysed sources. The activity values obtained from Scipy and Kromek software are compared to the reference values.

The algorithm that estimates on-line the activity of the collected radionuclide is using as detected number of counts \mathcal{N} the value estimated by Kromek MultiSpect in automatic. For this specific application, it could be more appropriated to configure the efficiency curve as the one obtained using MultiSpect automatically calculated net counts instead of SciPy net counts.

Test with ^{43}K

The efficiency calibration curves obtained in the analysis described above were tested with a source of ^{43}K . This radionuclide has a half-life of about 22 h, and it was produced at MEDICIS and measured soon after implantation. The activity measured on 18/07/2024 at 21:34 is 12 MBq [12], this value is assumed as the reference activity \mathcal{A}_{ref} .

In the spectrum some of the ^{43}K lines reported in Table B.2 are overlapping, therefore only the two lines at about 221 keV and 1022 keV can be used. The activity estimated from these two gamma lines are:

energy (keV)	activity (MBq)	compatibility (adim)
220.632	7.6(20)	1.6
1021.698	9.2(17)	2.2

The last column shows the compatibility between the estimations and the reference value of the logbook calculated as

$$\lambda_i = \frac{|\mathcal{A}_i - \mathcal{A}_{\text{ref}}|}{\sigma_i} \quad (\text{B.19})$$

Starting from the full-energy peak at high energy the activity estimation has a good agreement with the reference value. Instead, at low energy the estimated activity is less compatible. This behaviour is expected since the efficiency curve obtained from the calibration has larger uncertainties below 300 keV.

Comparison between different software

In this section the efficiency values for the energy peaks of ^{152}Eu calibration source calculated with different software are compared. The efficiency value of Kromek automatic algorithm at 121 keV is about half of the value calculated by the other three algorithms. This fact suggests that the automatic procedure can underestimate the net counts at low energy, probably due to the influence of the background.

energy (keV)	ϵ (adim)			
	Kromek Auto	Kromek Manual	Fitzpeaks	SciPy
121.78	1.21×10^{-6}	2.94×10^{-6}	3.01×10^{-6}	2.90×10^{-6}
244.6974	2.4×10^{-6}	2.71×10^{-6}	2.56×10^{-6}	2.66×10^{-6}
344.28	1.67×10^{-6}	1.82×10^{-6}	1.83×10^{-6}	1.78×10^{-6}
411.1165	9.5×10^{-7}	9.08×10^{-7}	9.57×10^{-7}	8.89×10^{-7}
443.96	1.2×10^{-6}	1.27×10^{-6}	1.01×10^{-6}	1.24×10^{-6}
778.9	3.58×10^{-7}	4.10×10^{-7}	4.14×10^{-7}	4.02×10^{-7}
867.4	-	4.10×10^{-7}	9.43×10^{-8}	4.01×10^{-7}
964.1	2.81×10^{-7}	3.01×10^{-7}	3.01×10^{-7}	2.94×10^{-7}
1408.013	1.40×10^{-7}	1.74×10^{-7}	1.83×10^{-7}	1.72×10^{-7}

Table B.7: Comparison between efficiency values calculated for ^{152}Eu calibration source using different software.

B.4 Conclusion

Energy and efficiency calibration of detectors are essential for interpreting the acquired data. At the MEDICIS facility, these calibrations are specifically used to estimate the activity of collected radionuclides. The aim of this internship was to obtain a calibration curve for a Kromek GR05 CZT detector, intended for use at the implantation station of the MEDICIS facility.

The curves for both energy and efficiency calibrations were obtained. Applying these curves to the data from which they were derived, the reference activity values (Table B.6) were successfully retrieved. Figure B.9 illustrates the deviation of the estimated values from the reference ones. This difference may result from an imprecise estimation of the counts in the full-energy peak area (see Figure B.4). The figure also shows that the error bars tend to increase at lower energies. This observation suggests that the detectors studied in this internship perform better at energies above 300 keV. Comparing the two detectors, the GR05 exhibits lower efficiency than the GR1, which has a larger crystal, consistent with the expected ratio of their active volumes.

The reliability of the efficiency curve was tested by estimating the activity of a ^{43}K source implanted at MEDICIS during the internship. Considering the uncertainties affecting the measurements, the results are in good agreement with the reference value. Therefore, the detector can be reliably used for activity estimation.

References

- [1] Davide Serafini, Patricija Kalnina, and Charlotte Duchemin. *Kromek CZT detector calibration for activity estimation of medical radionuclides at MEDICIS*. Tech. rep. CERN, 2025. URL: <https://edms.cern.ch/document/3230432/1>.
- [2] Charlotte Duchemin et al. “CERN-MEDICIS: A Review Since Commissioning in 2017”. In: *Frontiers in Medicine* 8 (2021). ISSN: 2296-858X. DOI: 10.3389/fmed.2021.693682. URL: <https://www.frontiersin.org/journals/medicine/articles/10.3389/fmed.2021.693682>.
- [3] *CZT-based high performance gamma-ray spectrometer*. kromek. URL: <https://www.kromek.com/product/gr-family/> (visited on 07/09/2024).

- [4] *Kromek Spectroscopy Software K-Spect*. kromek. URL: <https://www.kromek.com/product/kromek-spectroscopy-software/> (visited on 07/11/2024).
- [5] *NuDat3*. NNDC. URL: <https://www.nndc.bnl.gov/nudat3/> (visited on 07/21/2024).
- [6] Patricija Kalnina. “CERN-MEDICIS isotope mass separation process optimization: the case of Scandium for release study and on-line monitoring of the implanted activity.” Presented 06 Jun 2024. University of Latvia, 2024. URL: <https://cds.cern.ch/record/2899635>.
- [7] Knoll Glenn F. *Radiation Detection and Measurements*. 4th ed. John Wiley & Sons, Inc, 2015. Chap. 4.
- [8] M C Lépy, A Pearce, and O Sima. “Uncertainties in gamma-ray spectrometry”. In: *Metrologia* 52.3 (May 2015), S123–S145. ISSN: 1681-7575. DOI: 10.1088/0026-1394/52/3/s123. URL: <http://dx.doi.org/10.1088/0026-1394/52/3/S123>.
- [9] *FitzPeaks Gamma Analysis and Calibration Software*. JF Computing Services. URL: <https://jim-fitz.co.uk/fitzpeak.htm> (visited on 07/19/2024).
- [10] Pauli Virtanen et al. “SciPy 1.0: Fundamental Algorithms for Scientific Computing in Python”. In: *Nature Methods* 17 (2020), pp. 261–272. DOI: 10.1038/s41592-019-0686-2.
- [11] Michael Heines, Joris De Ridder, and Thomas E. Cocolios. “New best practices for efficiency fitting for accurate gamma-ray spectroscopy with semi-conductor detectors”. In: *Applied Radiation and Isotopes* 225 (2025), p. 112002. ISSN: 0969-8043. DOI: <https://doi.org/10.1016/j.apradiso.2025.112002>. URL: <https://www.sciencedirect.com/science/article/pii/S0969804325003471>.
- [12] *ISO-MEDICIS logbook*. CERN. URL: <https://be-op-logbook.web.cern.ch/elogbook-server/GET/showEventInLogbook/4108693> (visited on 08/12/2024).

List of publications

- [1] Davide Serafini et al. “ ^{111}Ag phantom images with Cerenkov Luminescence Imaging and digital autoradiography within the ISOLPHARM project”. In: *Applied Radiation and Isotopes* 215 (2025), p. 111562. ISSN: 0969-8043. DOI: <https://doi.org/10.1016/j.apradiso.2024.111562>. URL: <https://www.sciencedirect.com/science/article/pii/S0969804324003907>.
- [2] Gaia Pupillo et al. “Cyclotron-based production of innovative medical radionuclides at the INFN-LNL: state of the art and perspective”. In: *The European Physical Journal Plus* 138.12 (Dec. 2023), p. 1095. ISSN: 2190-5444. DOI: 10.1140/epjp/s13360-023-04564-3. URL: <https://doi.org/10.1140/epjp/s13360-023-04564-3>.
- [3] Anna M. Pavone et al. “Biodistribution Assessment of a Novel ^{68}Ga -Labeled Radiopharmaceutical in a Cancer Overexpressing CCK2R Mouse Model: Conventional and Radiomics Methods for Analysis”. In: *Life* 14.3 (2024). ISSN: 2075-1729. DOI: 10.3390/life14030409. URL: <https://www.mdpi.com/2075-1729/14/3/409>.
- [4] Alberto Arzenton et al. “Benchmark of a biophysical model for the radiobiology of RNT with ^{125}I -labelled agents”. In: *The European Physical Journal Special Topics* (July 2025). ISSN: 1951-6401. DOI: 10.1140/epjs/s11734-025-01752-3. URL: <https://doi.org/10.1140/epjs/s11734-025-01752-3>.
- [5] A. Donzella et al. “Monte Carlo dosimetry of silver-111 in simplified cell geometries in the framework of the ISOLPHARM project”. In: *Applied Radiation and Isotopes* 225 (2025), p. 111979. ISSN: 0969-8043. DOI: <https://doi.org/10.1016/j.apradiso.2025.111979>. URL: <https://www.sciencedirect.com/science/article/pii/S0969804325003240>.
- [6] A. Arzenton et al. “The SPES-ISOLPHARM beamline for the production of medical radionuclides at INFN-LNL”. English. In: *Proc. HIAT2025* (Michigan State University, East Lansing, USA). HIAT

16. JACoW Publishing, Geneva, Switzerland, June 2025, pp. 315–318. ISBN: 978-3-95450-260-8. DOI: 10.18429/JACoW-HIAT2025-FRA04. URL: <https://indico.jacow.org/event/82/contributions/8989>.
- [7] Alberto Arzenton et al. “Laser photo-ionization efficiency of ^{111}Ag for medical use in the SPES-ISOLPHARM project”. In: *Applied Radiation and Isotopes* 226 (2025), p. 112143. ISSN: 0969-8043. DOI: <https://doi.org/10.1016/j.apradiso.2025.112143>. URL: <https://www.sciencedirect.com/science/article/pii/S0969804325004889>.

List of Acronyms

ABCD Acquisition and Broadcast of Collected Data

ALPIDE ALice PIxel DEtector

ARG digital AutoRadioGraphy

BBB Blood Brain Barrier

CAPiR Center for Advanced Preclinical *in vivo* Research

CCTV Closed Circuit TeleVisions

CERN Conseil Européen pour la Recherche Nucléaire - European Organization for Nuclear Research

CLI Cerenkov Luminescence Imaging

COG Center Of Gravity

CT Computed Tomography

CZT Cadmium Zinc Telluride

DAQ Data AcQuisition

DICOM Digital Imaging and Communications in Medicine

DUMBO Detector Using MAPS for Beta-rays Observation

FoV Field of View

FPGA Field Programmable Gate Array

FWHM Full Width at Half-Maximum

GAGG Gadolinium Aluminium Gallium Garnet

GUI Graphical User Interface

HCL	Hollow Cathode Lamp
HPMC	HydroxyPropyl MethylCellulose
HV	High Voltage
IOC	Input/Output Controller
ISOL	Isotope Separation On-Line
ISOLDE	Isotope Separator On-Line DEvice
ISOLPHARM	ISOL technique for radioPHARMaceutical
INFN	Italian National Institute for Nuclear Physics
LBC	Lanthanum Bromo Chloride
LENA	Laboratorio Energia Nucleare Applicata
LET	Linear Energy Transfer
LNL	Legnaro National Laboratories
LRMS	Low Resolution Mass Separator
MEDICIS	MEDical Isotopes Collected from ISolde
MAPS	Monolithic Active Pixel Sensors
NAA	Neutron Activation Analysis
NIST	National Institute of Standards and Technology
NP	NanoParticle
ODE	Ordinary Differential Equation
PCB	Printed Circuit Board
PEEK	PolyEther Ether Ketone
PK	PharmacoKinetics
PIS	Plasma Ion Source
PPB	Primary Proton Beam
PSF	Point Spread Function

PSMA Prostate-Specific Membrane Antigen

QC Quality Control

REGe Reverse Electrode coaxial Ge detector

RIB Radioactive Ion Beam

RILIS Resonant Ionisation Laser Ion Source

S100 100 % Sorbitol

SHG Second Harmonic Generation

SiPM Silicon PhotoMultiplier

SIS Surface Ion Source

SPECT Single Photon Emission Computed Tomography

SPES Selection Production of Exotic Species

TIS Target Ion Source

TRT Targeted Radionuclide Therapy

WF Wien Filter